

國立交通大學

電子物理研究所

博士論文

空間控制陣列結構中局域性表面電漿子之
研究



*Studies on Localized Surface Plasmons in Spatially
Controlled Array Structures*

研 究 生：周瑞雯

指 導 教 授：褚德三 博士

共同指導教授：周武清 博士

中 華 民 國 99 年 01 月

空間控制陣列結構中局域性表面電漿子之研究

博士生：周瑞雯

指導教授：褚德三 博士

共同指導教授：周武清 博士

國立交通大學 電子物理研究所

論 文 摘 要

本論文主要在探討具有空間控制的半導體陣列結構上，局域性表面電漿子(localized surface plasmons (LSPs))特性之研究。本論文的第一部份，我們以電子束刻版印刷術(electron beam lithography (EBL))製作出三組不同間距的鍍金矽奈米柱樣品，然後以鎢燈提供的白色光源照射該三組陣列結構，經由反射光譜的觀察，證實該三組陣列結構上的局域性表面電漿子的共振頻率能被調變；鍍金矽奈米柱間距越大則表面電漿子共振頻率越小(紅位移特性)。本論文的第一部份中，我們也探討了以二維有限元素法計算模擬陣列近場範圍內的總能量分佈。近場模擬結果除了顯示局域性表面電漿子的分佈情形和局域性表面電漿子頻率的紅位移特性外，還顯示陣列結構所特有的光柵特性——也就是說，不同間距的結構(相當於光柵)都有對應能在其中形成建設性干涉的特定光波長。在模擬分析中，由高階繞射項在近場範圍(包含角度範圍廣及高階繞射項所能涵蓋的所有角度)內所形成建設性干涉可以被完全預測出來。然而，反射譜無法讓我們觀察到上述的光柵效應，因為反射譜的觀察角度只有在入射角等於反射角的位置上(此角度正好是零階繞射項)。

在建立能提供在空間上排列整齊的局域性表面電漿子頻率的陣列結構之後，我們進行第二部份的研究，將量子點旋轉塗佈在蓋玻片上，再將三個不同間距的鍍金矽奈米柱陣列結構先後分別置於已塗佈完成量子點的蓋玻片上。在三個陣列上，針對相同的

50顆目標量子點觀察其發光強度所受到的影響。我們發現在最密的陣列結構上量子點與金奈米柱可能接觸的面積最大，因而量子點螢光強度減弱的比例最高。而最疏的結構上，其局域性表面電漿子的頻率與量子點螢光頻率最接近，因而其螢光強度增強的比例最高。另外，我們發展出一個新的技巧，使我們在測量量子點螢光強度時也能先後取得陣列結構的光學影像(藉由移除濾鏡，將激發雷射光源聚焦在接近基板位置處，得到基板位置明亮而柱子頂端黑暗的光學影像以定位陣列的位置)、量子點的螢光影像(放回濾鏡，將激發雷射光源聚焦在量子點上)，然後，將兩張影像疊加，進而得以定出量子點與陣列的相對位置。藉由此項技巧，我們歸納出量子點在陣列樣品不同相對位置上發光強度的變化規則。當量子點位在金柱表面所形成的局域性表面電漿區域內或是位在兩金柱中點附近的建設性干涉區，螢光強度皆能增強。在螢光強度能增強的兩個情形中，量子點位在金柱表面所形成的局域性表面電漿區域內，因為量子點螢光能與局域性表面電漿子產生耦合效應，使得量子點螢光具有較短的生命期。而當量子點太靠近金柱(<10 nm)甚至接觸到金柱時，螢光強度減弱機會比較大。最後，再由二維有限元素法，以電磁模型為基礎，在量子點螢光頻率條件下，計算總能量在陣列結構近場空間中分佈的情形。我們得到與實驗一致的結果。

Studies on Localized Surface Plasmons in Spatially Controlled Array Structures

Student: Jui-Wen Chou

Advisor: Prof. Der-San Chuu

Co-Advisor: Prof. Wu-Ching Chou

**Department of Electrophysics, National Chiao Tung University,
Hsin-Chu, Taiwan, Republic of China**

Abstract

This dissertation is devoted to study the localized surface plasmons (LSPs) in spatially controlled array structures. In the first part, three periodic Au coated Si nano rod (SiNR) arrays on Si substrate with different distances between the SiNRs were fabricated by electron beam lithography (EBL). The LSPs is induced when these spatially controlled array structures were irradiated by an un-polarized white light from a tungsten halogen lamp, we found that the trends of reflectance spectra indicate that the LSP frequency can be spatially controlled by manipulating the distances between the SiNRs of the arrays. In addition, the experimental results were compared with 2D numerical simulations based on the finite element method. The simulation result of each array in the near field regions can reveal subtle characteristic of the intensity distributions including the grating effects (the higher order diffractions) and more LSP modes than in the far field reflection observation.

After the investigation of the spatially controlled LSPs, we started the second part of the research, fluorescence signals of quantum dots (QDs) influenced by the three array

structures of the Au coated SiNRs. The QDs were spin-coated on a cover glass. And then, the three array structures were put upside down on the cover glass in sequence. We further developed a new technique which can obtain the optical image of the array structures without losing information of the QD locations at the time of QDs fluorescence measurement. We removed the filter and focused the excitation laser on the substrate to obtain the optical image of the array structures (the substrate is therefore bright, and the top of the SiNR is dark). And then, we put back the filter and focused the excitation laser on the QDs to obtain the fluorescence image of the QDs. After superposing the two images, the relative locations between the QDs and the Au coated SiNRs were defined. The same 50 QDs were successively observed on the three array structures (one by one). On the densest gold coated SiNRs array structure, the highest QDs fluorescence quenching rates are observed. And on the sparsest array structure which provides the LSP frequency closer to the emission band of QDs, the highest QDs fluorescence enhancement rates are observed. The QDs fluorescence enhancement effects are observed on the locations proximity enough (but not touched by the Au) to the Au coated SiNRs, and on the locations near the mid point of two Au coated SiNRs (where the constructive interference is formed). And we found again that when the QDs contact with Au coated SiNRs, instead of enhancement, a non-radiative process may occur, leading to QDs fluorescence quenching. Finally, both in the near field region, 2D numerical simulation results are consistent with the experiment results.

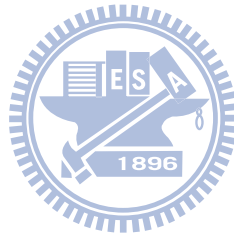
Acknowledgments

感謝我的指導教授褚德三老師，一路上指引我研究的方向、給我很多鼓勵和支持、給我最好的環境學習如何做研究。在這個過程中，很多時候，我忙了老半天完成不堪一擊的東西，硬著頭皮想要趕著交差了事。老師總是嚴格看待，要我好好正視缺點，想辦法改進。我很感謝老師的耐心指教，給我機會修正，否則我這個不算嚴以律己的人，鐵定不可能進步太多。我還要感謝共同指導教授周武清老師，總是給我很多的指導、建議和幫助。無論是與實驗相關的研究之道或是待人處世的道理，老師給的都是最重要的提示。當然，我也要感謝實驗室的夥伴們，和我一起成長，有過許多失敗，也完成一些不可能的任務。當然這些任務是因為有大家再三幫忙、一直互相加油打氣，不然不可能的任務就真的還是不可能了！

特別感謝麥克博士、克莉斯汀教授和古舍立教授在實驗上和論文寫作上給我很多的指點和幫忙。感謝我的好朋友們陪我度過抱怨很多或是坐立難安不然就是超級開心的時刻。最後，我要感謝親愛的爸爸、媽咪、三姑、二姑、姊姊、妹妹，沒有你們的愛心加持，我可能沒有勇氣開始這趟旅程也很有可能會半途而廢。

Contents

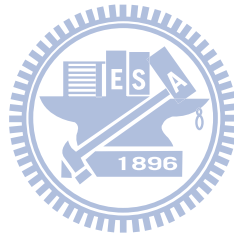
Abstract in Chinese	I
Abstract in English	III
Acknowledgments	V
Contents	VI
List of Tables	IX
List of Figures	IX
Chapter 1 Introduction	1
1-1 Motivation	1
1-2 Surface Plasmons	2
Chapter 2 Experiments and Techniques	22
2-1 Micro Raman Spectrometer	22
2-2 Fluorescence Lifetime Imaging Microscopy	24
2-3 Scanning Near-Field Optical Microscope	27
2-4 Reflectance Spectrometer	29
Chapter 3 The Finite Element Method	31
Chapter 4 Fluorescence Signals of Core-shell Quantum Dots Enhanced by Single Crystalline Gold Caps on Silicon Nanowires	38
4-1 Introduction	38
4-2 Experiment	40
4-3 Results	43



4-4 Discussion	50
4-5 Conclusion	57

Chapter 5 Observation of the Localized Surface Plasmons in Spatially Controlled

Array Structures	62
5-1 Observed by Scanning Near-Field Optical Microscope	62
5-1-1 Introduction	63
5-1-2 Results	63
5-1-3 Conclusion	64
5-2 Observed by Reflectance Spectrometer	65
5-2-1 Introduction	65
5-2-2 Experiment	66
5-2-3 Results	68
5-2-4 Discussion	72
5-2-5 Conclusion	77



Chapter 6 Fluorescence Signals of Quantum Dots Influenced by Spatially Controlled

Array Structures	80
6-1 Introduction	80
6-2 Experiment results and discussion	81
6-3 Conclusion	88

Chapter 7 Surface Enhanced Raman Scattering Observed on Spatially Controlled

Array Structures	91
7-1 Introduction	93
7-2 Experiment results	94
7-3 Discussion	97
7-4 Conclusion	102

Chapter 8 Conclusion	106
Chapter 9 Future Works	109
Publication Lists	115



List of Tables

Tab. 5.1: The peripheral distances and the diagonal distances, the incident wavelengths of the localized surface plasmons modes of array (a-c) observed in the reflectance spectra, 2D finite element method simulations results.....71

List of Figures

Fig. 1.1: The characteristics of surface plasmons wave propagating at the interface of the metal-dielectric material.....4

Fig. 1.2: Surface plasmon polaritons excitation configurations.....6

Fig. 1.3: Three-channel microscope set-up reported by Lukin's group.....9

Fig. 1.4: Optical Surface plasmons coupled to quantum dots with simulation results reported by Lukin's group.....10

Fig. 1.5: Normalized energy flux for an emitter at different position.....11

Fig. 1.6: Nanoengineered fluorescent response of quantum dots.....12

Fig. 1.7: Reflectance spectra of quantum dot-doped samples for four different silver disk.....12

Fig. 2.1: Optical path simple description of the Micro-Raman spectrometer.....23

Fig. 2.2: Jobin Yvon LabRam HR800, side view I.....23

Fig. 2.3: Jobin Yvon LabRam HR800, side view II.....24

Fig. 2.4: The schematic diagram of fluorescence images and the lifetime measurement system.....26

Fig. 2.5: The fluorescence images and the lifetime measurement system.....	26
Fig. 2.6: The scan near field optical microscope (SNOM).....	28
Fig. 2.7: The schematic of optical system of the reflectance spectrometer.....	29
Fig. 3.1: Illustration of the eth segment and the linear shape functions.....	34
Fig. 3.2: The computation domain and node coordinates for the eth triangle.....	36
Fig. 4.1: SEM images of silicon nanowires grown by electron beam evaporation.....	44
Fig. 4.2: TEM and SEM cross sectional micrograph of a silicon nanowire, and oblique SEM micrograph of silicon nanowires after chemical gold-cap removal.....	45
Fig. 4.3: Fluorescence PL study of quantum dots on different substrates.....	46
Fig. 4.4: Fluorescence PL measurements quantum dots on different locations on silicon nanowires with nanoscale gold-caps on silicon (111) substrates.....	47
Fig. 4.5: High resolution SEM micrographs that show the quantum dots on silicon nanowires with nanoscale gold-caps on silicon (111) substrates.....	49
Fig. 4.6: Electron backscatter diffraction pattern of a gold-cap on a silicon nanowires	50
Fig. 4.7: Finite element modeling of the electromagnetic field enhancement at a silicon nanowire with gold-cap atop.....	52
Fig. 4.8: Maximum enhancement factor deduced from 2D finite element method calculations.....	53
Fig. 4.9: Fluorescence signals Time-Related Single Photon Counting analysis of single quantum dots on silicon nanowires with and without gold-cap.....	55
Fig. 5.1: SEM images of the array structure and the NSOM images of different incident wavelengths.....	64
Fig. 5.2: Localized Surface Plasmons in Spatially Controlled Array Structures: SEM images, reflectance spectra and 2D finite element method simulation results...	65

Fig. 5.3: SEM images of gold-coated silicon nanorods arrays, a unit cell of array, the mesh diagram, the integration areas, the enhancement factors calculated in the integration areas of array (c).....	67
Fig. 5.4: Reflectance spectra of array (a-c).....	70
Fig. 5.5: 2D finite element method calculations of the normalized time average total energy densities of array (a-c).....	73
Fig. 5.6: Reflectance spectra and 2D finite element method simulations results of array (a-c).....	74
Fig. 6.1: SEM images of gold-coated silicon nanorods arrays, schematic view of the sample structure, and the reflectance spectra of arrays (a-c).....	82
Fig. 6.2: Fluorescence images of 50 different quantum dots on arrays, statistic event numbers of the enhancement factors, the multi channel scalar and the Time-Correlated Single Photon Counting of one of the single quantum dots picked up from the 50 quantum dots on arrays and on the glass.....	84
Fig. 6.3: The quantum dots fluorescence images, the reflectance image combined with schematic square unit cell, Time-Correlated Single Photon Counting and multi channel scalar trace and simulation results.....	87
Fig. 7.1: SEM image of one of the gold nanoparticle array structures and the surface enhancement Raman scattering results reported by N. Félidj et al.....	92
Fig. 7.2: SEM images, optical images, and the Raman mapping of gold-coated silicon nanorods arrays.....	94
Fig. 7.3: Surface enhanced Raman scattering and average surface enhanced Raman scattering of the molecule crystal violet aqueous on arrays.....	96
Fig. 7.4: Reflectance spectra of arrays.....	98
Fig. 7.5: Finite element method analysis of arrays.....	100

Fig. 9.1: SEM images of AFM tip and the nanowire tip.....109

Fig. 9.2: Setup of the Tip Enhancement Raman Spectroscopy with Si nanowire tip
measurement.....110

Fig. 9.3: Enhanced Raman spectra of malachite green.....111

Fig. 9.4: Electron micrograph of various metal structures.....112

Fig. 9.5: Light excites a surface plasmon resonance on a metal nanoparticle and is coupled
into silicon, simulation of increased light intensity beneath a metal nanoparticle
on a silicon cell, and SEM image of silver nanoparticles on a solar cell.....113



Chapter 1 Introduction

§ 1-1 Motivation

Lukin's group [1], has demonstrated a cavity-free, broadband approach for engineering photon-emitter (the CdSe quantum dots (QDs) [2]) interactions [3, 4] via sub-wavelength confinement of optical fields near metallic nano-structures (the silver nanowires) [5-8]. It should be interesting to investigate which geometric size and shape of metallic structures can be coupled to QDs and generate surface plasmons (SPs) [9-10] with frequencies we hope. Our research topics about the colloidal QDs fluorescence influenced by the localized surface plasmons (LSPs) [10-25] were investigated by two series of candidates, *i.e.* the substrate of gold-caps on top of Si nanowires (SiNWs) [26-27] (inhomogeneous in size and shape) and the substrate of gold-coated Si nanorod (SiNR) array structures [28-29] (homogeneous in size and shape). Gold was chosen for it is a good metal [30-31] for forming surface plasmon polaritons (SPPs) [32-48] on its surface. For the first series of substrate, by the gold-catalyzed vapour-liquid-solid (VLS) growth mechanism fabricated gold-caps on top of SiNWs [26-27, 49-51] which provided proper surface conditions for forming the LSPs resonance, we observed the fluorescence signal enhancement of the QDs [27] (illustrated in chapter 4). However, the gold-caps on top of SiNWs fabricated by the VLS growth mechanism (based on the addition of certain metal impurities and small globules of the impurity (not with regular sizes and shapes) are located at the tip of the wire during growth [52-53]) are not with regular sizes and shapes. Since the LSPs resonance frequencies are strongly dependent on the geometric sizes and shapes of the metallic particles, there are difficulties in analyzing how the fluorescence is influenced.

Hence, the second series of substrates were fabricated, by electron beam lithography (EBL) properly arranging the geometric configurations of gold-coated SiNR array structures, we are able to manipulate the LSPs resonance frequencies [28-29]. The geometries of the array structures were designed based on the finite element method (FEM) [54-55] (will be illustrated in chapter 3) which can obtain the near-field distribution of the array structures for estimating the target LSPs resonance frequencies. By the proper design of the distances between the SiNRs of array structures, we can spatially control the LSPs resonance frequencies. The relative LSPs topics investigated by the second series of substrate “gold-coated SiNR array structures” (which is corresponding to the title of the dissertation) will be illustrated in chapter 5, 6 and 7 [28-29].

§ 1-2 Surface plasmon



After a brief illustration of the motivation and the arrangement in the dissertation, we would like to give an introduction to the SPs [9-10] in the following. SPs were first brought up by Ritchie in the 1950s [10], and were extensively studied in the following two decades. The relative applications are getting hotter in the modern age due to the progress of the nanometer-sized structure manufacture technology. Many possible applications such as the surface enhanced Raman scattering (SERS) [56-64], solar cells [65], plasmon waveguides [66], filters and microscopy [67-68], etc. have been developed and improved till now.

SPs [9-10] are coherent electron oscillations at the interface between any two materials with opposite sign of the dielectric function (in the real part) across the interface (for example: the metal-dielectric interface, the metal-air interface). When SPs [9-10] couple with a photon, the resulting hybridised excitation is called a surface plasmon polariton

(SPP) [32-48]. In other words, a combined excitation consisting of a surface plasmon and a photon is called a SPP [68-71]. The light waves are trapped on the metal surface due to their interaction with the free electrons (provided by the metal). And the free electrons which are in resonance with the light wave oscillate collectively. At the moment, the SPPs [68-71] are formed. In addition to SPs [9-10] on a plane surface, excitations of electron plasmons bounded in geometries such as bumps or voids are called LSPs [10-25, 68, 72]. It is worthwhile to mention that the SPP mode can be excited only if both the frequency and wave vector of the excitation light match the SPP frequency and the SPP wave vector; whereas the LSP mode can be resonantly excited with light of appropriate frequency with arbitrary excitation light wave vector [68]. LSP resonances play an important role when the SPPs propagate on rough surfaces. Significant enhancement due to the SPP scattering can be found on surface defects when the frequency of SPP and resonant frequency of LSP are close to each other [66, 73-75].

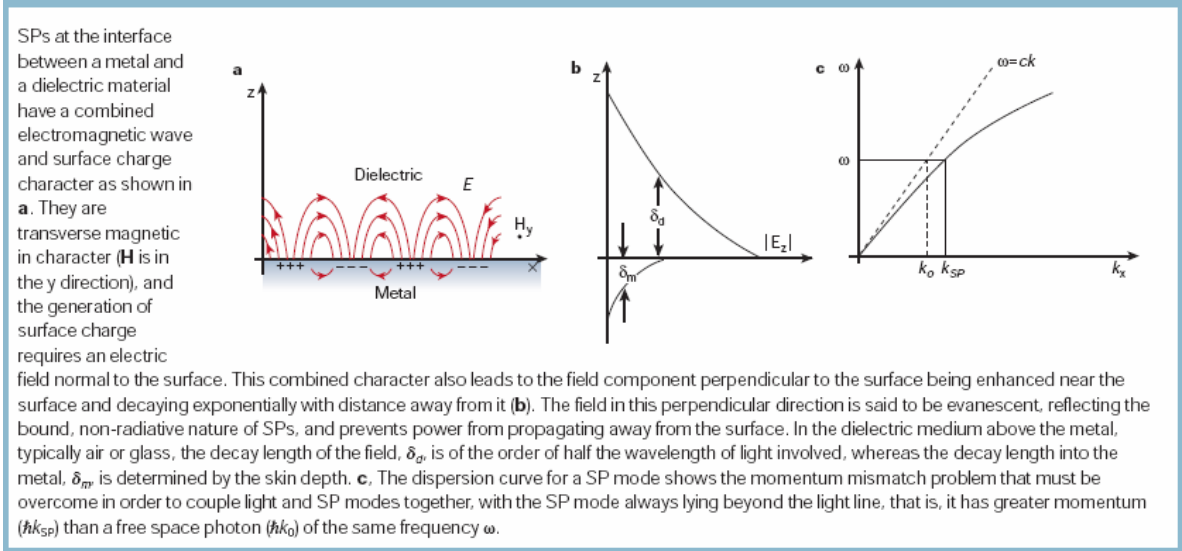
For the interface of the metal and the dielectric infinite plane, Eq. (1.1) describes the relation between the frequency-dependent SP wave vector k_{sp} and the frequency-dependent electromagnetic wave vector k_0 in the free space.

$$k_{sp} = k_0 \sqrt{\frac{\epsilon_d \epsilon_m}{\epsilon_d + \epsilon_m}} \quad (1.1)$$

Where ϵ_m and ϵ_d is the frequency-dependent permittivity of the metal and the dielectric material respectively. For the interface of the metal-dielectric, $\sqrt{\frac{\epsilon_d \epsilon_m}{\epsilon_d + \epsilon_m}} > 1$, the momentum of the SP mode $\hbar k_{sp}$ is greater than that ($\hbar k_0$) of a free-space photon [68].

When the SPs wave propagating at the interface of the metal-dielectric material, the transverse magnetic (parallel to the interface) and the electric field (normal to the interface) are formed as shown in Fig. 1.1(a). This character based on the electromagnetic theory leads to the field enhancement near the surface and decaying exponentially with distance

away from the metal surface as shown in Fig. 1.1(b). The field decaying away from the surface is corresponding to the field bounded near the surface which leads to the non-radiative feature of SPs (preventing power from propagating away from the surface) [12].



Figs. 1.1(a)(b)(c) The characteristics of SPs wave propagating at the interface of the metal-dielectric material [12]

Eq. (1.1) can be obtained by solving the Maxwell's equations [55] with continuous boundary conditions on the interface. The full set of Maxwell's equations in the absence of external sources can be expressed as follows:

$$\nabla \times \mathbf{H}_i = \varepsilon_i \frac{1}{c} \frac{\partial}{\partial t} \mathbf{E}_i, \quad (1.2)$$

$$\nabla \times \mathbf{E}_i = -\frac{1}{c} \frac{\partial}{\partial t} \mathbf{H}_i, \quad (1.3)$$

$$\nabla \cdot (\varepsilon_i \mathbf{E}_i) = 0, \quad (1.4)$$

$$\nabla \cdot \mathbf{H}_i = 0, \quad (1.5)$$

For the interface shown in Fig. 1.1(a), the index i can be applied for the dielectric or for the metal, i.e. $i=d$ or $i=m$. Solutions of equations (1.2)-(1.5) can be expressed as:

$$\mathbf{E}_i = (E_{ix}, 0, E_{iz}) e^{-\kappa_i |z|} e^{i(k_i x - \omega t)}, \quad (1.6)$$

$$H_i = (0, H_{iy}, 0)e^{-\kappa_i|z|}e^{i(k_i x - \omega t)}, \quad (1.7)$$

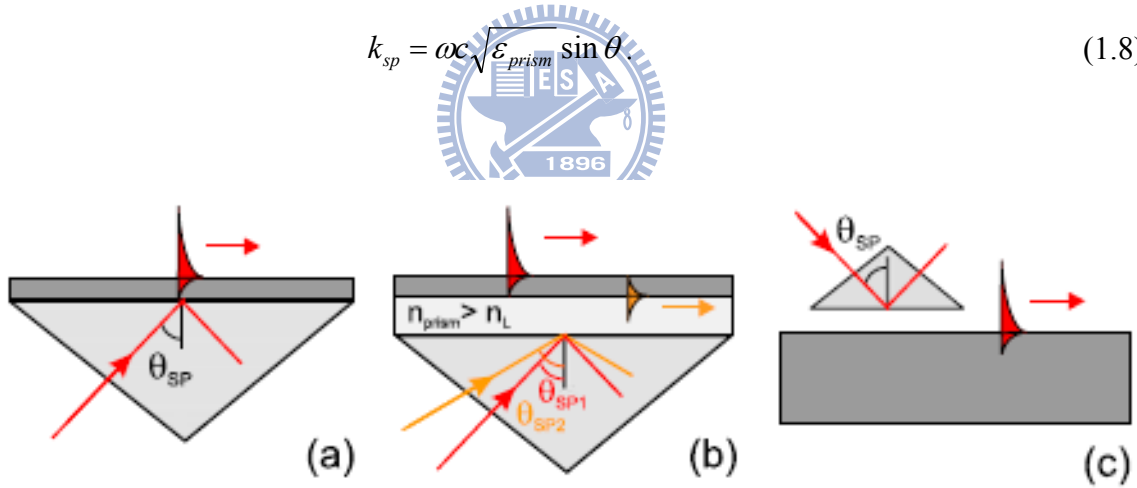
Where E_{ix} and E_{iz} are for the x and z component electric fields respectively, and H_{iy} is for the y component magnetic field. k_i is the frequency-dependent electromagnetic wave vector, and ω is the angular frequency. $\kappa_i = \sqrt{k_i^2 - \varepsilon_i \frac{\omega^2}{c^2}}$, the exponential term with negative real argument $e^{-\kappa_i|z|}$ is corresponding to the feature of z component field bounded near the surface of the metal, as shown in Fig. 1.2(b). Above the metal surface, the decay length of the field [12] is defined as $\delta_d = \frac{1}{\kappa_d}$, i.e. when the field falls to 1/e, and is in the order of half wavelength of involved light whereas inside the metal, the decay length is determined by the skin depth [12] $\delta_m = \frac{1}{\kappa_m}$.

Substitute Eq. (1.6) and Eq. (1.7) into Eqs. (1.2)-(1.5) with the boundary condition that the electric and magnetic fields parallel to the interface of the dielectric material and the metal must be continuous, one obtains Eq. (1.1) to describe the relation between the SP wave vector k_{sp} and the wave vector k_0 in the free space. The dispersion relation is shown in Fig. 1.1(c). For the same angular frequencies, the SP modes have higher momentum than the light in the free space [12].

Although the SPPs in the infinite plane interface between the dielectric and the metal can be solved analytically, however, for the other complicated cases such as our gold-caps on SiNWs substrates and gold-coated SiNR array structures, the analytic solutions are not available. When the geometry of the interface is complicated, and the problem cannot be solved analytically, the FEM [54-55] provides reliable numerical solutions and is usually applicable. Therefore, we use the FEM to design our array structures and analyze the LSP problems for our array structures.

By the way, from the SPP dispersion relations (Eq. 1.1), we found that the SPP wave vector (k_{sp}) is larger than the photon wave vector (k_0) which means that the light illuminating a plane surface cannot be directly coupled to surface polaritons [20, 68]. Special experimental arrangements by Kretschmann [76] and Otto [77] as shown in Figs. 1.2(a-c) have been designed to provide the condition for matching the wave vector of the photon and the SPP. In the Kretschmann's setup [68, 76] (Fig. 1.2(a)), light incidents to the metal film through the dielectric prism at an angle of incidence greater than the angle of total internal reflection [76]. At a certain angle of incidence θ where the in-plane component of the photon wave vector in the prism coincides with the SPP wave vector on an air-metal surface, resonant light tunneling through the metal film occurs and light is coupled to the surface polaritons [68]:

$$k_{sp} = \omega c \sqrt{\epsilon_{prism}} \sin \theta \quad (1.8)$$



Figs. 1.2 SPP excitation configurations: (a) Kretschmann geometry, (b) two-layer Kretschmann geometry, (c) Otto geometry. [68]

Under these resonant conditions, because light is coupled to SPPs with high efficiency, a sharp minimum reflectivity is observed from the prism interface [68]. When increase the thickness of the metal film, the efficiency of the SPP excitation decreases (because the tunneling distance is increased). SPP on an interface between the prism and metal cannot be excited anymore when the wave vector of SPP at the interface is greater than the photon

wave vector in the prism (at all possible incident angles). An additional dielectric layer (with a refractive index smaller than the refractive index of the prism) should be deposited between the prism and the metal film (Fig.1.2 (b)). In such a setup, the photon tunneling through this additional dielectric layer can provide resonant excitation of SPP on the inner interface.

For thick metal films (or surfaces of bulk metal), SPP can be excited in the Otto's setup [68, 77] (as shown in Fig. 1.2(c)). In the setup, similar to Kretschmann's setup (Fig. 1.2(b)), the additional dielectric layer is the air. The prism where total internal reflection occurs is placed close to the metal surface, so that photon tunneling occurs through the air gap between the prism and the surface [68, 77]. And of course, the resonant conditions can also be derived from (Eq. (1.8)).

In the Following, we give an illustration of the colloidal QDs which contain wide applications and play an important role in our research. A quantum dot (QD) is a semiconductor whose excitons are confined in three dimensions [78-80]. The chemical colloidal synthesis is one of several different methods (such as lithographic techniques, epitaxial techniques by chemical methods, ion implantation) to fabricate QDs. Many different chemical compositions of colloidal QDs can be possibly synthesized, for examples, cadmium selenide (CdSe), cadmium selenide tellurium (CdSeTe), cadmium sulfide (CdS), indium arsenide (InAs), and indium phosphide (InP), etc. The diameters of the colloidal QDs are ~ 2 to 10 nm which possibly contain 100~ 100000 atoms [81].

Colloidal QDs are synthesized based on a three-component reaction medium, i.e. precursors, organic surfactants, and solvents. By heating the reaction medium to a sufficiently high temperature, the precursors can be chemically transformed into monomers. When the monomers reach a high enough supersaturating level, the nanocrystal growth starts with a nucleation process. The temperature and the monomer concentration are two critical factors in determining optical conditions of the colloidal QDs [81]. For excellent

condition controlling, the QDs fluorescence photo luminescence signals exhibit narrow and symmetric emission peaks (FWHM typically in the few 10 nm range) [80-84].

Two important optical features of the QDs are the tuneable fluorescence frequencies and the quantized energy spectra with quantized density of states near the band gap edges. Due to quantum confinement which causes the band gap energy varying with the particle size [78-81, 85-91], by tuning the chemical composition and the particle size of QD, fluorescence emission wavelength of the QD varied in a wide range, from 400 to 2000 nm. The band gap energy which determines the fluorescence energy of the QD is inversely proportional to the square of the size of the QD [81]. The larger the QD size, the lower frequency of its fluorescence spectrum.

Till now, comprehensive QD applications in optoelectronics devices such as solar cells [92], light-emitting diode (LEDs) [93], and diode lasers [94], biological and medical studies (investigated QDs as agents for medical imaging [95]), and quantum computation [95-96] have been carried out. In modern biological analysis, QDs are superior to traditional organic dyes on brightness (due to 20 times higher quantum yield) and stability (due to less photobleaching) [81, 84, 97-106]. The QDs applications are widely developed in the study of intracellular process at the single molecule level, high-resolution cellular imaging long-term in vivo observation of cell trafficking, tumour targeting, and diagnostics [107-109] etc.

QDs can be synthesized with larger (and thicker) shells and formed core/shell structures. In this study (will be illustrated in chapter 4 and 6) we choose the commercial core/shell CdSeTe/ZnS [2] colloidal QDs in a highly dilute aqueous solution, the wavelength of the fluorescence center is at 705 nm.

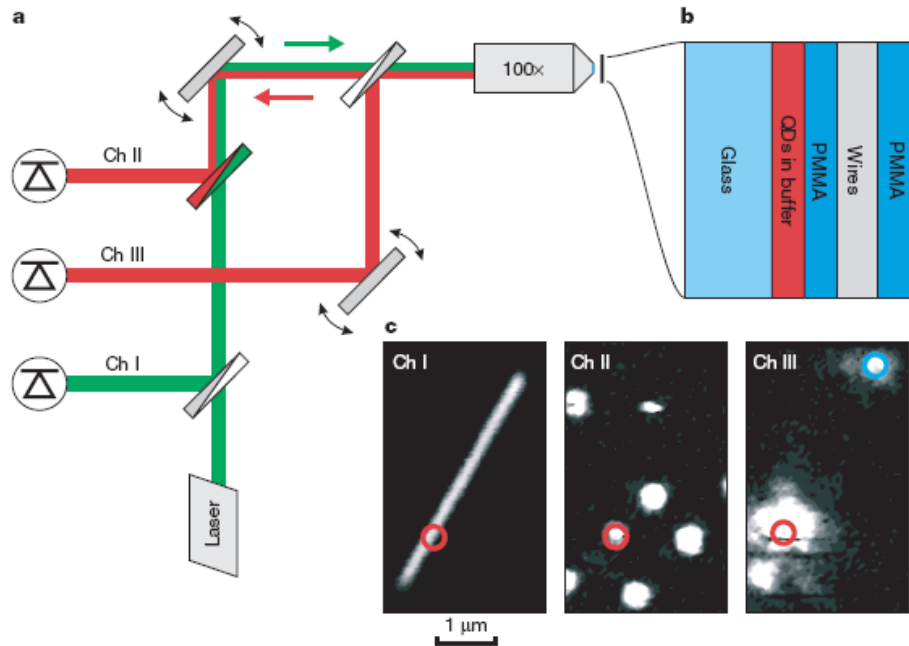


Fig. 1.3 Experimental set-up **a**, Three-channel confocal microscope with 532 laser excitation source. **b**, Layout of sample containing QDs and Ag NWs. The samples were created by spinning QDs onto a glass substrate, covering them with $\sim 30\text{nm}$ layer of poly (methylmethacrylate), and then depositing dry wires on top. Finally, the sample was overcoated with a thick layer of PMMA. **c**, Left, channel I: Ag NW image. Middle, channel II: image of QDs. The red circle denotes the position of the coupled QD, and the same point is also denoted in the leftmost image. Right, channel III: the excitation laser was focused on the QD (red circle). The largest bright spot corresponds to the QD fluorescence, while two smaller spots correspond to SPs scattered from the Ag NW ends. The blue circle indicates the farthest end of the NW, used for photon cross-correlation measurements. [1]

After reviewing the previous experimental arrangements of SPs and the illustration of colloidal QDs [2], now let us review two previous relative papers in the following. In the year of 2007, M. D. Lukin et al. reported that the observation of single optical plasmon in silver nanowires (Ag NWs) coupled to the CdSe single quantum dot (SQD) as shown in Fig. 1.3c by the three-channel set-up (the excitation source: 532 nm wavelength laser, power $< 4\mu\text{W}$) as shown in Figs. 1.3a-b, When a SQD is excited in close to an Ag NW, fluorescence occurs from the SQD coupled to SPs in the Ag NW. At the moment, not only the SQD fluorescence (more than 2.5-fold enhancement) is emitted but also two end sides of the wire are lightened up (due to couple to SPs) as shown in Fig. 1.3c.CHIII.

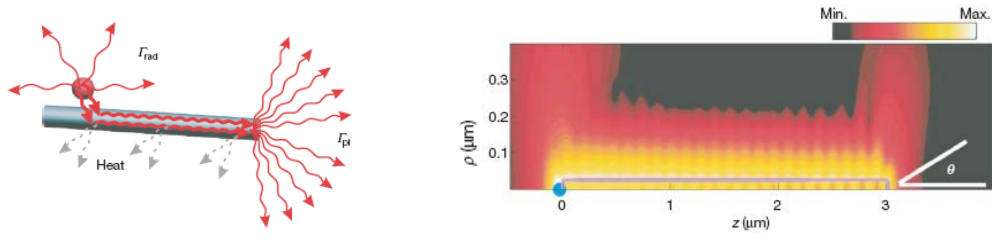
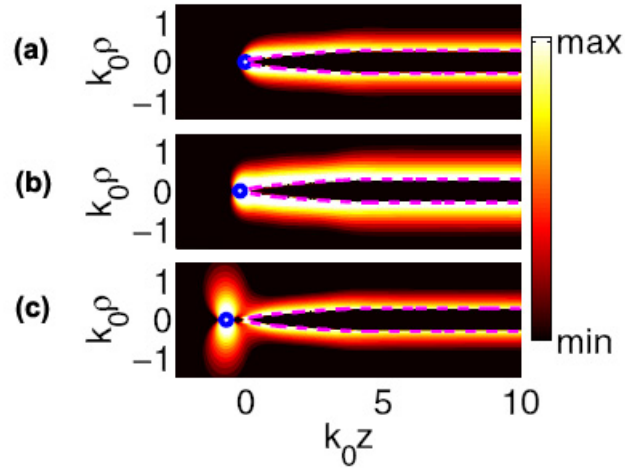


Fig. 1.4 Radiative coupling of QDs to conducting nanowires (NWs). In the left side, a coupled QD can either spontaneously emit into free space or into the guided SPs of the NW with respective rates $\Gamma_{rad}, \Gamma_{pl}$. In the right side, simulations of the electric field amplitude (arbitrary units) emitted by a dipole (blue filled circle) positioned 25 nm from one end of a conducting NW (whose surface is outlined) 3 μm in length and 50 nm in diameter. The vertical scale (ρ) is enlarged compared to the horizontal (z) to clearly show the near field of the SP energy is clearly scattered into the far-field, while the remaining is either lost to dissipation or to back-reflection. θ is the emission angle. [1]

Similar to the optical modes of a conventional dielectric fiber, a broad continuum of SP modes can be confined on a cylindrical metallic wire and guided along the wire axis [7-8] as shown in Fig. 1.4 (the left side). The field confinement with reduced velocity of SPs which occurs when the QD fluorescence coupled into the guided SP modes [4] is much like a lens with extraordinarily high numerical aperture. For an optimally placed emitter, the spontaneous emission rate Γ_{pl} into SPs is larger than the radiative (Γ_{rad}) rate and non-radiative rate (Γ_{nrd}), which results in highly efficient coupling to SPs and enhancement of the total decay rate (Γ_{total}) compared to that of an uncoupled emitter (Γ_0). This enhancement can be characterized by a Purcell factor, $P = \Gamma_{total} / \Gamma_0$ [1, 4]. A simulation of the SPs in this case is shown in Fig. 1.4 (the right side). A QD is placed 25 nm away from one of the Ag NW's end (marked with the blue circle). The SPs decay from the edge of Ag NW. The fluorescence from the QD emits into free space, and the SP scattering appears at the other end of the Ag NW.

Normalized energy flux of the typical position for an emitter is demonstrated by the FEM simulation (combined with coupled-mode theory) as shown in Figs. 1.5(a-c) [110]. In Fig. 1.5(a), the emitter is at the distance $k_0d = 0.002$ (very close to the nanotip): the emitter decays primarily nonradiatively. In Fig. 1.5(b), the emitter is at the distance $k_0d = 0.2$: efficient excitation of guided plasmons. And in Fig. 1.5(c), the emitter is at the distance $k_0d = 0.7$: associated with radiative decay.



Figs. 1.5 Normalized energy flux for an emitter (denoted by the blue circle) positioned at the distance **(a)** $k_0d = 0.002$, **(b)** $k_0d = 0.2$ and **(c)** $k_0d = 0.7$ from the nanotip. The surface of the nanotip is indicated by the dotted lines. [110]

Another paper closely related to our work was reported by Arto V. Nurmikko et al. In 2005, [70], this article reported that the fluorescent from QDs in proximity to the SPP field of periodic Ag nanoparticle arrays can be enhanced. Tuning the SPP resonances to the QD exciton emission band results in an enhancement of up to ~ 50 - fold in the overall fluorescence efficiency as shown in Fig. 1.6. Propagating modes of SP resonances can be tuned by varying the diameters and the lattice constants of the Ag nanoparticle arrays. As shown in Fig. 1.7, the valley in the reflectance spectra which corresponding to the LSP can

be tuned by different diameters and lattice constants of the Ag nanoparticle arrays. The larger the diameter (and the lattice constant), the lower the LSP frequency.

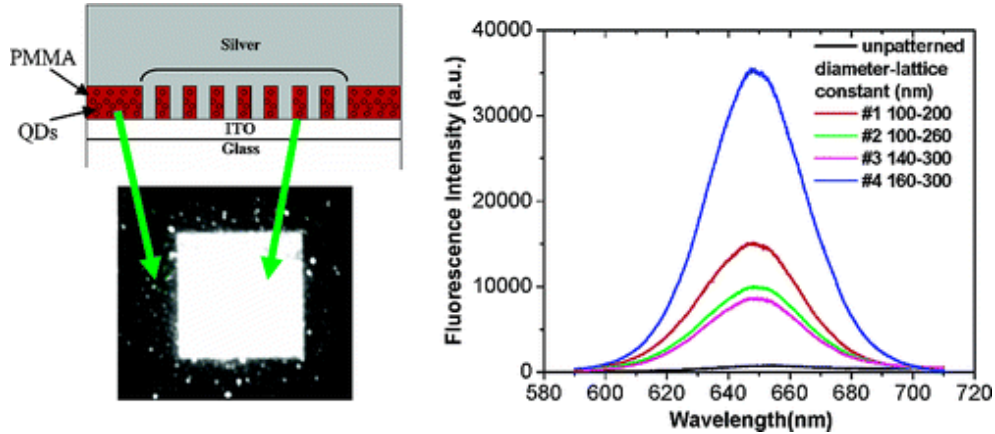


Fig.1.6 Nanoengineered fluorescent response is reported from semiconductor core–shell (CdSe/ZnS) QDs in proximity to the SPP field of periodic Ag nanoparticle arrays (as shown in the left upper side). Propagating modes of SP resonances have a direct impact on the fluorescence enhancement (as shown in the left lower side and the PL in the right side) [70].

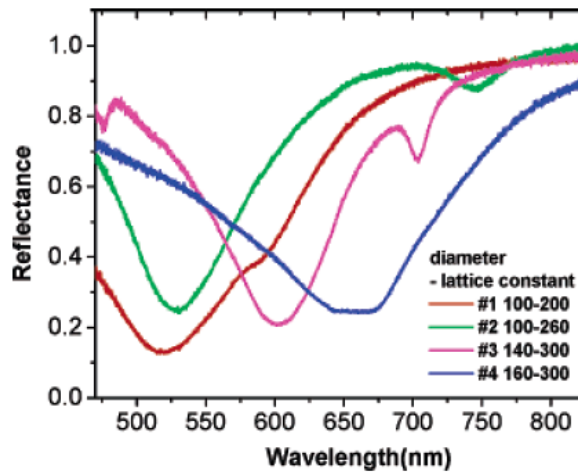


Fig. 1.7 Normal incident reflectance spectra of QD-doped samples for four different Ag disk diameters and lattice constants labeled from #1 through #4. Respective diameter and lattice constants are as follows: #1, 100 and 200 nm; #2, 100 and 260 nm; #3, 140 and 300 nm; #4, 160 and 300 nm [70].

Comparing with our results, by two series of substrates “Au caps on top of SiNWs” (will be illustrated in chapter 4) and “Au coated SiNR array structures” (will be illustrated in

chapter 5 and 6), we investigated the LSP and how the QDs fluorescence can be influenced. On both series of substrates, we observed QDs fluorescence enhancement on hot spots (the hot spots are specific regions (near the metal surface) where the high electromagnetic fields (caused by LSP coupling) are formed) [27-29]. However, the first series of substrate “Au caps on SiNWs” is inhomogeneous in size and shape and the number of the hot spots is rare (not so efficient for enhancement), we started to design the second series of substrate “Au coated SiNR array structures” [28-29] based on 2D FEM [54-55]. We found that by tuning the distance between the SiNRs of the array structures, we can spatially control the LSP resonance modes [28]. And since arrays of the hot spots were formed by this way, much more efficient enhancement can be reached [29] (chapter 5 and 7). By developing a new technique which obtains the optical image of the array structures without losing information of the QD locations, we are able to further investigate how the QDs fluorescence influenced by spatially controlled array structures [29]. We found QDs fluorescence on the array structures can be enhanced or quenched (depend on the relative positions between the QDs and the Au coated SiNRs) [29, 101], and 2D FEM [54-55] simulation results are helpful for analyzing the experiment results [27-29].

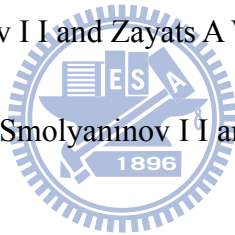
Reference:

- [1] Akimov A. V., Mukherjee A., Yu C. L., Chang D. E., Zibrov A. S., Hemmer P. R., Park H. & Lukin M. D. *Nature* **450**, 402 (2007)
- [2] <http://tools.invitrogen.com>
- [3] Chang D. E, Sørensen A. S., Demler E. A. and Lukin M. D. *Nature Phys.* **3**, 807 (2007)

- [4] Chang D. E, Sørensen A. S., Hemmer P.R. and Lukin M. D. *Phys. Rev. Lett.* **97**, 053002 (2006)
- [5] Atwater H. A. *Sci. Am.* **296**, 56 (2007)
- [6] Genet C. and Ebbesen T. W. *Nature* **445**, 39 (2007)
- [7] Sanders A. W. et al. *Nano Lett.* **6**, 1822 (2006)
- [8] Ditlbacher Harald, Hohenau Andreas, Wagner Dieter, Kreibig Uwe, Rogers Michael, Hofer Ferdinand, Aussenegg Franz R., and Krenn Joachim R. *Phys. Rev. Lett.* **95**, 257403 (2005)
- [9] Raether H, Surface Plasmons, Berlin, Springer (1988)
- [10] Ritchie R. H. *Phys. Rev.* **106**, 874 (1957)
- [11] Stern E. A. and Ferrell R. A. *Phys. Rev.* **120**, 130 (1960)
- [12] Barnes William L., Dereux Alain, and Ebbesen Thomas W. *Nature* **424**, 824 (2003)
- [13] Boardman A D ed. *Electromagnetic Surface Modes*, New York, Wiley (1982)
- [14] Kreibig U and Vollmer M *Optical Properties of Metal Clusters*, Berlin, Springer (1995)
- [15] Shchegrov A V, Novikov I V and Maradudin A A *Phys. Rev. Lett.* **78** 4269 (1997)
- [16] Xiao M, Zayats A V and Siqueiros J *Phys. Rev. B* **55** 1824 (1997)
- [17] Moskovits M *Rev. Mod. Phys.* **57** 783 (1985)
- [18] Ponath H-E and Stegeman G I (eds.) *Nonlinear Surface Electromagnetic Phenomena*, Amsterdam, North-Holland (1991)

- [19] Shalaev V M *Nonlinear Optics of Random Media*, Berlin, Springer (2000)
- [20] Ushioda S, Uehara Y and Kuwahara M *Appl. Surf. Sci.* **60** 448 (1992)
- [21] Smolyaninov I, Zayats A and Davis C *Phys. Rev. B* **56** 9290 (1997)
- [22] Zayats A V and Sandoghdar V *Opt. Commun.* **178** 245 (2000)
- [23] Malshukov A G *Phys. Rep.* **194** 343 (1990)
- [24] Zayats A V *Opt. Commun.* **161** 156 (1999)
- [25] Mills D L *Phys. Rev. B* **65** 125419 (2002)
- [26] Becker M. , Sivakov V., Andrä G., Geiger R., Schreiber J., Hoffmann S., Michler J., Milenin A. P., Werner P., and Christiansen S. H. *Nano Letters* **7**, 75 (2007)
- [27] Christiansen S H, Chou J W, Becker M, Sivakov V, Ehrhold K, Berger A, Chou W C, Chuu D S, Gösele U *Nanotechnology* **20**, 165301 (2009)
- [28] Chou J W, Lin K C, Lee Y J, Yuan C T, Hsueh F K, Shih H C, Fan W C, Luo C W, Lin M C, Chou W C, Chuu D S *Nanotechnology* **20**, 305202 (2009)
- [29] Chou J W, Lin K. C. , Tang Y. T., Lee Yao-Jen, Luo C.W., Chen Y. N, Yuan C. T., Shih Hsun-Chuan, Lin M. C. , Chou W. C. , Chuu D. S. *Nanotechnology* **20**, 415201 (2009)
- [30] Joannopoulos J D, Meade R D and Winn J N *Photonic Crystals*, Princeton, NJ: Princeton University Press (1995)
- [31] Agranovich V M and Mills D L (eds.) *Surface Polaritons*, Amsterdam, North-Holland (1982)
- [32] Reddick R C, Warmack R J and Ferrel T L *Phys. Rev. B* **39** 767 (1989)

- [33] Courjon D, Sarayeddine K and Spajer M *Opt. Commun.* **71** 23 (1989)
- [34] Fornel F. de , Goudonnet J P, Salomon L and Lesniewska E *Proc. SPIE* **1139** 77 (1989)
- [35] Marti O, Bielefeldt H, Hecht B, Herminhaus S, Leiderer P and Mlynek J *Opt. Commun.* **96** 225 (1993)
- [36] Adam P M, Salomon L, de Fornel F and Goudonnet J P *Phys. Rev. B* **48** 2680 (1993)
- [37] Dawson P, de Fornel F and Goudonnet J P *Phys. Rev. Lett.* **72** 2927 (1994)
- [38] Tsai D P, Kovasc J, Wang Z, MoskovitsM, ShalaeV V M, Suh J S and Botet R *Phys. Rev. Lett.* **72** 4149 (1994)
- [39] Bozhevolnyi S I, Smolyaninov I I and Zayats A V *Phys. Rev. B* **51** 17916 (1995)
- [40] Bozhevolnyi S I, Vohnsen B, Smolyaninov I I and Zayats A V *Opt. Commun.* **117** 417 (1995)
- [41] Bozhevolnyi S I, Vohnsen B and Zayats A V *Optics at the Nanometer Scale* ed M Nieto-Vesperinas and N Garcia, Dordrecht, Kluwer Academic, p 163 (1996)
- [42] Hecht B, Bielefeldt H, Novotny L, Inouye Y and Pohl D W *Phys. Rev. Lett.* **77** 1889 (1996)
- [43] Laks B, Mills D L and Maradudin A A *Phys. Rev. B* **23** 4965 (1981)
- [44] Glass N E, Weber M and Mills D L *Phys. Rev. B* **29** 6548 (1984)
- [45] Barnes W L, Preist T W, Kitson S C and Sambles J R *Phys. Rev. B* **54** 6227 (1996)
- [46] Salomon L, Grillot F, de Fornel F and Zayats A V *Phys. Rev. Lett.* **86** 1110 (2001)



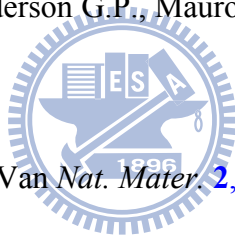
- [47] Bozhevolnyi S I, Erland J, Leosson K, Skovgaard P M W and Hvam J M *Phys. Rev. Lett.* **86** 3008 (2001)
- [48] Smolyaninov I I, Zayats A V, Stanishevsky A and Davis C C *Phys. Rev. B* **66** 205414 (2002)
- [49] Sivakov V., Andrä G., Gösele U., and Christiansen S. *phys. stat. sol. (a)* **203**, 15, 3692 (2006)
- [50] Sivakov V., Andrä G., Himcinschi C., Gösele U., Zahn D. R. T., Christiansen S. *Appl. Phys. A* **85**, 311 (2006)
- [51] Vladimir Sivakov, Frank Heyroth, Fritz Falk, Gudrun Andrä, Silke Christiansen *Journal of Crystal Growth* **300**, 288 (2007)
- [52] Wagner R.S., Ellis W.C. *Appl. Phys. Lett.* **4**, 89 (1964)
- [53] Schmidt Volker, Wittemann Joerg V., Senz Stephan, and Gösele Ulrich *Ade. Mater.* **21**, 2681 (2009)
- [54] Jin Jianming, *The Finite Element Method in Electromagnetics*, Second Edition, JOHN WILEY & SONS. INC. (2002)
- [55] Volakis John L., Chatterjee Arindam, Kempel Leo C., *Finite Element Method for Electromagnetics —antennas, microwave circuits, and scattering applications*, IEEE PRESS (1998)
- [56] Félidj N., Aubard J., Lévi G. *Phys. Rev. B* **65**, 075419 (2002)
- [57] Ibach Harald and Lüth Han, *Solid-State Physics —An Introduction to Principles of Materials Science*, Second Edition, Springer (2002)

- [58] Christiansen S. H., Becker M., Fahlbusch S., Michler J., Sivakov V., Andrae G., and Geiger R. *Nanotechnology* **18**, 035503 (2007)
- [59] Becker M., Sivakov V., Goesele U., Stelzner T., Andra G., Reich H. J., Hoffmann S., Michler J., and Christiansen S. H. *Small* **4**, 398 (2008)
- [60] Wang Y., Becker M., Wang L., Liu J., Scholz R., Peng J., Gösele U., Christiansen S., Kim D. H., Steinhart M. *Nano Lett.* **9**, 2384 (2009)
- [61] Tsang J. C., Kirtley J. R. and Bradley J. A. *Phys. Rev. Lett.* **43**, 772 (1979)
- [62] Lyon S. A. and Worlock J. M. *Phys. Rev. Lett.* **51**, 593 (1983)
- [63] Murray C. A., Allara D. L. and Rhinewine M. *Phys. Rev. Lett.* **46**, 57 (1981)
- [64] Nie Shuming and Emory Steven R. *Science* **275**, 1102 (1997)
- [65] Service Robert F. *Science* **319**, 718 (2008)
- [66] Maier Stefan A., Kik Pieter G., Atwater Harry A., Meltzer Sheffer, Harel Elad, Koel Bruce E., and Requicha Aria G. *Nature Material* **2**, 229 (2003)
- [67] Flätgen Georg, Krischer Katharina, Pettinger Bruno, Doblhofer Karl, Junkes Heinz, and Ertl Gerhard *Science* **269**, 668 (1995)
- [68] Zayats Anatoly V and Smolyaninov Igor I. *J. Opt. A: Pure Appl. Opt.* **5**, S16 (2003)
- [69] Pitarke J. M., Silkin V. M., Chulkov E. V. and Echenique P. M. *Rep. Prog. Phys.* **70**, 1–87 (2007)
- [70] Song Jung-Hoon, Atay Tolga, Shi Sufei, Urabe Hayato, and Nurmikko Arto V. *Nano Lett.* **5**, 1557 (2005)

- [71] Kneipp Kartrin, Moskovits Martin, and Kneipp Harald: *Surface-Enhanced Raman Scattering*, Springer (2006)
- [72] Chuang Wen-Hung, Wang Jyh-Yang, Yang C. C. and Kiang Yean-Woei *Appl. Phys. Lett.* **92**, 133115 (2008)
- [73] Shchegrov A V, Novikov I V and Maradudin A A *Phys. Rev. Lett.* **78** 4269 (1997)
- [74] Xiao M, Zayats A V and Siqueiros J *Phys. Rev. B* **55** 1824 (1997)
- [75] Agranovich V M, Kravtsov V E and Leskova T A *Solid State Commun.* **47** 925 (1983)
- [76] Kretschmann E and Raether H *Z. Naturf. A* **23** 2135 (1968)
- [77] Otto A *Z. Phys.* **216** 398 (1968)
- [78] Efros A.L. *Sov. Phys. Semicond.* **16**, 772 (1982)
- [79] Ekimov A.I. and Onushchenko A.A. *Sov. Phys. Semicond.* **16**, 775 (1982)
- [80] Alivisatos A.P. *J. Phys. Chem.* **100**, 13226 (1996)
- [81] http://en.wikipedia.org/wiki/Quantum_dot
- [82] Alivisatos A.P. *Science* **271**, 933 (1996)
- [83] Bruchez Jr. M., Moronne M., Gin P., Weiss S. and Alivisatos A.P. *Science* **281**, 2013 (1998)
- [84] Chan W.C.W., Nie S. *Science* **281**, 2016 (1998)
- [85] Qu L.H. and Peng X.G. *J. Am. Chem. Soc.* **124**, 2049 (2002)
- [86] Zhong X.H., Feng Y.Y., Knoll W. and Han M.Y. *J. Am. Chem.Soc.* **125**, 13559 (2003)
- [87] Bailey R.E. and Nie S.M. *J. Am. Chem. Soc.* **125**, 7100 (2003)

- [88] Kim S., Fisher B., Eisler H.J. and Bawendi M. *J. Am. Chem.Soc.* **125**, 11466 (2003)
- [89] Wehrenberg B.L., Wang C.J. and Guyot-Sionnest P. *J. Phys. Chem. B* **106**, 10634 (2002)
- [90] Silbey Robert J., Iberty Robert A. and Bawendi Mounji G., *Physical Chemistry*, 4thEdition, John Wiley & Sons, Page 835 (2005)
- [91] C. Pollock, *Fundamentals of Optoelectronics*, Irwin, Boston, MA (1995)
- [92] Huynh Wendy U., Dittmer Janke J. and Alivisatos A. *Paul Science* **295**, 2425 (2002)
- [93] Caruge J. M., Halpert J. E., Wood V., Bulović V. and Bawend M. G. *Nature Photonics* **2**, 247 (2008)
- [94] Grundmann M., Ledentsov N. N., Kirstaedter N., Heinrichsdorff F., Krost A., Bimberg D., Kosogov A. O., Ruvimov S. S., Werner P., Ustinov V. M., Kopév P. S. and Zh. I. Alferov *Thin Solid Films* **318**, 83 (1998)
- [95] Chen Y. N., Chen G. Y., Chuu D. S. and Brandes T. *Phys. Rev. A* **79**, 033815 (2009)
- [96] Kurucz Z., Sørensen M.W., Taylor J. M., Lukin M. D. and Fleischhauer M. *Phys. Rev. Lett.* **103**, 010502 (2009)
- [97] Wu X.Y., Liu H.J., Liu J.Q., Haley K.N., Treadway J.A., Larson J.P., Ge N.F., Peale F. and Bruchez M.P. *Nat. Biotechnol.* **21**, 41 (2003)
- [98] Parak W.J., Gerion D., Zanchet D., Woerz A.S., Pellegrino T., Micheel C., Williams S.C., Seitz M., Bruehl R.E., Bryant Z., Bustamante C., Bertozzi C.R. and Alivisatos A.P. *Chem. Mater.* **14**, 2113 (2002)
- [99] Pathak S., Choi S.K., Arnheim N. and Thompson M.E. *J. Am. Chem. Soc.* **123**, 4103 (2001)

- [100] Auman E.R., Anderson G.P., Tran P.T., Mattoussi H., Charles P.T. and Mauro J.M. *Anal. Chem.* **74**, 841 (2002)
- [101] Willard D.M., Carillo L.L., Jung J. and Orden A. Van *Nano Lett.* **1**, 469 (2001)
- [102] Clapp A.R., Medintz I.L., Mauro J.M., Fisher B.R., Bawendi M.G. and Mattoussi H. *J. Am. Chem. Soc.* **126**, 301 (2004)
- [103] Auman E.R., Clapp A.R., Anderson G.P., Uyeda H.T., Mauro J.M., Medintz I.L. and Mattoussi H. *Anal. Chem.* **76**, 684 (2004)
- [104] Lingerfelt B.M., Mattoussi H., Auman E.R., Mauro J.M. and Anderson G.P. *Anal. Chem.* **75**, 4043 (2003)
- [105] Tran P.T., Auman E.R., Anderson G.P., Mauro J.M. and Mattoussi H. *phys. stat. sol. (b)* **229**, 427 (2002)
- [106] Willard D.M. and Orden A. Van *Nat. Mater.* **2**, 575 (2003)
- [107] Dubertret Benoit, Skourides Paris, Norris David J., Noireaux Vincent, Brivanlou Ali H. and Libchaber Albert *Science* **298**, 1759 (2002)
- [108] Michalet X., Pinaud F. F., Bentolila L. A., Tsay J. M., Doose S., Li J. J., Sundaresan G., Wu A. M., Gambhir S. S. and Weiss S. *Science* **307**, 538 (2005)
- [109] Dahan Maxime, Lévi Sabine, Luccardini Camilla, Rostaing Philippe, Riveau Béatrice and Triller Antoine *Science* **302**, 442 (2003)
- [110] Chang D.E., Sørensen A.S., Hemmer P.R., Lukin M.D. *Phys. Rev. Lett.* **97**, 053002 (2006)



Chapter 2 Experiments and Techniques

In this chapter, we will introduce the experimental systems and techniques including Micro-Raman spectrometer, fluorescence lifetime image, the Scan Near field Optical Microscope (SNOM), and the reflectance spectrometer system.

§ 2-1 Micro-Raman Spectrometer

The Micro-Raman spectrometer (Jobin Yvon LabRam HR800 [1]) is used during our photo luminescence (PL) experiments (illustrated in chapter 4) and Surface Enhanced Raman Scattering (SERS) experiments (illustrated in chapter 7). Fig. 2.1 describes the simplified optical path of the apparatus [1]. He-Ne (633nm) laser is set as the incident source for the PL (and the SERS) measurement, the objective we used is $\times 100$ (and for the SERS $\times 50$), and the laser power through the density filter is down to ~ 3 mW (and for the SERS ~ 0.45 mW). After the excitation laser spot is focused (in the normal direction) on the sample (for fluorescence PL: spin-coated the highly dilute quantum dots (QDs) solution on the Au caps on silicon nanowires (SiNWs), and for the SERS: dilute crystal violet (CV) aqueous solution on the Au coated silicon nanorods (SiNRs)). The entrance filter is for purifying the laser source, while the notch filter is for filtering out the laser and getting the fluorescence PL (and the SERS) signals from the samples. The fluorescence PL (and the SERS) signals pass through the notch filter and go to the turning grating, and then collected by the charge couple device (CCD) and translated to electric signals for analyzing. In Figs. 2.2-2.3 [1], pictures of the apparatus side view I and II are shown.

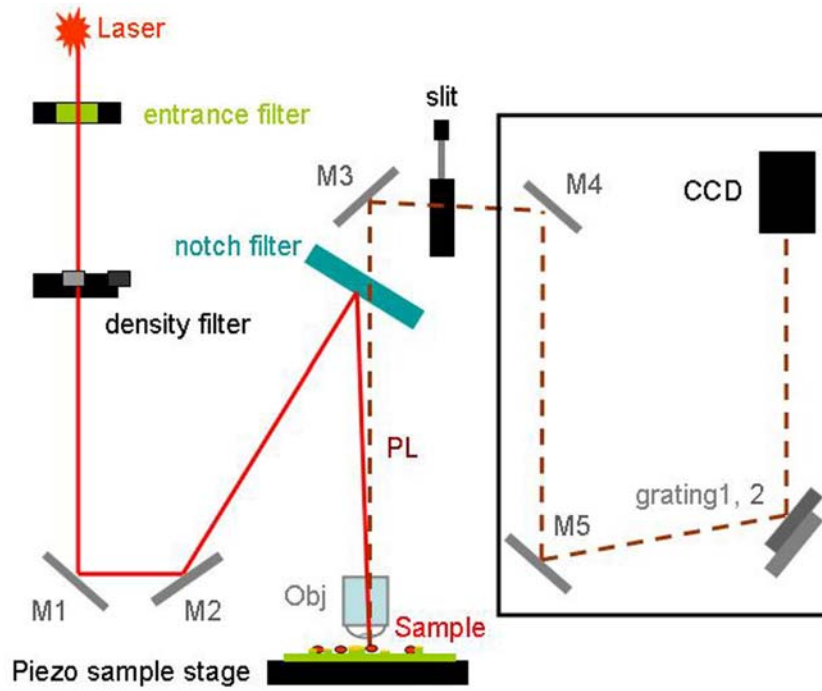


Fig. 2.1 Optical path simple description of the Micro-Raman spectrometer. M1, 2, 3, 4, 5 are mirror1, 2, 3, 4, 5, and obj is the objective. The minimum step of the piezo sample stage is 20 nm [1].

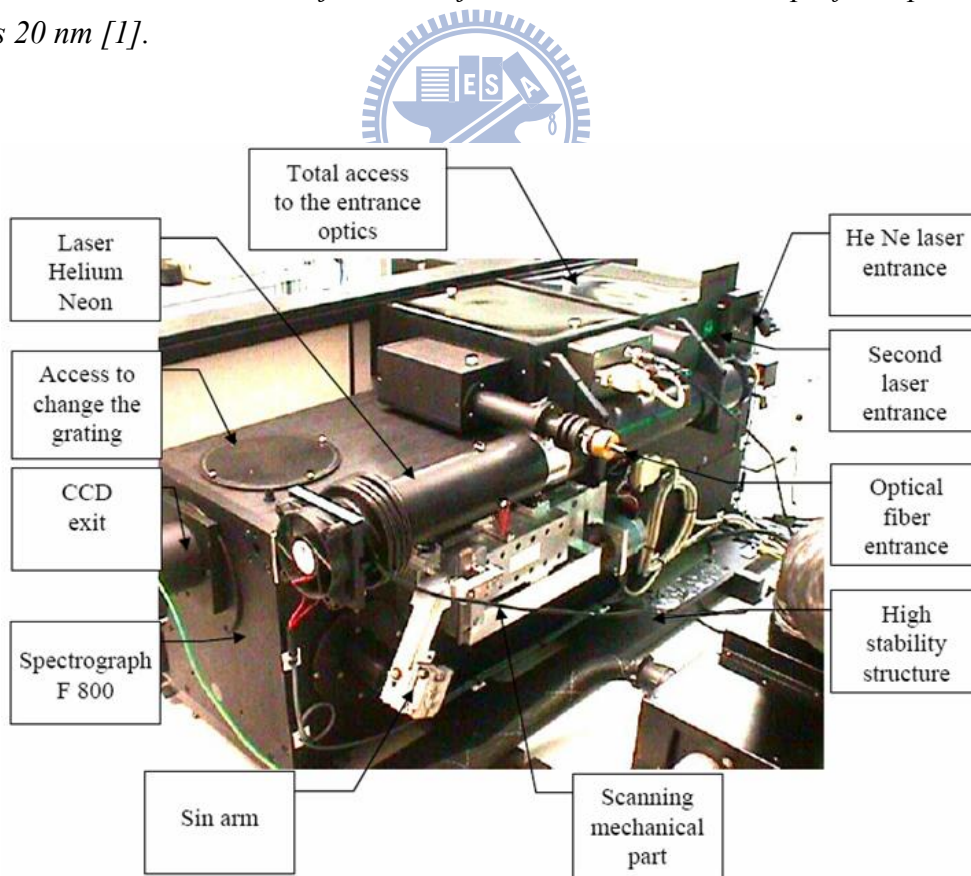


Fig. 2.2 Jobin Yvon LabRam HR800, side view I [1]

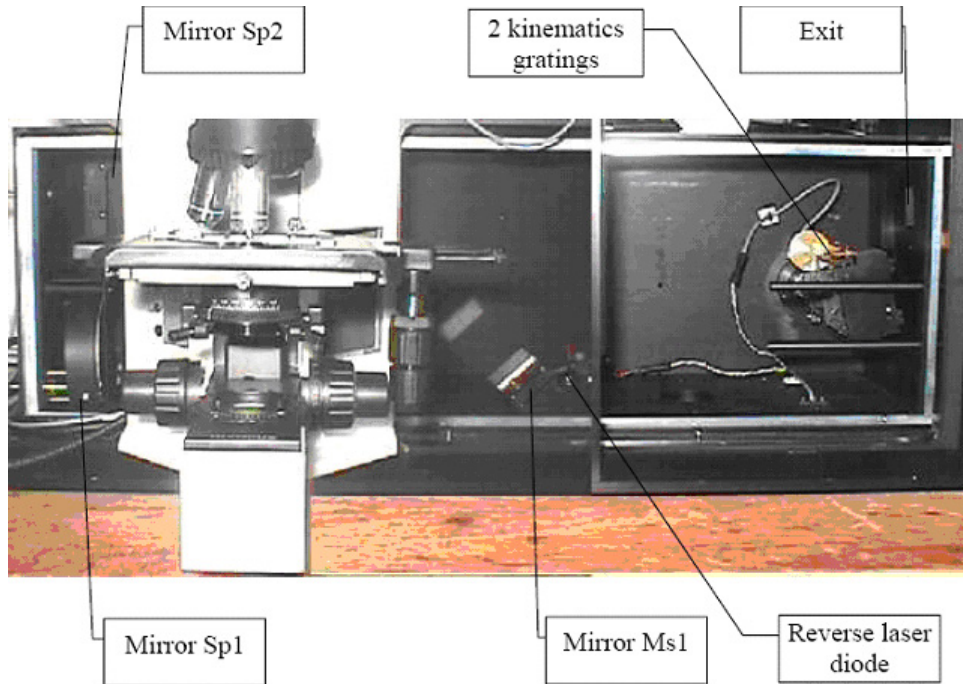


Fig. 2.3 Jobin Yvon LabRam HR800, side view II [1]

§ 2-2 Fluorescence Lifetime Imaging Microscopy

The fluorescence lifetimes of the QDs on the different sample surfaces used in our experiments (illustrated in chapter 4 and chapter 6) were measured by the apparatus shown in Figs. 2.4-2.5 [2].

The excitation laser (picosecond pulsed diode laser, repetition frequency: 10 MHz, wavelength 405 nm, power $\sim 0.13 \mu W$, pulse width 50 ps) directed by an optical fiber is led into the main optical unit and collected by a collimating lens, and then reflected by a mirror. After the laser reaching the partly reflected/ partly transmitted (R/T) mirror, it is partly reflected to a photo diode which is used for measuring the excitation laser power, and partly transmitted and then reflected by the dichroic mirror and led into the objective (Olympus UPlanSAPO 100xoil, $NA = 1.4$) connected to a computer controlled piezo-scanner (spatial resolution: nm precision) in the microscope (Olympus IX71). After

the excitation laser spot focused on the QDs, it possibly generates an electron-hole pair. After the excitation (in an order of $\sim ns$), the electron-hole pair may have a chance to recombine and emit fluorescence.

The fluorescence collected by the same objective is led into the main optical unit. In the main optical unit, the dichroic mirror which is used for reflecting the excitation laser and letting the fluorescence passing by. The excitation laser is reflected to reach the R/T mirror again, and then led into the charge-coupled device (CCD), which is used for monitoring the laser focus pattern. The fluorescence goes through a long pass 500 nm filter, and then passes through a pin hole ($50 \mu m$) and is expanded by two lenses. Finally, the expanded fluorescence goes through a filter for purifying and then focused by a lens before reaching a single photon avalanche photodiode (SPAD, response time is about 400 ps) which turns the light signal into the electric signal for TTTR (Time-Tagged Time-Resolved) analysis.

Time-Correlated Single Photon Counting (TCSPC) histogram of QDs fluorescence is obtained from TTTR provided by PicoQuant. Every 100 ns, there is a laser pulse impinges on the target. After 60 s, there are 6×10^8 excitation cycles which produce $10^6 \sim 10^7$ counts of fluorescence (for our QDs samples). These are abundant for statistic. TCSPC histograms are formed by recording the correlated time (the excitation laser trigger time correlated to single photon arrival SPAD time) of each single photon produced in each excitation cycle, and accumulating single photon numbers in a bin time for all cycles. According to TCSPC histograms, some of the fluorescence intensities of the QDs can be nicely fitted by single exponential decay: $I(t) = A_0 + A_1 e^{-t/\tau_1}$. Where $I(t)$ is the intensity (counts) at the time t , A_0 and A_1 representing the number of photons (given by counts) that were collected. τ_1 is the lifetime of a QD.

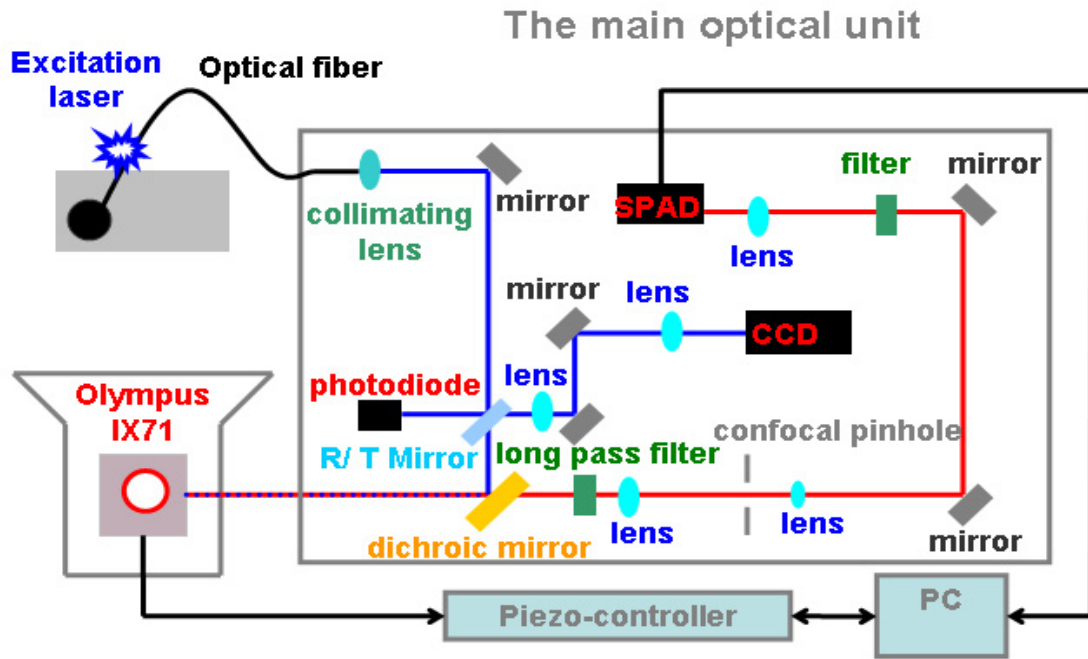


Fig. 2.4 The schematic diagram of fluorescence images and the lifetime measurement system [2]. R/T Mirror is the reflection/transmission mirror.

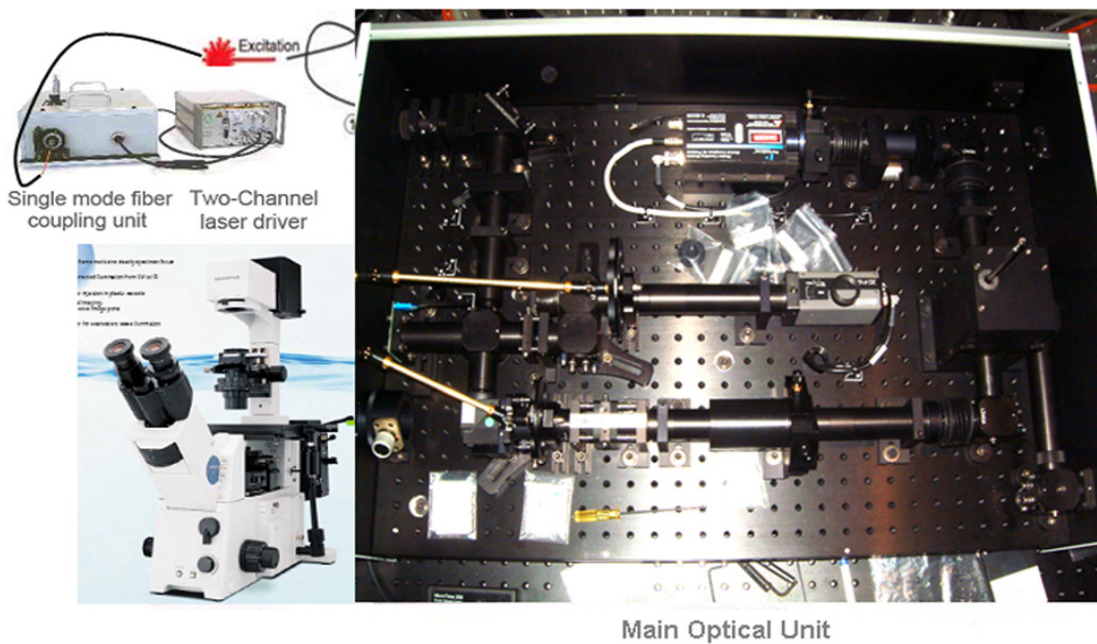


Fig. 2.5 The fluorescence images and the lifetime measurement system [2]

§ 2-3 Scanning Near-Field Optical Microscope

The idea for SNOM (also named Near-Field Scanning Optical Microscope (NSOM)) was first proposed by E. H. Synge in 1928 [3]. An imaging instrument originated from the concept of exciting and collection diffraction in the near field was first developed by Ash and Nichols in 1972 [4], the diffraction limit (expressed by the Rayleigh criterion: $d = 0.61 \frac{\lambda}{NA}$, where d is the minimum resolution, λ is the wavelength in vacuum and $NA = n \sin \theta$ is the numerical aperture for the optical component. n is the index of refraction of the medium where the lens is working in, and θ is the half-angle of the maximum cone of light incident into the lens) was first broken [5]. Later, Pohl et al. and Lewis et al. developed a NSOM (resolution can reach $\sim \lambda/20$) with a metal coated aperture at the tip of a sharp probe, and a feedback system [6-7].

Instrument picture of the NSOM (Aurora-3), schematic of the light paths, tuning fork mechanism and the AFM tip are shown in Fig. 2.6 [8]. The Excitation laser source in an NSOM system is led into an optical fiber. The end of the fiber sharpened to a diameter of ~ 50 nm and coated with aluminum (approximately 100 nm thick) as a tip. A scanning probe microscope (SPM) equipped in an NSOM is comprised of a sensing probe (for scanning across the sample surface), piezoelectric ceramics (for positioning the sample), an electronics control unit and a computer (for controlling the scan parameters and generating images). A SPM has provided the technology needed to maintain the tip-sample spacing (typically less than 10 nm) while a tip scanning over a sample. Two modes (with different relative positions of photo detectors), transmission mode and reflection mode are available for different sample types in the SPM. Photo detectors are placed behind the sample (or beside the tip) for transmission mode (or for reflection mode) to collect light emitted from the sample. In the experiment illustrated in chapter 5, we use the reflection mode. A sensor

(with very high spatial resolution, and can sense height changes $\sim 0.1 \text{ \AA}$) is another important component in the SPM. There are two imaging modes (defined by the types of the sensor): Scanning Tunneling Microscopy (STM) and Atomic Force Microscopy (AFM) in the SPM. In our experiment (illustrated in chapter 5), the Aurora-3 operates in AFM non-contact mode and uses a tuning fork mechanism (a tuning fork mounted alongside the tip and made to oscillate at its resonance frequency) as a sensing probe. The AFM and NSOM images are simultaneously obtained. The excitation light is locally illuminated by a nano-aperture ($\sim 80 \text{ nm}$), the diameter of the fiber tip is about 250 nm , and the near-field signals were collected by an objective at the 45° normal to the sample surface.

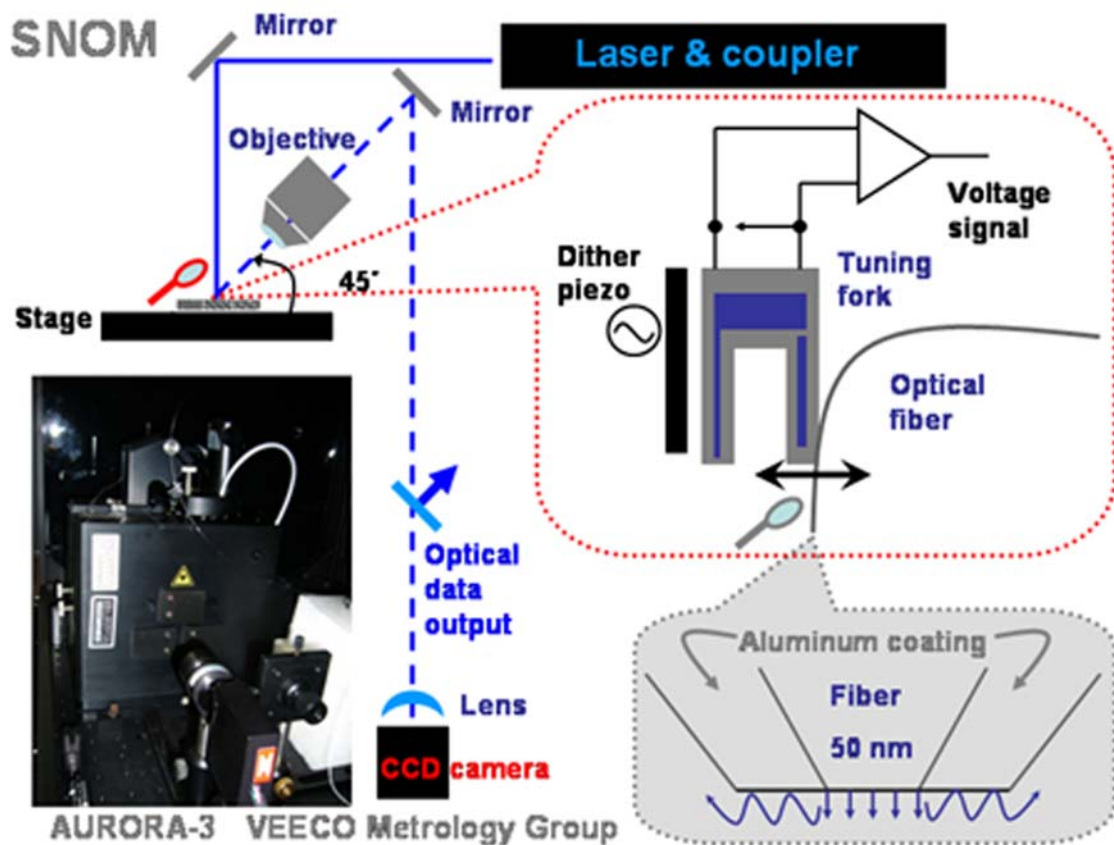


Fig. 2.6 Instrument picture of the scan near field optical microscope (SNOM), schematic of the light paths, tuning fork mechanism and the AFM tip (very close to the sample $< 10 \text{ nm}$) are shown. The AFM image and the laser light reflection were obtained simultaneously. [8]

§ 2-4 Reflectance Spectrometer

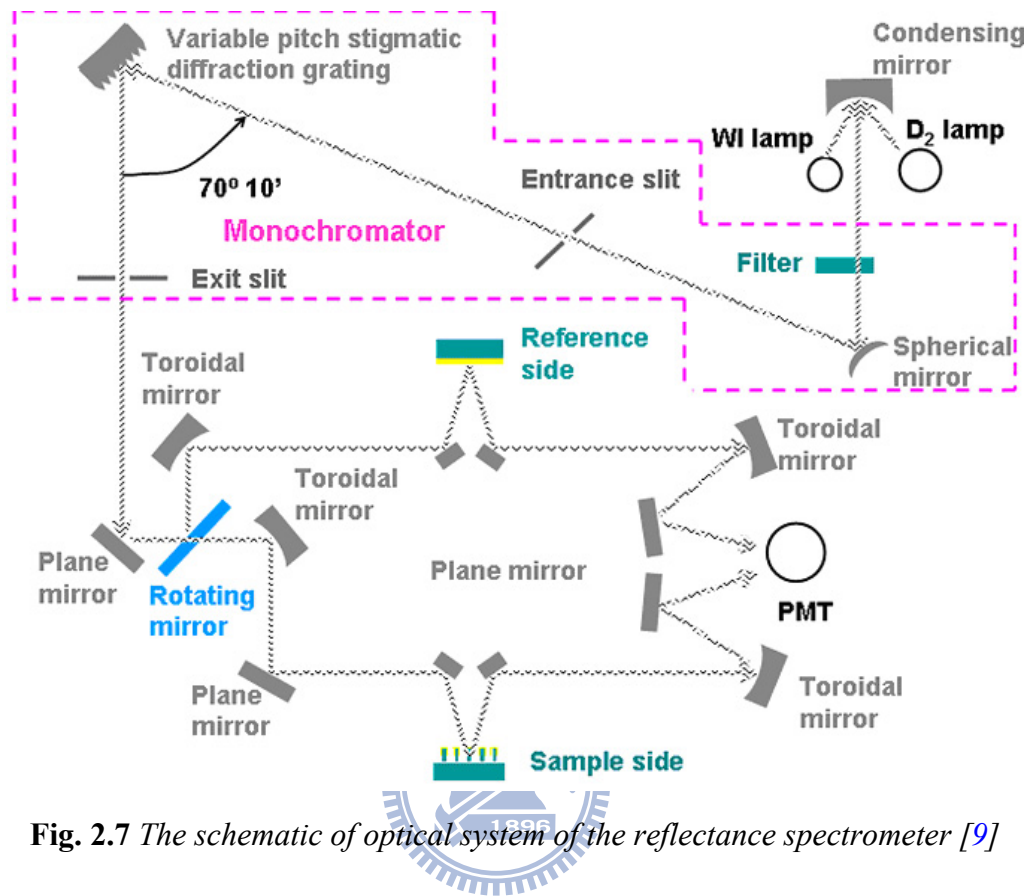


Fig. 2.7 The schematic of optical system of the reflectance spectrometer [9]

The spectrometer (Model U-3010 [9]) is used for reflectance analysis of liquid, solid and gaseous samples in the ultraviolet-visible region (wavelength: 190 nm ~ 900 nm). Our relative experiments (Au coated SiNR array structures reflectance spectra) will be illustrated in chapter 5, 6 and 7. The optical system of the spectrometer is shown in Fig. 2.7 [9]. A light from the light source (the tungsten iodide (WI) lamp: in the visible region; the Deuterium (D₂) lamp: in the ultraviolet region) is selected automatically by the light source switching mirror (optionally selectable in a range of 325 to 370 nm) according to the measurement wavelength. Then, the selected light passed a filter, reflected by a spherical mirror, passed an entrance slit, and let to the monochromator. The monochromator (with variable pitch stigmatic diffraction grating; the grating constant: 1/600 mm) is employing

unique stigmatic concave grating. After passed an exit slit, the monochromatic beam is branched into the reference beam and the sample beam (the reference beam and the sample beam are included in the sample compartment) by a group of sector mirrors (including two plane mirrors, two toroidal mirrors, and a rotating mirror). The beams which have passed through the sample compartment are let by two toroidal mirrors and two plane mirrors, and finally irradiated into the detector (the Photomultiplier tube (PMT)). The reflection value is obtained from the intensity value from the sample side/ the intensity value form the reference side.

Reference:

- [1] HORIBA JOBIN YVON, HR800 *User manual*
- [2] <http://www.picoquant.com>
- [3] http://www.nanonics.co.il/index.php?page_id=149A
- [4] Ash E.A. and Nicholls G. *Nature* **237**, 510 (1972)
- [5] http://en.wikipedia.org/wiki/Near-field_scanning_optical_microscope
- [6] Lewis A., Isaacson M., Harootunian A., and Murray A. *Ultramicroscopy* **13**, 227 (1984)
- [7] Pohl D.W., Denk W., and Lanz M. *Appl. Phys. Lett.* **44**, 651 (1984)
- [8] AURORA-3 *Instrument User Guide*
- [9] *Instruction manual model U-2010/U-3010/U3310 spectrometer (maintenance manual)*, Hitachi-High Technologies Corporation 2001, 6th Edition (2005)



Chapter 3 The Finite Element Method

The finite element method (FEM) [1-2] is commonly used for solving the partial differential equations over complicated domains and thus is a good choice for a wide class of problems. By breaking up the computational domain into elements (usually elements with simple shapes expressed by basic functions) and solving the unknown function within, one can approximately solve the partial differential equations over domains even with complicated geometries. For two-dimensional (2D) problems, the triangles or quadrilaterals elements are typically chosen. Segmenting the computational domain into small elements is called meshing. The meshing size should be tinny enough to ensure that the field interior to the meshing element can be approximated with sufficient exactness.

By the FEM, the approximations of the partial differential equations expressed by the expansions of unknown coefficients combined with the boundary conditions of each element lead to a matrix system of the form:

$$[A]\{x\} = \{b\}, \quad (3.1)$$

where the matrix $[A]$ is square of size $N \times N$, very sparse due to the continues properties on each joint (joint of two neighboring segments), and $\{b\}$ is a column matrix determined on the basis of the boundary conditions or the forced excitation (current source, incident field, etc.) [2]. After Eq. (3.1) constructed, its solution proceeds easily with the application of an iterative or direct solver.

Based on the electromagnetic theory, 2D FEM simulations are suitable for carrying out the near-field optical properties, especially the field distribution of the array structures. The localized surface plasmon (LSP) resonance modes relative topics in our research were investigated by this method (illustrated in chapter 4, 5, 6 and 7). We used the scattered harmonic propagation model provided by FEMLAB (www.femlab.de). The model solves

the electromagnetic fields based on Maxwell's equations. For the example of TM incident mode, the z component of scattered field E_z^{scat} in 2D (x-y) surface can be solved by:

$$\nabla \cdot \left(\frac{1}{\mu_r} \nabla E_z^{scat} \right) - k_0^2 \varepsilon_r E_z^{scat} = -\nabla \cdot \left(\frac{1}{\mu_r} \nabla E_z^i \right) - k_0^2 \varepsilon_r E_z^i + i\omega\mu_0 J_{iz}. \quad (3.2)$$

Where ε_r is the relative permittivity, μ_r is the relative permeability, ω is the angular frequency, μ_0 is the permeability in vacuum, k_0 is the wave number in vacuum. E_z^i is the z component of the incident electric field generated by $\hat{z}J_{iz}$. Where $\hat{z}J_{iz}$ is the electric current source (or can be assumed as the excitation source).

To describe the FEM, the FEM will be illustrated by an one-dimensional (1D) example [2] in the following. The Sturm-Liouville problem which can be used to describe the potential or the electric field between the parallel plates will be used as the example to describe the method. The Sturm-Liouville equation is described as

$$-\frac{d}{dx} \left(p(x) \frac{dU(x)}{dx} \right) + q(x)U(x) = f(x), 0 < x < x_a. \quad (3.3)$$

Where $U(x)$ is an unknown function (can be the potential or the electric field between the parallel plates), $p(x)$ and $q(x)$ are known functions. In order to solve the Sturm-Liouville problem by the FEM, we illustrate a weighted residual method for the approximation in every segment of the interested 1D line (x). Inside every segment (labeled as segment "m"), the following condition must be satisfied.

$$\int_{\text{Domain: } W_m} W_m(x) R(x) dx = 0, \quad (3.4)$$

$$R(x) = -\frac{d}{dx} \left(p(x) \frac{dU(x)}{dx} \right) + q(x)U(x) - f(x), \quad (3.5)$$

Where $W_m(x)$ is the weighting function which must be chosen under the restriction of

$$\int_0^{x_a} \left\{ [W_m(x)]^2 + \left[\frac{d}{dx} W_m(x) \right]^2 \right\} dx < \infty \quad (3.6)$$

to prevent from the numerical errors (due to the divergence). $R(x)$ is the residual function original from Eq. (3.3).

Substitute Eq. (3.5) into (3.4), and use the technique of integration by part, the weak form equation in the region $0 \sim x_a$ is obtained:

$$\int_0^{x_a} \left[p(x) \frac{dW_m}{dx} \frac{dU}{dx} + q(x) W_m(x) U(x) - W_m(x) f(x) \right] dx - \left[p(x) W_m(x) \frac{dU}{dx} \right]_0^{x_a} = 0. \quad (3.7)$$

Let

$$U(x) = \sum_{e=1}^{N_e} \sum_{i=1}^2 U_i^e N_i^e(x), \quad (3.8)$$

$$\text{where } N_1^e(x) = \begin{cases} \frac{x_2^e - x}{x_2^e - x_1^e}, & x_1^e < x < x_2^e \\ 0, & \text{otherwise} \end{cases}, N_2^e(x) = \begin{cases} \frac{x - x_1^e}{x_2^e - x_1^e}, & x_1^e < x < x_2^e \\ 0, & \text{otherwise} \end{cases}. \quad (3.9)$$

And then, substitute Eq. (3.9) into Eq. (3.8), one obtains

$$U(x) = \sum_{e=1}^{N_e} \left[U_1^e \frac{x_2^e - x}{x_2^e - x_1^e} + U_2^e \frac{x - x_1^e}{x_2^e - x_1^e} \right] \quad (3.10)$$

In Eqs. (3.8)-(3.10), the superscript “e” is for the eth element, and the lower index “i” (1 or 2) are the two end points of a segment. For example, U_1^e and U_2^e are the two unknowns of the eth segment. The figure for explaining the eth segment and the linear shape functions is shown in Fig. 3.1.

Finally, let $W_m = N_j$, the following equation can be obtained:

$$[A_{ij}] \{U_i^e\} + \text{endpoint} \Big|_0^{x_a} = \{b_i^e\} \quad (3.11)$$

where

$$A_{ij}^e = \int_{x_1^e}^{x_2^e} \left[p(x) \frac{dN_i^e(x)}{dx} \frac{dN_j^e(x)}{dx} + q(x) N_i^e(x) N_j^e(x) \right] dx, [A_{ij}^e] = \begin{bmatrix} A_{11}^e & A_{12}^e \\ A_{21}^e & A_{22}^e \end{bmatrix}, \text{ and}$$

$$b_i^e = \int_{x_1^e}^{x_2^e} N_i^e(x) f(x) dx. \text{ Every } U_i^e \text{ can be solved by Eq. (3.11).}$$

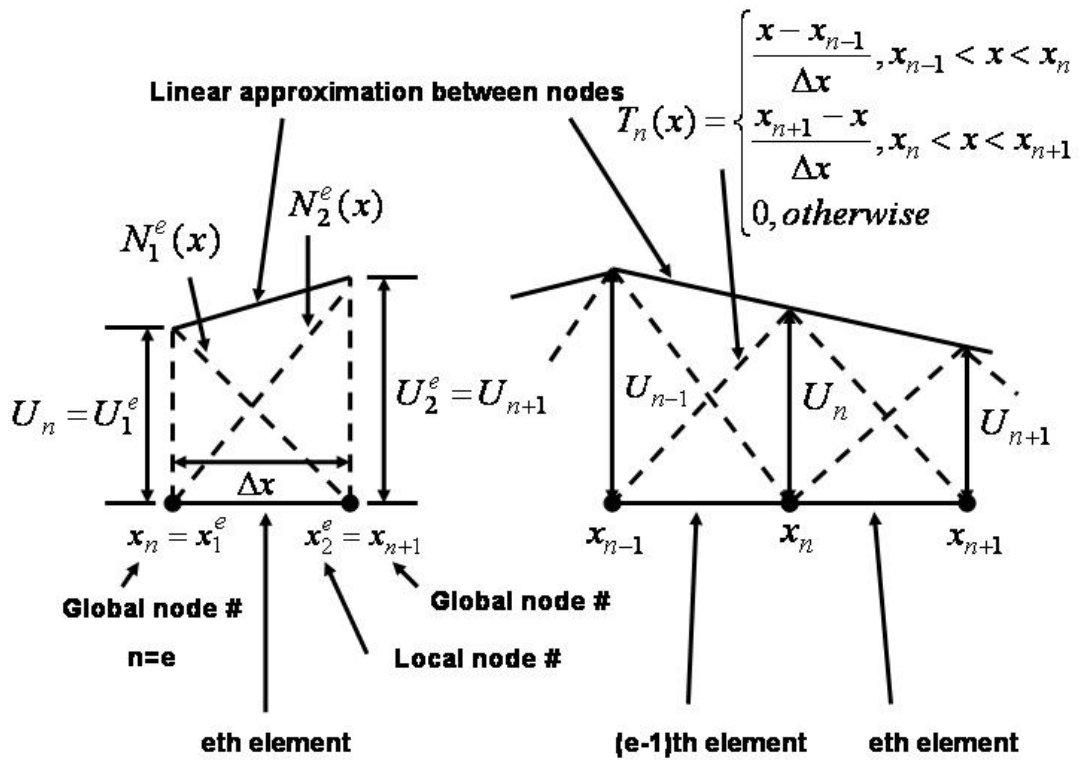
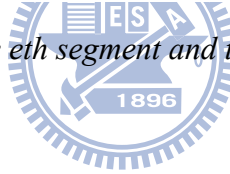


Fig. 3.1 Illustration of the eth segment and the linear shape functions. [2]



If there are N elements of an interested line segment, there are $N-1$ nodes in between. If each element contains two unknowns (U_1^e and U_2^e), N elements will produce $2N$ unknowns. And between the neighboring two elements, the joint node must satisfy the continuous boundary condition. Since there are $N-1$ nodes inside the segment, number of unknowns is reduced to $N+1$. Reducing number of unknowns is an advantage of the FEM.

For 2D FEM, by the similar concept, one can start from the general form of the wave equation:

$$\nabla \cdot [p(x, y) \nabla U(x, y)] + k_0^2 q(x, y) U(x, y) = f(x, y). \quad (3.12)$$

Where $\nabla = \hat{x} \frac{\partial}{\partial x} + \hat{y} \frac{\partial}{\partial y}$, $\mathbf{r} = x\hat{x} + y\hat{y}$ is the position vector, $U(x)$ is an unknown function (can be the magnetic or the electric field), $p(x)$ and $q(x)$ are known functions and k_0 is the wave number in vacuum. The pertinent residual of Eq. (3.12) is:

$$R(x, y) = \nabla \cdot p(\mathbf{r})\nabla U(\mathbf{r}) + k_0^2 q(\mathbf{r})U(\mathbf{r}) - f(\mathbf{r}). \quad (3.13)$$

In order to derive the weak form over the domain of each element, let

$$\iint_{\text{Domain } : W(\mathbf{r})} W(\mathbf{r})R(\mathbf{r})dxdy = 0. \quad (3.14)$$

Where $W(\mathbf{r})$ is the weighting function which must be compatible with the boundary conditions and be square integratable over the domain (just like in 1D calculations) [2]. And use the identity of Eq. (3.15),

$$W\nabla \cdot p\nabla U = \nabla \cdot (pW\nabla U) - p\nabla W \cdot \nabla U \quad (3.15)$$

and the technique of integration by part

$$\iint_{\Omega} \nabla \cdot (pW\nabla U) ds = \oint_C pW(\nabla U \cdot \hat{n}) dl. \quad (3.16)$$

In which Ω indicates the pertinent computational domain, C is the contour enclosing Ω , and \hat{n} is the outward directed unit normal vector to the contour C as shown in Fig. 3.2. Use Eq. (3.15) (3.16) and (3.14), the weak form of the 2D scalar wave equation is obtained in the following:

$$\iint_{\Omega} [-p(\mathbf{r})\nabla W(\mathbf{r}) \cdot \nabla U(\mathbf{r}) + k_0^2 q(\mathbf{r})W(\mathbf{r})U(\mathbf{r}) - W(\mathbf{r})f(\mathbf{r})] ds + \oint_C p(\mathbf{r})W(\mathbf{r})[\hat{n} \cdot \nabla U(\mathbf{r})] dl = 0. \quad (3.17)$$

In order to use the weak form equation in every segment, a tessellation of the computational domain Ω in small triangular elements is chosen as illustrated in Fig. 3.2. And the following linear equation (Eq. (3.18)) is used to approximate the fields in each triangle.

$$U(x, y) = \sum_{e=1}^{N_e} \sum_{i=1}^3 U_i^e N_i^e(x, y) \quad (3.18)$$

, in which U_i^e are the unknown coefficients of the expansion and represent the field (or the potential values) at the nodes of each triangle, and

$$N_i^e(x, y) = \begin{cases} \frac{1}{2\Delta^e} (a_i^e + b_i^e x + c_i^e y), & \mathbf{r} \in \Omega^e \\ 0, & \text{otherwise} \end{cases} \quad (3.19)$$

is the shape function, where $a_i^e = x_j^e y_k^e - x_k^e y_j^e$, $b_i^e = y_j^e - y_k^e$, $c_i^e = x_k^e - x_j^e$, i, j, k follow the cyclical rule.

$$\Delta^e = \frac{1}{2} \det \begin{bmatrix} 1 & x_1^e & y_1^e \\ 1 & x_2^e & y_2^e \\ 1 & x_3^e & y_3^e \end{bmatrix} = \frac{1}{2} [(x_2^e - x_1^e)(y_3^e - y_1^e) - (x_3^e - x_1^e)(y_2^e - y_1^e)] \quad (3.20)$$

is the triangle area (as shown in Fig. 3.2.).

Substitute Eq. (3.18) in the weak form Eq. (3.17) to obtain

$$\begin{aligned} & \sum_{e=1}^{N_e} \sum_{i=1}^3 U_i^e \iint_{\Omega^e} [-p(\mathbf{r}) \nabla W(\mathbf{r}) \cdot \nabla N_i^e(\mathbf{r}) + k_0^2 q(\mathbf{r}) W(\mathbf{r}) N_i^e(\mathbf{r})] dx dy + \int_C p(\mathbf{r}) W(\mathbf{r}) \hat{\mathbf{n}} \cdot \nabla U(\mathbf{r}) dl \\ & = \iint_{\Omega^e} W(\mathbf{r}) f(\mathbf{r}) dx dy. \end{aligned} \quad (3.21)$$

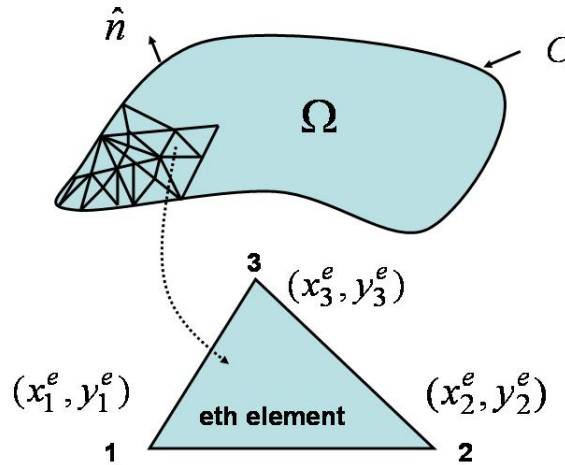


Fig. 3.2 The computation domain and node coordinates for the eth triangle. [2]

Let $W(x, y) = N_i^e(x, y)$, $i = 1, 2, 3$, substitute into Eq. (3.21) to obtain

$$\begin{aligned} & \sum_{i=1}^3 U_i^e \iint_{\Omega^e} \left[-p(\mathbf{r}) \nabla N_j^e(\mathbf{r}) \cdot \nabla N_i^e(\mathbf{r}) + k_0^2 q(\mathbf{r}) N_j^e(\mathbf{r}) N_i^e(\mathbf{r}) \right] dx dy + \int_C p(\mathbf{r}) N_j^e(\mathbf{r}) \hat{n} \cdot \nabla U(\mathbf{r}) dl \\ & = \iint_{\Omega^e} N_j^e(\mathbf{r}) f(\mathbf{r}) dx dy, \quad j=1,2,3. \end{aligned} \quad (3.22)$$

In which $N_j^e(x,y)$ is nonzero over eth element. If assume on C , the field satisfies the with Neuman boundary condition: $\hat{n} \cdot \nabla U = \frac{\partial U}{\partial n} = 0$, Eq. (3.22) can be expressed as the element matrix system (similar to Eq. (3.11)):

$$\begin{bmatrix} A_{11}^e & A_{12}^e & A_{13}^e \\ A_{21}^e & A_{22}^e & A_{23}^e \\ A_{31}^e & A_{32}^e & A_{33}^e \end{bmatrix} \begin{bmatrix} U_1^e \\ U_2^e \\ U_3^e \end{bmatrix} = \begin{bmatrix} b_1^e \\ b_2^e \\ b_3^e \end{bmatrix}. \quad (3.23)$$

Where $A_{ij}^e = -p^e \iint_{\Omega^e} \nabla N_i^e(\mathbf{r}) \cdot \nabla N_j^e(\mathbf{r}) dx dy + k_0^2 q^e \iint_{\Omega^e} N_i^e(\mathbf{r}) N_j^e(\mathbf{r}) dx dy, i=1,2,3, j=1,2,3$

and $b_j^e = \iint_{\Omega^e} N_j^e(\mathbf{r}) \cdot f(\mathbf{r}) dx dy, j=1,2,3.$

In 2D calculations, due to the complexities are much higher than that in 1D, we will need nod location table, triangle connectivity table and boundary element table to help us making things clear. The proper arrangement of groups for table will be helpful for shortening the time needed for solving our problems. More details about the process with examples can be found in [2]. Similar with in 1D process, between the neighboring two elements, the joint node must satisfy the continuous boundary condition.

Reference:

- [1] Jin Jianming, *The Finite Element Method in Electromagnetics*, Second Edition, JOHN WILEY & SONS. INC. (2002)
- [2] Volakis John L., Chatterjee Arindam, Kempel Leo C., *Finite Element Method for Electromagnetics —antennnas microwave circuits, and scattering applications*, IEEE PRESS (1998)

Chapter 4 Fluorescence signals of core-shell quantum dots enhanced by single crystalline gold caps on silicon nanowires

We use nanoscale (20 nm – 300 nm in diameter) single crystalline gold (Au) caps on silicon nanowires (SiNWs) grown by the vapour-liquid-solid (VLS) growth mechanism to enhance the photoluminescence (PL) signals of highly dilute core/shell CdSeTe/ZnS quantum dots (QDs) in aqueous solution (10^{-5} M). For nanowires (NWs) without Au-caps, as they appear e.g. after Au etching in aqua regia or buffered KI/I₂-solution, essentially no fluorescence PL signal of the same diluted QDs could be observed. PL signals were measured using excitation with a laser wavelength of 633 nm. The signal enhancement by single crystalline, nanoscale Au-caps is discussed and interpreted based on finite-element modelling (FEM).

§ 4-1 Introduction

Semiconductor QDs have optical and electronic properties which are strongly dependent on QD size, due to quantum confinement of the involved charge carriers [1, 2]. For two decades now, extensive research has been carried out to define and explore QD applications in optoelectronics and memory devices [3-5]. Only 10 years ago, Alivisatos et

al. could present a recipe to make QDs water-soluble so that QDs could thus be combined with biological molecules [6, 7], a finding that opened up additional options to integrate QDs in biological and medical studies. One of the important features of QDs is that the particle size determines many of the QD properties such as the wavelength of the fluorescence emission. By altering the QD size and its chemical composition, fluorescence emission may be tuned in a broad wavelength range of 400–2000 nm [8-12]. Given that fact, the utilization of QDs as fluorescent labels for biological macromolecules has attracted considerable attention. The current methods of producing QDs *via* chemical synthesis allow for excellent control over the mean particle size and particle size distribution allowing in the milli-gram or gram quantities of QDs where the particles exhibit narrow and symmetric emission peaks (FWHM typically in the few 10nm range). This is much better than the emission characteristics for typical organic dye molecules, which often have much broader and asymmetric emission profiles. This particular property of QDs is useful when simultaneous labelling and detection of multiple analytes is desired [13]. In addition to their controllable photon emission properties, QDs show advantageous absorption properties. Unlike organic dyes, which show large absorption cross-sections only across a narrow band of resonant frequencies, the relatively large densities of states and overlapping band structures in semiconductor materials result in QDs with high molar absorption capabilities and broad absorption spectra [14]. This property allows efficient excitation of multiple QD-based fluorophores with a single light source. The combination of large molar absorption capabilities and high quantum yield provides the basis for a series of QD-based fluorescent labels. In fact, studies comparing the brightness of single CdSe/ZnS core/shell QDs to that of single rhodamine 6G molecules indicate that the fluorescent photon flux in QDs is 10–100 fold larger [7]. Several other QD properties have significant practical implications for their use as fluorescent labels. E.g. their low photo-degradation rates make continuous or long-term monitoring of slow biological

processes possible (very challenging for traditional organic fluorophores) [7, 15]. The long fluorescence lifetimes of QDs, on the order of 10–50 ns, are advantageous for distinguishing QD signals from background fluorescence and for achieving high-sensitivity detection [6]. QD labels have successfully been used, as a replacement for organic dyes, for a variety of bio-analytical purposes, such as DNA hybridization detection [16, 17], immunoassays [18], and binding assays using fluorescence resonant energy transfer (FRET) to probe for target events [19 - 24]. In the area of biosensors, QDs are used for their long-term photo stability, allowing real-time and continuous monitoring.

In this study we use commercial core/shell CdSeTe/ZnS colloidal QDs in a dilute aqueous solution (10^{-5} M) that show fluorescence PL in a narrow energy range. We show that we are able to enhance the PL signal intensity by a factor larger than 100 by bringing the QDs in close vicinity to gold (Au)-caps which reside atop silicon nano-wires when grown Au-catalyzed following the VLS growth mechanism [25, 26] from the gas phase by evaporating silicon from a solid target using an electron beam [27, 28]. The PL signal enhancement is mediated by the electrical field enhancement at the nano-scale Au-caps. This optical near field phenomenon is discussed based on 2D FEM as are the implications for applications in the aforementioned fields.

§ 4-2 Experiment

We are interested in a PL study of QDs of a commercially available core/shell type, CdSeTe/ZnS [30], with 5.3 nm diameter at the low concentration of 10^{-5} M in aqueous solution. For the PL studies different substrates with the QD suspension were spin-coated with ~5000 rpm for several minutes. That way we expect to have well separated single QDs on the different substrate surfaces.

The PL measurements were carried out in a spectrometer of Jobin Yvon, LabRam HR800. using a He-Ne laser (wavelength 633 nm) for exciting fluorescence of the QDs. An objective of 100x magnification (numerical aperture: 0.9) was used. The laser power was reduced with the density filter down to ~ 3 mW. The entrance filter was used to filter out background light from the spectrum and the notch filter to remove the exciting laser light from the spectrum.

The Time-Correlated Single Photon Counting (TCSPC) measurements for single QDs sitting on SiNWs with and without Au-cap were carried out by using laser excitation by a picosecond pulsed diode laser with a repetition frequency of 10MHz operating at a wavelength of 405 nm, a power $\sim 0.13\mu W$ and a pulse width of $50ps$. The single QD excitation can be realized by directing the laser onto the sample by an optical fiber. After the excitation (of the order of $\sim ns$), the electron-hole pair that is excited recombines and emits a photon (fluorescence) that can be detected. The fluorescence signal goes through a long pass (500 nm) filter, and then passes through a pin hole ($50\mu m$) and is expanded by two lenses. Finally, the expanded fluorescence goes through a filter again and is then focused onto a single photon avalanche photodiode (SPAD, response time is about 400 ps) which turns the light signal into an electrical signal for Time-Tagged Time-Resolved (TTTR) analysis. With this experiment we study and compare the TCSPC of single QDs on SiNWs with and without Au-cap.

The SiNWs were grown by the Au-catalyzed VLS growth mechanism [25, 26] making use of the incorporation of silicon atoms in the epitaxially (with respect to the Si(111)-wafer substrate) growing SiNWs, evaporated by an electron-beam (EBE, electron beam evaporation) [27, 28]. The silicon substrate pieces were cleaned by rinsing in acetone for 5 min followed by an ethanol rinse for another 5min prior to nanowire growth. Native silicon dioxide layers were removed by etching with 40% HF for 30 s followed by a 2% HF rinse for 3 min. Finally, the samples were rinsed with de-ionized water and were blow

dried with nitrogen. This cleaning procedure yields hydrogen-terminated silicon surfaces (for a limited time of a few minutes), which allowed for subsequent deposition on an essentially oxide-free surface. Initially, a 2.4 nm thick Au film (EDWARDS, Sputter Coater S150 B) was sputtered on the cleaned, oxide-free wafers to create a continuous Au layer which disintegrates upon heating (above the eutectic temperature of Au-Si of 370°C) into Au-caps that catalyze straight SiNW growth on the Si(111) substrate wafer perpendicular to the sample surface. Then samples were heated for 30 min to temperatures of 650°C in the evacuated growth chamber (base pressure $2-5 \times 10^{-7}$ Torr) to produce the growth templates that consist of Au nanocaps on the oxide free Si substrates. The EBE system used for SiNW growth in this work was built in-house. The silicon is evaporated from a water cooled copper crucible using an electron beam at a beam current of 35-80 mA. The higher the evaporation current, the larger the growth velocities of the SiNWs [27]. All growth experiments were carried out for 10 min and 1h at 650°C and at a chamber pressure of $2-5 \times 10^{-7}$ Torr and an evaporation current of 80 mA. The growth rates of SiNWs under these conditions were in the range of at most 100 nm/min (achieved essentially on the virgin substrate at the beginning of the growth process) [28].

SiNWs and QDs were analyzed using scanning electron microscopy (SEM) in a conventional Jeol 6300F and a high resolution FEI Nova Nanolab 600 with in-lens detector that permits highest resolution of 1 nm at 15 kV and 5 mm working distance and still 2 nm at low voltages down to 1 kV at 1.5 mm working distance, i.e. sufficiently good to distinguish the 5.3 nm QDs. The SiNWs were moreover characterized by transmission electron microscopy (TEM) in a FEI CM200UT.

Finite element calculations [31] were carried out using the COMSOL software (www.femlab.de). Using this software the classical Maxwell's equation system especially the Helmholtz wave equation were solved with thin film experimental data of Johnson and Christie [29] as an input for the dielectric material's response. This approach allows to

delineate comparably realistically the geometrical appearance, e.g. of our SiNWs. However, our simulations are 2D (to reduce solving times at the required fine meshing in structures as complicated as our SiNWs) whereas the SiNWs are 3D features and we truly underestimate the achievable field enhancement when using 2D instead of 3D simulations [40]. Therefore, we may consider our simulations as a lower limit of what is in principle achievable in terms of field enhancement.

Our SiNW geometry is given by 200 nm wide and 400 nm long SiNWs on a Si substrate with a Au-cap that is either truly hemispherical or slightly faceted. The active domain for the calculation is $2 \times 2 \mu\text{m}^2$. We tested the convergence of our models for different mesh sizes via the evaluation of the normalized electric field at the centre of the gold hemisphere and found the applied mesh to be sufficiently fine to not obtain mesh dependent results. We choose an adaptive meshing with a maximum grid size of 1 nm at all surfaces. So we ended up with a relatively coarse mesh within the silicon NW shaft of 50 nm but a very fine one in the sensitive surface regions of the Au-cap, thus realizing an optimum compromise between exactness and solving time. The incident electric field is assumed as an electromagnetic plane wave with in-plane polarization (TM mode). As a variable parameter we chose the wavelength of the incident laser light, varying from 220 nm to 900 nm in two nanometer steps.

The single crystallinity of the Au-caps is verified by electron back-scatter diffraction (EBSD) in an SEM (TESCAN, LYRA equipped with an AMETEK, TSL EBSD system).

§ 4-3 Results

We will show that we can enhance the PL signal of the QDs by Au nanoparticles (named caps throughout the paper) as they form on SiNWs that were grown by the VLS process. The enhancement constitutes an optical near field effect that will be described and

discussed in the following, supported by finite element modelling (FEM) using the COMSOL code.

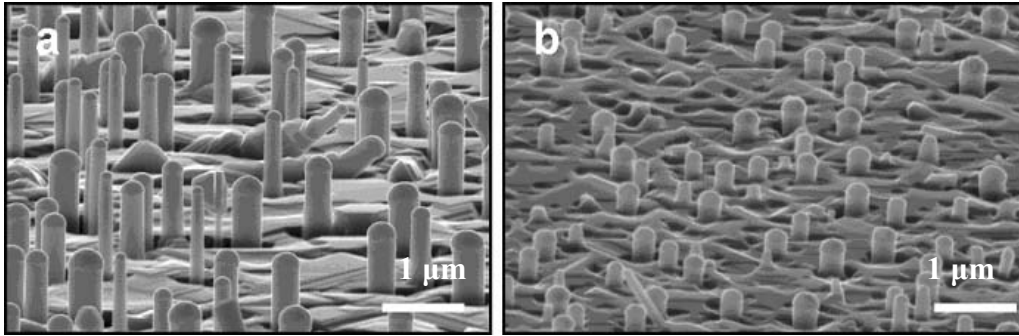


Fig. 4.1 SEM images of Si NWs grown by EBE at 650°C: (a) 1h; (b) 10min. Scale bar for (a) and (b) is 1 μm .

Typical SiNWs grown by EBE are shown in Fig. 4.1a (10 min growth) and 1b (1 h growth). The difference in the samples is the growth time of SiNWs. Statistical data of NW lengths and diameters are taken from SEM investigations. SiNW statistics gives the following lengths and diameter values: after 10 min the SiNWs are 350 \pm 50 nm long and 200 \pm 30 nm in diameter; after 1 h the SiNWs are 650 nm \pm 100 nm long and 325 nm \pm 80 nm in diameter. For 10 min growth the effect of surface migration of Au atoms over the surface is less pronounced [32-34]. That's why the NWs are of pretty identical length independently of the Au-cap diameter. After 1 h growth Ostwald ripening effects [32-35] are discernible (Fig. 4.1b) in the sense that bigger Au-caps grow bigger and smaller caps shrink further. In parallel, the smaller the cap the thinner the SiNW and thus the faster the growth since less material needs to be incorporated into the growing SiNW shaft. As a result, thinner SiNWs (e.g. <100 nm in diameter) grow faster and after 1 h growth time they are already substantially longer than thicker (e.g. >300 nm) ones (cf. Fig. 4.1b).

As concerns the size of the Au-caps we have a distribution of cap diameters in both samples, with a stronger scatter due to the Ostwald ripening after longer growth times. On average, however, the diameters lie for both the samples between \sim 200 nm and 300 nm.

The Au-caps assume in any case a close to half-spherical shape, often with some facets and are all single crystalline [36].

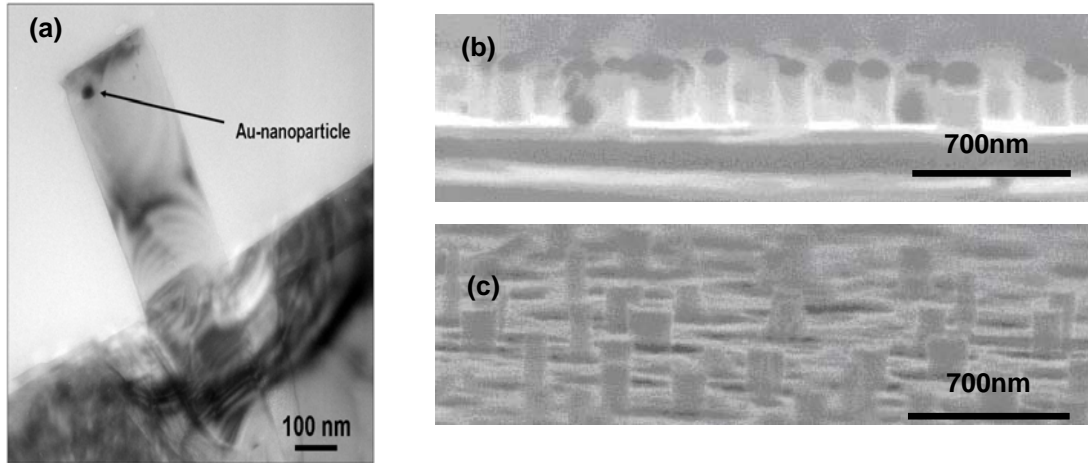


Fig. 4.2 (a) TEM cross sectional micrograph of a Si NW grown by EBE at 650 °C for 1 h from a Au-cap as the catalyst for the VLS growth. The Au on the SiNW surface agglomerated on the SiNW shaft by annealing the sample at 800°C for 20min in air. The Au-caps and agglomerates were removed by etching the sample in aqueous solution of KI/ I₂ (4:1) for 10 min after the surface SiO₂ that formed during oxidation had been removed by an HF dip (4 % HF in H₂O-dest, for 10 min). As a result the SiNW remained without the Au-cap atop and essentially a shaft that is free of Au agglomerates. On very rare occasions (we found this one example in an analyzed area of TEM samples of ~5 μm²) there remain Au agglomerates on the wire shaft that are not removed by the chemical treatment (indicated by an arrow here). These may consist of a Au-Si alloy that is resistant against the etch; **(b)** Cross sectional SEM of SiNWs from Fig. 4.1a; **(c)** Oblique SEM micrograph of SiNWs from (b) after chemical Au-cap removal.

For some samples, the Au-caps atop the Si NWs and on the SiNW shaft surfaces were removed by exposing them to aqua regia or aqueous solution of KI/I₂ (4:1) for 15 min (which both are known to be effective Au etchants) [37] after Au agglomeration on the surfaces by annealing at 800 °C for 20 min in air and subsequent oxide removal by an HF dip (hydrofluoric acid; 4% HF in H₂O-dest, for 10 min). An SEM analysis showed that the big Au-caps atop a NW and the smaller caps or Au clusters on the SiNW shaft surfaces were entirely removed after the treatment. In scanning electron microscopy we do not see any sign of remaining Au particles on the surface that give rise to strong scattering, so that

they are usually easily discernible in a secondary electron image as bright spots. In TEM studies we revealed that only on very rare occasions (one of these is selected for a TEM image in Fig. 4.2; Au particle indicated by an arrow) very small (few nanometers in diameter) Au agglomerates still remain. They are most probable composed of a Au-Si alloy so, that they are not as easily attacked by the gold-removing chemistry.

PL measurements were carried out for CdSeTe/ZnS QDs residing on a (i) bare Si(111) wafer, (ii) a Si(111) wafer with EBE SiNWs after 10 min and (iii) 1 h of growth and (iv) a Si(111) wafer with SiNWs after 1h of growth after Au removal in KI/I₂ etchant. For direct comparison PL measurements of the bare Si(111) wafer and the substrate wafer with SiNWs (1h of growth) without any QDs were carried out.

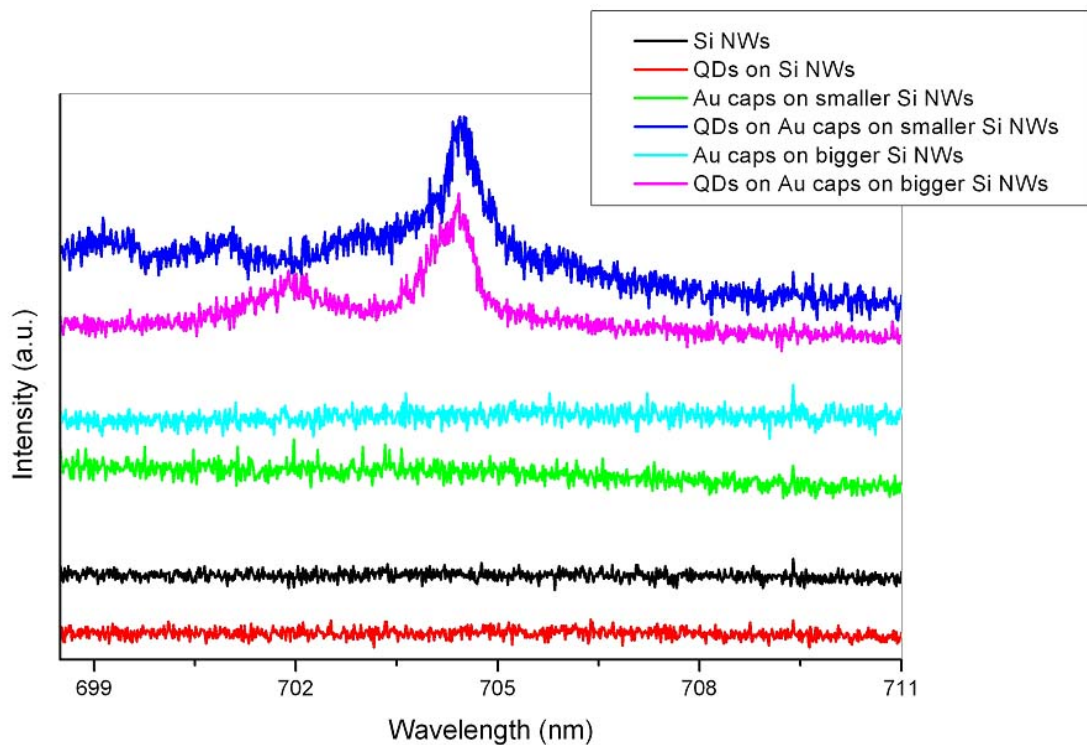


Fig. 4.3 PL study of core/shell CdSeTe/ZnS QDs on different substrates, including SiNWs with nanoscale Au-caps (blue and magenta lines). QDs are luminescent only when residing close to a Au-cap. QDs at the present dilution do not luminesce when residing on bare silicon surfaces (polished substrate surface or rough surface on the nanoscale due to SiNWs without the catalyzing Au-cap- red curve) nor do the bare surfaces luminesce without QDs (black, light blue, green curves).

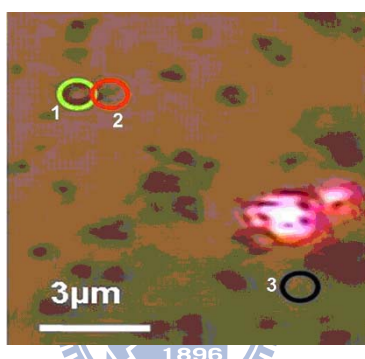
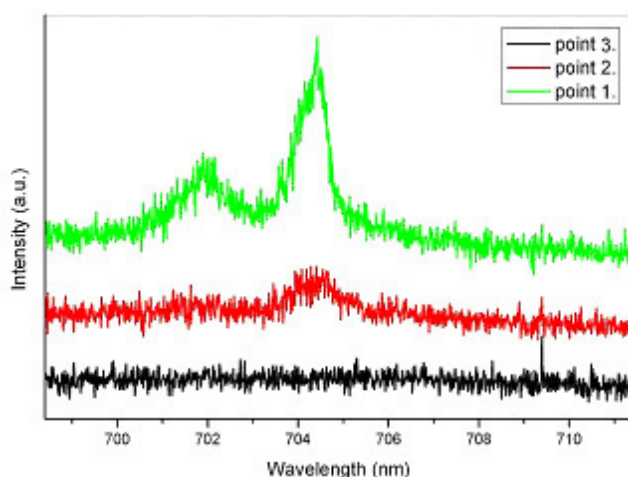


Fig. 4.4 Fluorescence PL measurements of core/shell CdSeTe/ZnS QDs on SiNWs with nanoscale Au-caps on Si(111) substrates as they form by the Au catalyzed VLS EBE growth. Single QD luminescence is discernible strong enough only when residing on a Au-cap (green line). Single QDs on the bare Si(111) surface do not give rise to a characteristic QD fluorescence PL signal (black line). The PL signal of ensembles of QDs may faintly appear if enough of them are close together as they are sometimes close to a SiNW (cf. Fig. 4.5, top row, right) (red line). The redish spot is due to reflected light of the focused laser on the sample surface.

All results of the PL study are shown in Fig. 4.3. No pronounced PL signal is visible for QDs on the substrate wafer alone (red line). No PL signal is visible for substrates without QDs, i.e. the bare substrate, neither for the bare substrate with SiNWs where the Au-caps have been removed (black line). However, an increased PL signal was found for all SiNWs (for both growth times) with Au-caps atop (green and turquoise line).

A pronounced PL signal with peaks at the QD emission range is only visible at this dilute concentration of QDs on the substrate surface when the QDs are in close vicinity to a

nanoscale Au-cap. PL signals of QDs on Au-caps are indicated by the blue and magenta lines. The characteristic fluorescence signal of the core/shell QDs is visible. The difference in the fluorescence signal of the QDs on the different SiNW samples can be interpreted as being a result of different size and composition of the QDs within the measured spot. Even though the QDs were purchased as a commercial product, the vendor does still allow a fluctuation in size and composition to a small extent that is however, may be enough to account for the PL signal differences. Another finding is that different PL signals were measured on different areas of the sample.

In Fig. 4.4 we see no PL signal of the QDs at an area where no SiNW was observed (black circle). We observe a pronounced PL signal (green line) that is very similar to the blue line signal in Fig. 4.3 when QDs reside directly on the Au-cap of SiNWs (1h of growth). We observe a faint PL which is however more than just background noise when measuring not exactly on the Au-cap but close to it on the substrate surface (Fig. 4.4, red line).

These findings can be interpreted based on an SEM study of the QD distribution after the spin coating procedure on the smaller SiNW sample surfaces. Using the high resolution SEM of a dual beam FIB (NOVALAB, FEI) with inlens detector it is possible to resolve the QDs on the sample surface as shown in Fig. 4.5.

We find that well separated QDs are spread over the sample surface and reside somewhere on the crystallographically faceted substrate surface or rarely on the Au-caps of the SiNWs too. In rare occasions even more than one QD resides on the Au-cap of a SiNW. It appears that the distribution of QDs is not exactly random. Close to the Au-caps with QDs usually the QD density on the sample surface is higher too. On the other hand there are areas that do not contain a QD whatsoever, neither on the NWs nor on the sample surface. This observation supports the PL results of Fig. 4.4 that suggest that single QDs on bare Si substrates do not give rise to the characteristic QD PL signal, that however, QDs at

higher density may give rise to a faint noisy QD PL and that even single QDs on Au-caps give rise to a more pronounced PL signal.

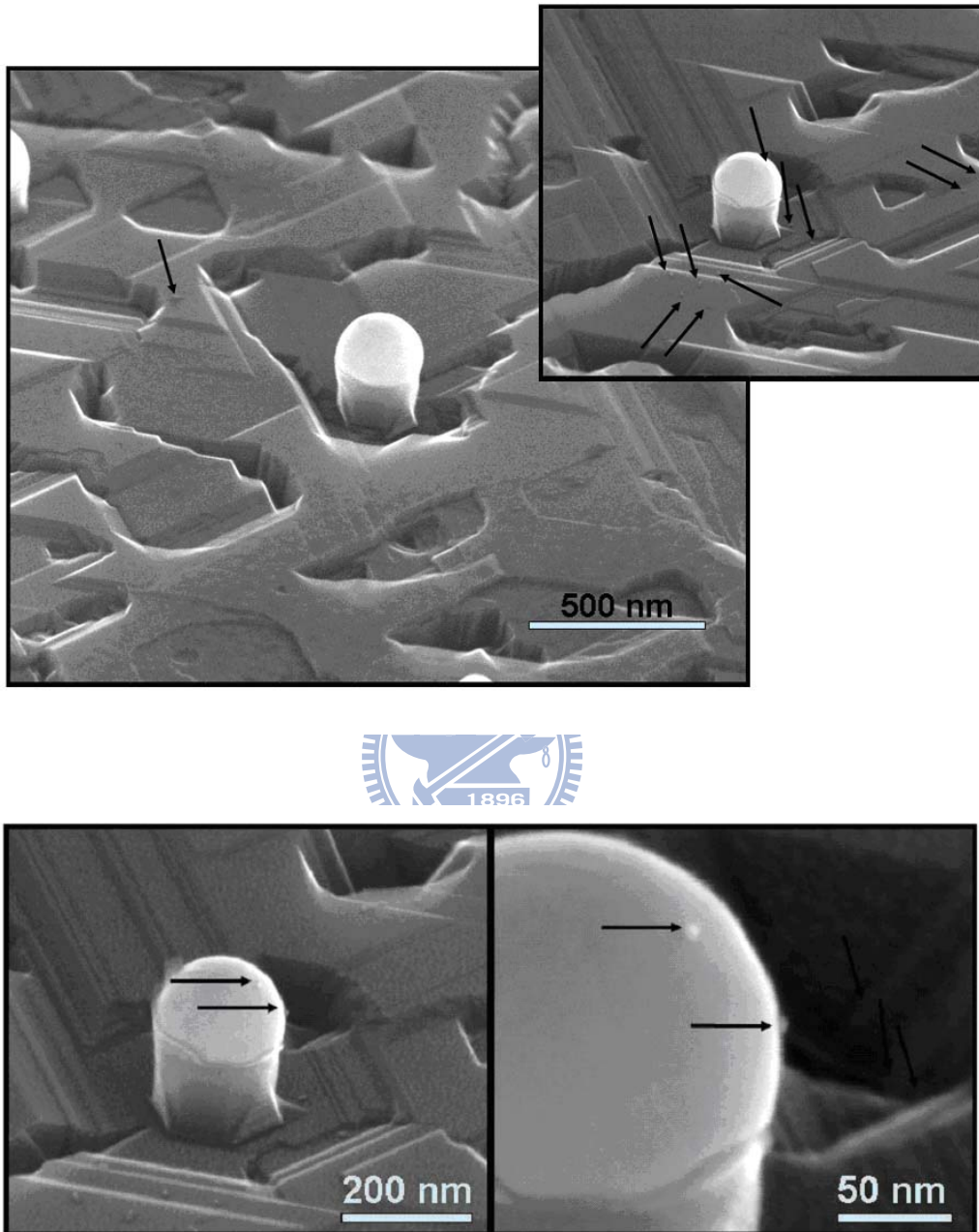


Fig. 4.5 High resolution SEM micrographs that show the $\sim 5\text{nm}$ core/shell CdSeTe/ZnS QDs on SiNWs with nanoscale Au-caps on Si(111) substrates as they form by the Au catalyzed VLS EBE growth. QDs in the top row of micrographs are on the left picture very rare and occur at higher density on the right picture which was taken at another spot on the sample. At areas where QDs reside on the Au-caps they are usually also found at higher density especially at the facets of the substrate surface. The bottom row of micrographs show a blow up of the QDs at the Au-cap surface. From these pictures the $\sim 5\text{nm}$ diameter of the QDs is clearly discernible.

§ 4-4 Discussion

The PL fluorescence signal enhancement by single crystalline Au-caps on VLS SiNWs can be interpreted in terms of enhancement effects that can reach several orders of magnitude depending strongly on the morphology and shape of the metal (here Au) nano features (here hemispherical, sometimes slightly faceted Au caps) as well as their crystalline nature. Single crystalline Au-caps are favorable for maximum, from lattice defects undisturbed enhancement. Fig. 4.6 gives a proof of the single crystallinity of the Au-caps. An EBSD pattern is shown that is superimposed on an SEM micrograph of a SiNW. The color code shows that the orientation of the Au-cap is not in registry with the SiNW [111]-direction. The orientation can be deduced from the color code. The fact that a single appears is a proof of single crystallinity. Larger statistics given by several EBSD patterns of different SiNW Au-caps show that the orientation of the caps differ but that all caps are single crystalline for the growth conditions used (for more details of this analysis cf. [46]).

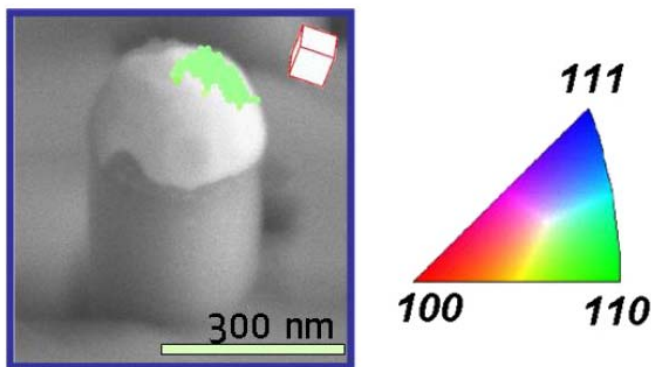


Fig. 4.6 *Electron backscatter diffraction pattern of a Au-cap on a SiNW. Due to the 3D geometry of the SiNW shadowing effects during EBSD analysis do allow to map only part of the Au-cap. However, this part that can be mapped is single crystalline as visible form the entirely, undisturbed green color. The same single crystallinity holds for all the Au-caps on VLS SiNWs that have been investigate (>8).*

The reason for the strong PL signal enhancement is still subject to some controversy [38, 39]. Two different mechanisms seem to be involved. The so-called pure electromagnetic effect is due to plasmon resonances of the metal nano-particles. The electromagnetic near field of a metal particle within this model can exceed the applied field by orders of magnitude. An additional enhancement can be caused by charge transfer or bond formation between the sample and the metallic substrate, which can strongly enhance the polarizability of e.g. a molecule. The electromagnetic near field enhancement of a metal nano-particle can affect the PL of our QDs. Typical near field enhancement factors as calculated by the FEM [31] can reach values of 3-5 strongly depending on the geometry of the metal nano-particle and the metal particle orientation with respect to the incident laser light. Let us again mention that our models are two-dimensional and therefore the estimated enhancement factors give a lower limit of the expected electro-magnetic enhancement. (This is due to the fact that spheres show stronger resonances than infinitely long cylinders which we had implicitly assumed.) Examples of the electromagnetic near field enhancement are given in the 2D FEM micrograph in Fig. 4.7, where the SiNW with Au-cap atop is shown as well as the polarization of the incident laser light for the example of incident laser light to be under 45° to the SiNW axis (polarization of laser light parallel to SiNW axis is denoted 0°). The SiNW in our example has a diameter of 200 nm and a length of 400 nm and the Au-cap is hemispherical (left) and (111) and (110) faceted (right). The color code indicates the dimensionless enhancement factor which is given by the absolute value of the local time averaged electric field normalized by the incident field.

The maximum enhancement achievable with 633 nm excitation wavelength and incidence of the polarized laser light under 45° with the type of Au-caps on VLS SiNWs we have is given by the hemispherical cap with an enhancement factor of 3.6 according to 2D FE simulations in Fig. 4.6 that leads to an intensity of 3.62. The fluorescence field at 704 nm (i.e. where the QDs have their resonances according to Fig. 4.3 and 4.4) shows a

factor of 3.3 (according to 2D FE simulations as shown in Fig. 4.8) which leads to an intensity of 3.3^2 . The overall maximum enhancement can thus be: $3.6^2 \cdot 3.3^2$, i.e. ~ 140 .

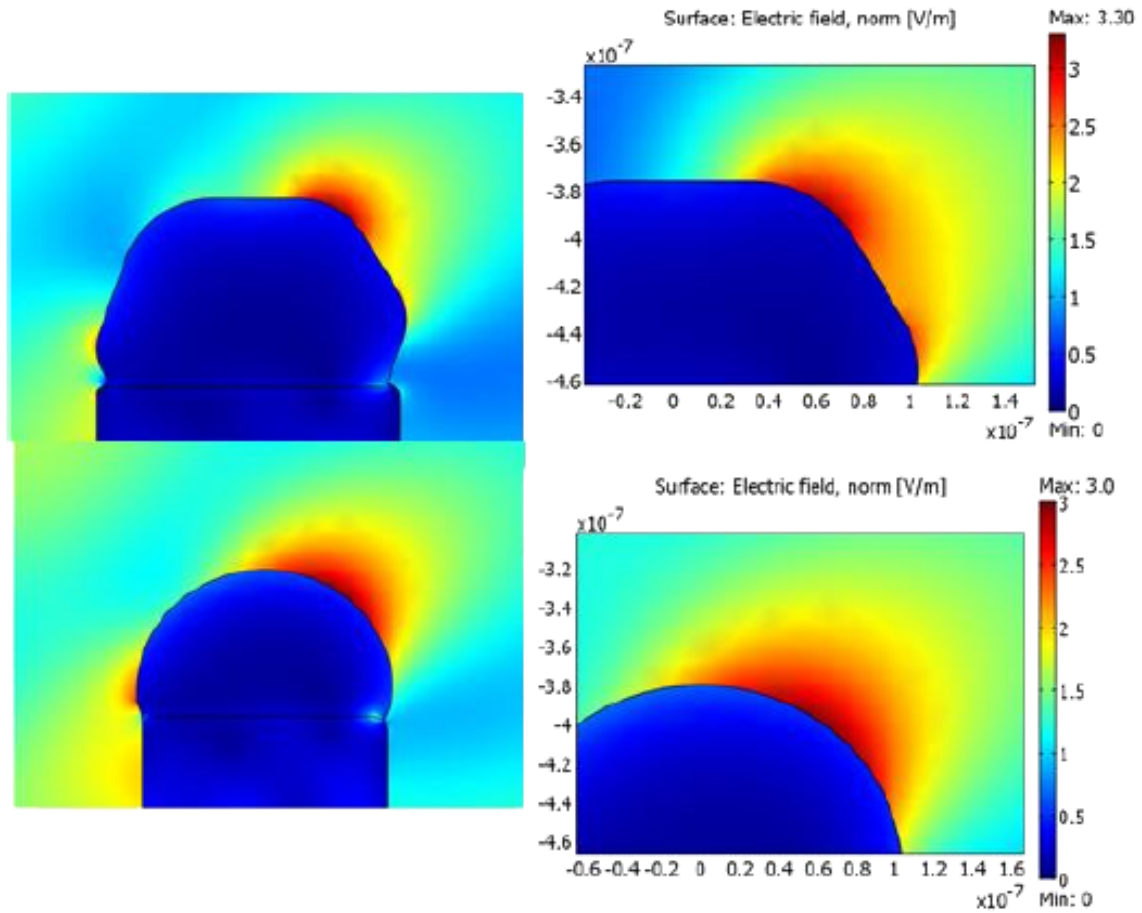


Fig. 4.7 Finite element modeling of the electromagnetic field enhancement at a SiNW with Au-cap atop. The color codes indicate the field enhancement factor as given by the local field divided by the incident field; light incident under 45° , 633 nm laser wavelength; (left) hemispherical cap, (right) (111) and (110) faceted cap.

The enhancement factor at the QD resonance of 704 nm can be deduced from 2D FE simulations in Fig. 4.8 where the enhancement factor depending on excitation wavelength is plotted for the geometrical point on the Au-cap surface of maximum enhancement. Fig. 4.8 shows a rather complex sequence of resonances depending on wavelength for the rather complex geometry of a slightly faceted or totally roundish Au-cap (both can experimentally be realized and controlled) sitting on pronounced SiNW shafts. The resonance at 704 nm coincides with an enhancement factor of 3.3.

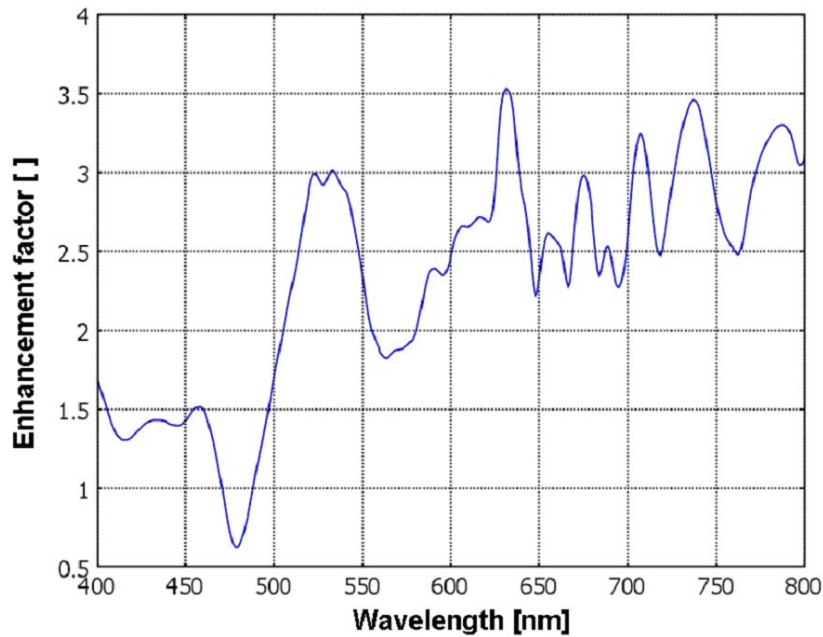


Fig. 4.8 Maximum enhancement factor deduced from 2D FE calculations as shown in Fig. 4.6 (for spherical Au-cap) as a function of wavelength of the incident laser light. Various resonances exist in the rather complex configuration of a SiNW with spherical Au-cap. One of these resonances resides at 704 nm with an enhancement factor of 3.3.

A definite interpretation of the mechanism of the PL enhancement requires further experiments. However, some points for discussion of PL enhancement can be given. First of all, the illumination was kept constant for all experiments, with and without Au-caps being present for the PL measurements of QDs. Therefore, the enhancement of PL intensity of QDs when Au-caps are present most probably follows the mechanism that was suggested before for dye molecules combined with silver nanoparticles by Kalele et al. [41]. This mechanism of increased PL in the vicinity of coinage metal nanoparticles is based on a higher excitation of the QD (higher absorption) there. The exciting light has a higher electric field strength close to the metal nanoparticles, here the Au-caps, and this then indirectly corresponds to a higher flux of photons and a higher probability of exciting the QDs. This in turn leads to a higher PL intensity. The opposite case, that PL quenching occurs in close vicinity to metal nanoparticles is not observed in our case and is therefore not discussed any further. Our observation, however, coincides with the earlier observation

that when metal nanoparticles are in close proximity to e.g. fluorophores, quenching of luminescence occurs, whereas when metal nanoparticles are located at a certain distance, enhancement in luminescence is observed. This effect has been explained by coupling of surface plasmon resonances from metal nanoparticles with the fluorophores, resulting in an increase of the excitation and emission rate of the fluorophore in the localized electromagnetic field [41,42]. The quenching and enhancement of luminescence intensity of the dye molecules was alternatively also explained as the transfer of electrons from the dye to the silver nanoparticles. Partly, it was also attributed to the aggregation of dye molecules upon addition of silver nanoparticles [41,42]. The aggregation of QDs at the Au-caps can be excluded in our case since the SEM pictures do not suggest such behavior.

For a proper discussion of observed PL fluorescence enhancement by Au-caps on SiNWs with respect to our 2D finite element calculations the following statistical considerations can be made: in principle, three cases can be distinguished for the QDs on silicon substrates with statistically distributed straight SiNWs with Au-caps atop, (1) single or (2) agglomerates of several QDs reside somewhere on one of the Au-cap or (3) QDs reside somewhere on silicon (wire or at different positions of the comparably rough Si substrate). For case (1) and (2) different options are possible: the laser beam can hit and excite the QD such that proper conditions for ideally maximum field enhancement are met, i.e. the PL experiment is carried out and polarization and direction of the laser beam creates an area of field enhancement on the Au-cap (cf. red spot on the Au-cap in Fig. 4.7) that coincides with the area where the QD is located or the PL experiment creates a spot of field enhancement but the QDs reside outside of this one on the Au-cap. In PL mapping experiments (we were mapping several tens of square micrometers) areas of effective PL can be distinguished as ‘hot spots’. Following our interpretation of the role of field enhancements for the PL signal of our QDs we can state that these ‘hot spots’ in the PL are spots where one or more QDs reside on a Au-cap at the right position of field enhancement.

In Fig. 4.3 and 4.4 we see PL intensity maps that were taken in ‘hot spot’ areas in PL mappings. Statistical considerations allow to state, that the PL signal of single or few QDs on our Si substrate with SiNWs with Au-caps looks like appearing random and unpredictable. This is essentially due to the fact that the SiNWs with Au-caps show a size and shape distribution and that the ‘hot spots’ of field enhancement do not spread over the entire Au-cap but are very local and therefore QDs can sit in ‘correct or odd’ positions for maximum PL enhancement. However, the principle of using Au-caps to facilitate PL of single QDs works well as long as enough QDs reside in positions that support PL enhancement. This is not only supported by the measurements in Fig. 4.3 and 4.4 but also by PL mappings (not shown) that show ‘hot spots’ of PL signals and additionally carried out spontaneous emission experiments of single QDs.

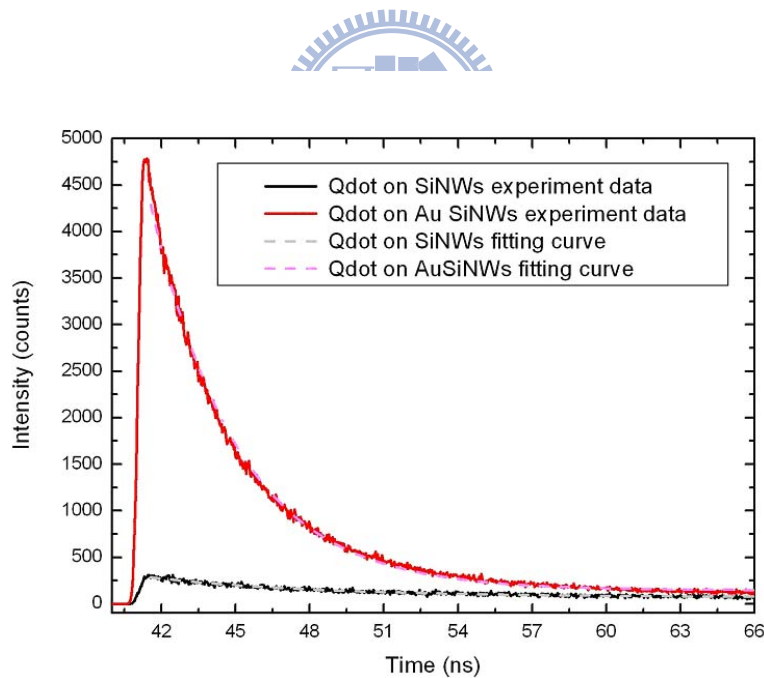


Fig. 4.9 Fluorescence signals analysis of single QDs on SiNWs with and without Au-cap. Time-Correlated Single Photon Counting (TCSPC) histogram is shown. By curve fitting QD lifetimes can be extracted from this measurement and by the ratio of lifetimes of the QDs on SiNWs with and without Au-cap we can deduce a 2.27- fold fluorescence enhancement due to the field enhancement by the Au-cap.

To further strengthen the concept to use Au-cap of SiNWs for local field enhancement that can be used to excite the fluorescence of QDs we carry out Time-Correlated Single Photon Counting (TCSPC) for single QDs sitting on SiNWs with and without Au-cap. The black line in Fig. 4.9 shows the accumulated PL intensity for a single QD on a SiNW without a Au-cap, while the red line shows the PL intensity of a single QD on a Au-cap that itself resides on a SiNW. The intensity accumulation was carried out for 60 seconds with a laser pulse exciting the QDs every 100 ns. After 60 s, there are 6×10^8 excitation cycles which produce $10^6 \sim 10^7$ photon counts. This number of counts is enough to obtain sufficiently large statistics. TCSPC histograms in Fig. 4.9 show accumulated photon counts for all cycles. According to the TCSPC histograms, the fluorescence intensities of the single QDs can nicely be fitted by an exponential decay: $I = A_0 + A_1 e^{-t/\tau_1}$, with τ_1 representing the lifetime of a QD, A_0 and A_1 representing the number of photons (given by counts) that were collected. The accumulated photon counts of all cycles for a single QD on the bare SiNW (cf. Fig. 4.2(c)) is shown in Fig. 4.9 (black curve) and the values deduced from this measurement are: $A_0 = 55.1(\text{counts})$, $A_1 = 148.2(\text{counts})$ and the lifetime of the QD is $\tau_1 = 9.78 \text{ ns}$. For the QD on the Au-capped SiNW (cf. Fig. 4.2(b)) the values, deduced from the TCSPC measurements are $A_0 = 106.4(\text{counts})$, $A_1 = 1779.4(\text{counts})$ and the lifetime of the QD is $\tau_1 = 4.30 \text{ ns}$. The quantum dot fluorescence enhancement by the Au-cap is characterized by the ratio of lifetimes τ_1 . This ratio is also known as a Purcell factor P [44, 45]. P is proportional to the ratio of spontaneous emission rates $P \equiv \Gamma_{total} / \Gamma_0$ while Γ_{total} represents the spontaneous emission rate with field enhancement while Γ_0 represents the spontaneous emission without enhancement, i.e. on the uncoupled single photon emitter. The spontaneous emission rates are inverse proportional to the QD lifetimes of the enhanced and uncoupled QDs and behave according to $P \equiv \Gamma_{total} / \Gamma_0 \equiv \tau_0 / \tau_{total}$. According to that we got a 2.27-fold

enhancement of the QD fluorescence by the Au-caps. The 2.27 fold enhancement is smaller than the 3.6 fold enhancement the calculations suggest. For the excitation wavelength of 400 nm a maximum enhancement of: $3.6^2 \times 1.6^2 \sim 33$ (the 1.6 is taken from Fig. 4.8) appears to be possible. The discrepancy in enhancement between experiment and simulation can as mentioned before be due to a non-optimal location of the QD with respect to the position of maximum field enhancement on the Au-cap. A larger number of experiments and better statistics of this type of TCSPC measurement are currently in preparation. These measurements will hopefully elucidate under which conditions the measured enhancement gets closer to the theoretical maximum value of 33 for the excitation wavelength in use.

§ 4-5 Conclusion



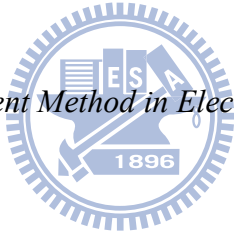
The preparation of the VLS silicon nanowires with Au-caps atop represents a new strategy for the realization of signal enhancing substrates based on plasmonic effects. These substrates have proved to be good candidates for ultrasensitive (due to signal enhancement mediated by the Au-nano-caps) detection of fluorescence photoluminescence (PL) signals of highly dilute core/shell CdSeTe/ZnS QDs in aqueous suspension. Given, that the SiNW based templates may not be the most effective ones for field enhancement due to the Au-cap shapes and sizes, they are, however, easily to be realized on wafer-level, cheaply and fast since VLS SiNW growth by chemical vapour deposition is a bottom up, self-organization technology that produces the single crystalline nano-sized Au-caps that are responsible for the field enhancement automatically during growth, without the necessity for any kind of nano-lithography. Most importantly, this approach is compatible with well-established silicon fabrication technology, making on-chip detection devices realizable.

References

- [1] Efros A.L. *Sov. Phys. Semicond.* **16**, 772 (1982)
- [2] Ekimov A.I., Onushchenko A.A. *Sov. Phys. Semicond.* **16**, 775 (1982)
- [3] Yoffe A.D. *Adv. Phys.* **50**, 1 (2001)
- [4] Alivisatos A.P. *J. Phys. Chem.* **100**, 13226 (1996)
- [5] Alivisatos A.P. *Science* **271**, 933 (1996)
- [6] Bruchez M. Jr., Moronne M., Gin P., Weiss S., Alivisatos A.P. *Science* **281**, 2013 (1998)
- [7] Chan W.C.W., Nie S. *Science* **281**, 2016 (1998)
- [8] Qu L.H., Peng X.G. *J. Am. Chem. Soc.* **124**, 2049 (2002)
- [9] Zhong X.H., Feng Y.Y., Knoll W., Han M.Y. *J. Am. Chem. Soc.* **125**, 13559 (2003)
- [10] Bailey R.E., Nie S.M. *J. Am. Chem. Soc.* **125**, 7100 (2003)
- [11] Kim S., Fisher B., Eisler H.J., Bawendi M. *J. Am. Chem. Soc.* **125**, 11466 (2003)
- [12] Wehrenberg B.L., Wang C.J., Guyot-Sionnest P. *J. Phys. Chem. B* **106**, 10634 (2002)
- [13] Rosenthal S.J. *Nat. Biotechnol.* **19**, 621 (2001)
- [14] Pollock C., *Fundamentals of Optoelectronics*, Irwin, Boston, MA (1995)
- [15] Wu X.Y., Liu H.J., Liu J.Q., Haley K.N., Treadway J.A., Larson J.P., Ge N.F., Peale F., Bruchez M.P. *Nat. Biotechnol.* **21**, 41 (2003)



- [16] Parak W.J., Gerion D., Zanchet D., Woerz A.S., Pellegrino T., Micheel C., Williams S.C., Seitz M., Bruehl R.E., Bryant Z., Bustamante C., Bertozzi C.R., Alivisatos A.P. *Chem. Mater.* **14**, 2113 (2002)
- [17] Pathak S., Choi S.K., Arnheim N., Thompson M.E. *J. Am. Chem. Soc.* **123**, 4103 (2001)
- [18] Auman E.R., Anderson G.P., Tran P.T., Mattoussi H., Charles P.T., Mauro J.M. *Anal. Chem.* **74**, 841 (2002)
- [19] Willard D.M., Carillo L.L., Jung J., Orden A. Van *Nano Lett.* **1**, 469 (2001)
- [20] Clapp A.R., Medintz I.L., Mauro J.M., Fisher B.R., Bawendi M.G., Mattoussi H. *J. Am. Chem. Soc.* **126**, 301 (2004)
- [21] Auman E.R., Clapp A.R., Anderson G.P., Uyeda H.T., Mauro J.M., Medintz I.L., Mattoussi H. *Anal. Chem.* **76**, 684 (2004)
- [22] Lingerfelt B.M., Mattoussi H., Auman E.R., Mauro J.M., Anderson G.P. *Anal. Chem.* **75**, 4043 (2003)
- [23] Tran P.T., Auman E.R., Anderson G.P., Mauro J.M., Mattoussi H. *phys. stat. sol. B* **229**, 427 (2002)
- [24] Willard D.M., Orden A. Van *Nat. Mater.* **2**, 575 (2003)
- [25] Wagner R.S., Ellis W.C. *Appl. Phys. Lett.* **4**, 89 (1964)
- [26] Givargizov E.I. *J. Cryst. Growth* **31**, 20 (1975)
- [27] (a) Sivakov V., Andrä G., Gösele U., Christiansen S. *phys. stat. sol. A* **203**, 3692 (2006)

- (b) Sivakov V., Andrä G., Himcinschi C., Gösele U., Zahn D.R.T., Christiansen S.
Appl. Phys. A **85**, 311 (2006)
- (c) Stelzner Th., Andrä G., Wendler E., Wesch W., Scholz R., Gösele U.,
Christiansen S.H. *Nanotechnology* **17**, 2895 (2006)
- (d) Christiansen S.H., Singh R., Scholz R., Gösele U., Stelzner Th., Andrä G.,
Wendler E. *J. Appl. Phys.* **100**, 084323 (2006)
- [28] Sivakov V., Heyroth F., Falk F., Andrä G., Christiansen S. *J. Cryst. Growth* **300**, 288
(2007)
- [29] Johnson P. and Christie R. *Phys. Rev. B* **6**, 4370 (1972)
- [30] <http://tools.invitrogen.com>
- [31] Jin Jianming, *The finite Element Method in Electromagnetics*, John Wiley & Sons Inc.
(2002)
- 
- [32] Ross F.M., Tersoff J., Reuter M.C. *Phys. Rev. Lett.* **95**, 146104 (2005)
- [33] Hannon J.B., Kodambaka S., Ross F.M., Tromp R.M. *Nature* **440**, 69 (2006)
- [34] Gösele U. *Nature* **440**, 34 (2006)
- [35] (a) Ostwald W. *Z. Phys. Chem.* **34**, 495 (1900)
- (b) Wagner C., *Z. Elektrochem.* **65** 581 (1961);
- (c) Lifschitz I.M., Slyozov V.V. *Phys. Chem. Solids* **19**, 35 (1981)
- [36] Christiansen S., Vogel A., Sivakov V., Bürki G., Michler J., *unpublished result*

- [37] Woodruff J. H., Ratchford J. B., Goldthorpe I. A., McIntyre P. C., Chidsey C. E. D. *Nano Letters* **7**, 1637 (2007)
- [38] Moskovits M. *Rev. Mod. Phys.* **57**, 783 (1985)
- [39] Otto A., Mrozek I., Grabhorn H., and Akemann W. *J. Phys.: Condens. Matter* **4**, 1143 (1992)
- [40] Ehrhold K., Becker M., Gösele U., Christiansen S., *unpublished result*
- [41] Kalele S., Deshpande A.C., Bhushan S., Kulkarni S.K. *Bull. Mater. Sci.* **31**, 541 (2008)
- [42] Zhang J., Lacowicz J.R., *J. Phys. Chem. B* **110**, 2387 (2006)
- [43] Chen Y., Munechika K., Plante Ilan Jen-La, Munro A. M., Skrabalak S. E., Xia Y., Gingera D. S. *Appl. Phys. Lett.* **93**, 053106 (2008)
- [44] Akimov A. V., Mukherjee A. et al. *Nature* **450**, 402 (2007)
- [45] Chang D.E., Sørensen A.S., Hemmer P.R., Lukin M.D. *Phys. Rev. Lett.* **97**, 053002 (2006)
- [46] Niederberger Ch., Christiansen S.H., Lerosé D., Sivakov V., Brönstrup G., Michler J., *unpublished result*

Chapter 5 Observation of the Localized Surface Plasmons in Spatially Controlled Array Structures

In this chapter, we observed nano-scale array structures of Au coated silicon nanorods (SiNRs) by illumination-mode near-field scanning optical microscopy (NSOM) and the Reflectance Spectrometer. By proper arrangements of the geometric configurations on the array structures, the properties of the localized surface plasmons (LSPs) resonance modes with different wavelengths can be manipulated and can be spatially observed by NSOM. The trends of reflectance spectra indicate that the localized surface plasmon modes can be spatially controlled by manipulating geometric parameters, the lattice constants of the array. In addition, the experimental results were compared with 2D numerical simulations based on finite element method (FEM). Satisfactory agreement between the experiment observations and numerical results were obtained.

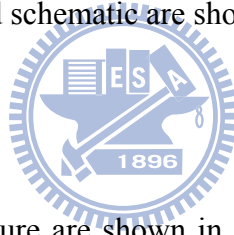
§ 5-1 Observed by Scanning Near-Field Optical Microscope

The localized surface plasmons on the array structure of Au coated SiNRs generated by excitation laser with different wavelengths were spatially observed by illumination-mode NSOM.

5-1-1 Introduction

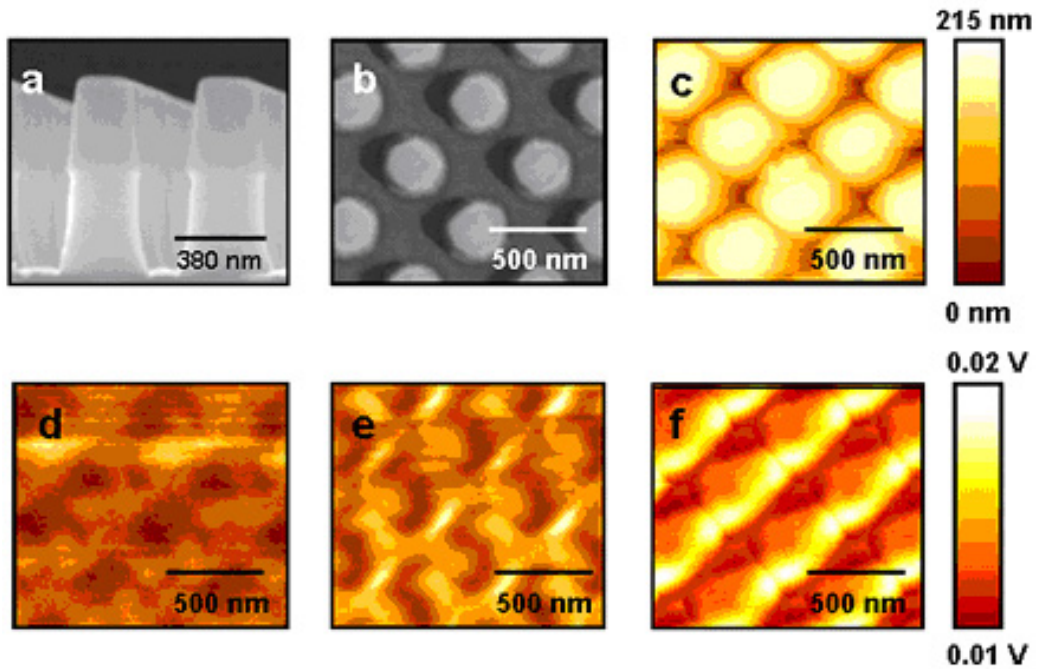
Surface plasmons (SPs) are waves that propagate along the interface of a metal and dielectric [1-7] material. Excitations of plasmons bounded in geometries such as bumps or voids are called LSPs [5, 8]. Recently, many relative applications such as surface enhanced Raman scattering (SERS) [7, 9], plasmon waveguides, filters, and nanocavities, etc. have been successfully developed. For further development of applications with higher efficiency, the spatial observation of the LSPs is necessary. In our study, the periodic SiNR array was fabricated by electron beam lithography (EBL). After SiNR arrays were constructed, a thickness of 50 nm gold thin films by electron gun were deposited on the surfaces. The LSPs modes were spatially resolved by using the illumination-mode NSOM. The NSOM instrument picture and schematic are shown in Fig. 2.6 in Chapter 2.

5-1-2 Results



SEM images of the array structure are shown in Fig. 5.1[a] for the side view and Fig. 5.1[b] for the top view. AFM image of the array structure is shown in Fig. 5.1[c]. Due to the diameter of the fiber tip is about 250 nm, the AFM image exhibits magnified diameter and shrunken height of Au coated SiNRs.

The AFM and NSOM images are simultaneously obtained. The excitation light is locally illuminated by a nano-aperture (~ 80 nm), and the near-field signals were collected by an objective at the 45° normal to the sample surface. The NSOM images of the three incident excitation wavelengths, 458 nm, 514 nm and 633 nm, are shown in Figs. 5.1[d-f]. We can find the LSPs exhibit specific characteristic of different incident wavelengths. The NSOM image implies the spatial distributions of LSPs modes. Due to the limitation of experimental configuration, the results of near-field scattering show the directional property and magnified edge effects.



Figs. 5.1 SEM images of the array structure: the side view [a], the top view [b]; the AFM image [c]; the NSOM image of incident wavelength: 458 nm [d], 514 nm [e], and 633 nm [f].



5-1-3 Conclusion

By proper arrangements of the geometric configurations on a metal/dielectric interface, the properties of the LSPs resonance modes with different wavelengths can be manipulated and then spatially observed by NSOM. The array structures were fabricated by well-established silicon technology and are reproducible. As exquisite design and fabrication are implemented, more efficient nanophotonic devices and circuits can be expected.

§ 5-2 Observed by Reflectance Spectrometer

We observed reflectance spectra of three different nano-scale array structures of Au coated SiNRs. The trends of reflectance spectra indicate that the localized surface plasmon modes can be spatially controlled by manipulating geometric parameters, the lattice constants of the array. In addition, the experimental results were compared with 2D numerical simulations based on finite element method. Satisfactory agreement between the experiment observations and numerical results were obtained.

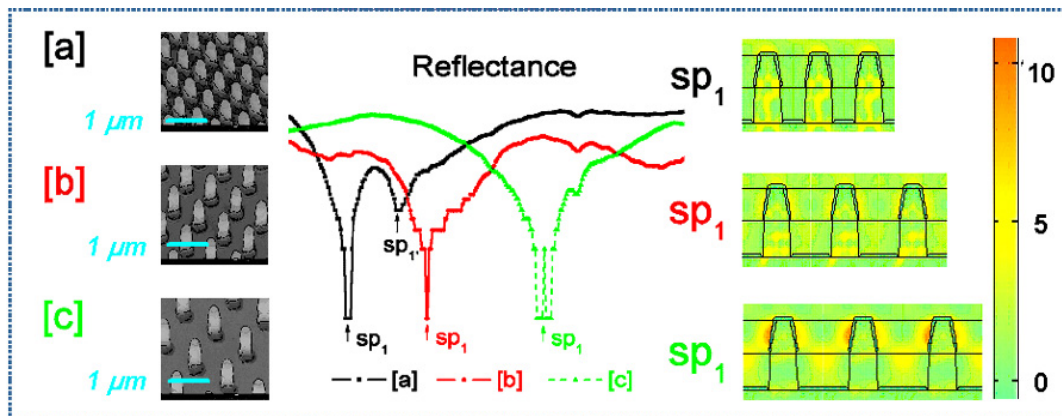


Fig. 5.2 *LSPs in Spatially Controlled Array Structures: SEM images, reflectance spectra and 2D FEM results*

5-2-1 Introduction

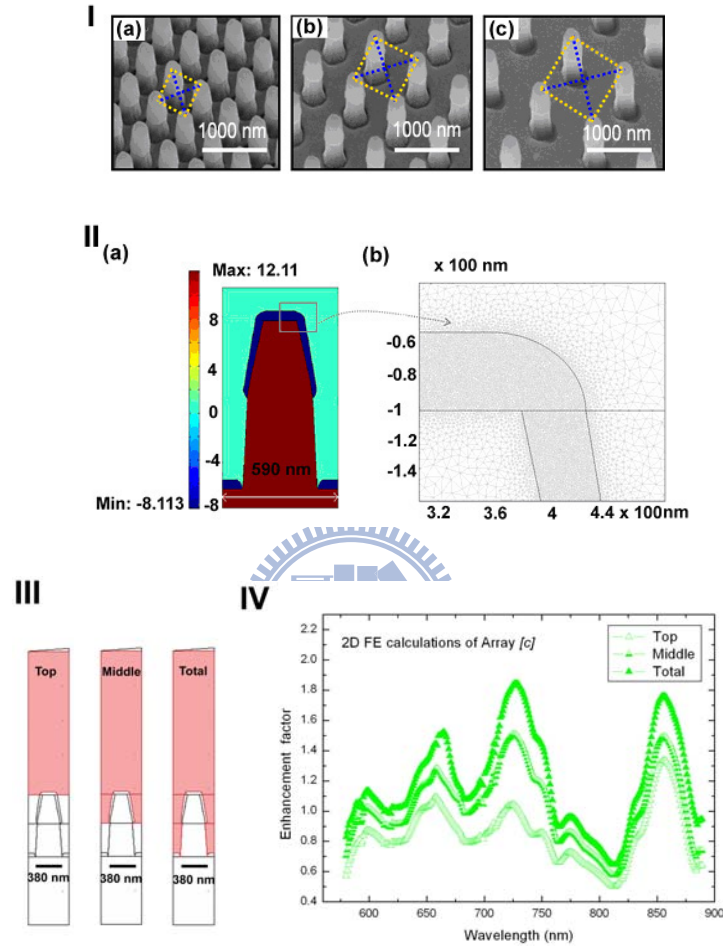
SPs are waves that propagate along the interface of a metal and dielectric[1-2] material. A combined excitation consisting of a surface plasmon (SP) and a photon is called a surface plasmon polariton (SPP) [3-7]. In addition to SP on a plane surface, excitations of electron plasmons bounded in geometries such as bumps or voids are called LSPs. Because

of the relatively higher loss and in-plane radiation of the SPP modes, the LSP modes dominate the enhancement effects. To distinguish the SPP and LSP modes, one can compare the field enhancement effects at locations near the metal surfaces with those far away from the metallic surfaces [8]. The field enhancement effects at the distance far from the metal surface due to the SPP modes tend to be much weaker than that caused by the LSP modes. By properly arranging the geometric configurations of a metal/dielectric interface, the properties of the SP modes, in particular, their interaction with light, can be manipulated. Therefore, many possible applications such as SERS [9-12], plasmon waveguides [13], filters, and nanocavities [14], etc. have been developed and improved in recent years. Experimental results from many different particle configurations vary widely in terms of the reported enhancement or quenching. In this letter, we designed three different array structures, i.e. square periodic arrays of gold-coated SiNRs, to investigate the LSP. The results show that the LSP modes can be manipulated. To study more of the modulated LSP modes, the FEM [15] which is commonly used for solving the partial differential equations over complicated domains is a good choice. Based on the electromagnetic theory, 2D FEM simulations were carried out to obtain the near-field optical properties, especially the field distribution of the array structures.

5-2-2 Experiment

In our experiments, the periodic SiNR arrays on Si (100) wafers (n-type, 27 Ω -cm) were fabricated by EBL and followed by Transformer Coupled Plasma (TCP) etching. After SiNR arrays were constructed, a thickness of 50 nm gold thin films by electron gun were deposited on the surfaces. Three samples of Au coated SiNRs of same diameters but with different shortest root distances (210 nm, 380 nm, and 650 nm) between the nearest neighbor Au coated SiNR arrays were prepared for the reflectance spectra measurements. Every single Au coated SiNR (in the three array structures) is not uniform cylinder. On the

top side, the SiNR is with Au coated (the diameter is ~ 200 nm); whereas on the root side, SiNR is without Au coated (the diameter is ~ 380 nm). And the length of the SiNR is ~ 900 nm.



Figs. 5.3I: SEM images of Au coated SiNR arrays (a-c) are shown. Scalar bars shown in (a-c) are $1 \mu\text{m}$. In the square unit cell of each array, both the peripheral distances ($D \sim 210$ nm, 380 nm, and 650 nm (yellow dash line)) and the diagonal distances ($\sqrt{2}D \sim 297$ nm, 537 nm, 919 nm (blue dash line)) between the two Au coated SiNRs were included in 2D FE calculations. In **Fig. 5.3II(a)**, a unit cell of array (a) is shown. The color code is the real value of the relative permittivity. ($\epsilon_{\text{Au}} \sim -8.1$, $\epsilon_{\text{Si}} \sim 12.1$, $\epsilon_{\text{Air}} \sim 1.0$) for incident wavelength: 600 nm [16]. **Fig. 5.3II(b)** is the mesh diagram. **Fig. 5.3III** The integration areas of top/middle/total region of each cell are shown. **Fig. 5.3IV** The enhancement factors calculated in the integration areas of top/middle/total region of array [c] are shown. The three enhancement factors' curves show the same features (without losing any SP resonance modes). Therefore, array [c] provides LSP resonance modes.

SEM images of the three array structures (Si substrate tilted with angle 30°) are shown in Figs. 5.3I(a-c). In Fig. 5.3II(a), a unit cell of 2D single Au coated SiNR of array (a) is shown. The color code is the real value of the relative permittivity ($\epsilon_{Au} \sim -8.1$, $\epsilon_{Si} \sim 12.1$, $\epsilon_{Air} \sim 1.0$) for incident wavelength equals to 600 nm [16]. In Fig. 5.3II(b), the mesh diagram is shown. And in Fig. 5.3III, the top/middle/total regions of the integration area used in the FEM simulation processes are shown. In Fig. 5.3IV, the enhancement factors calculated in the integration areas of top/middle/total region of array [c] are shown. The three enhancement factors' curves show the same features without losing any SP resonance modes. (Similar situations are also found in array [a] and [b].) Therefore, the SP resonance modes provided by our three samples are mainly LSP [8]. The enhancement factors corresponding to each specific wavelength are calculated from the integration area of the top region, as shown in Fig. 5.3III.

A standard reflection setup was used in the experiment. An un-polarized white light from a tungsten halogen lamp was focused on the sample. The spot size is smaller than the size of the sample but much bigger than the lattice constants of the arrays. Inside the region of the spot size (0.2 cm x 0.7 cm), thus, the light can illuminate every Au coated SiNRs uniformly. In reflectance spectra measurements, an incident angle of 5° from normal direction was set for the three different array structures. The reflection spectra from three arrays of Au coated SiNRs on Si substrates were normalized to that of 50 nm Au thin films without array structures on the same Si substrates.

5-2-3 Results

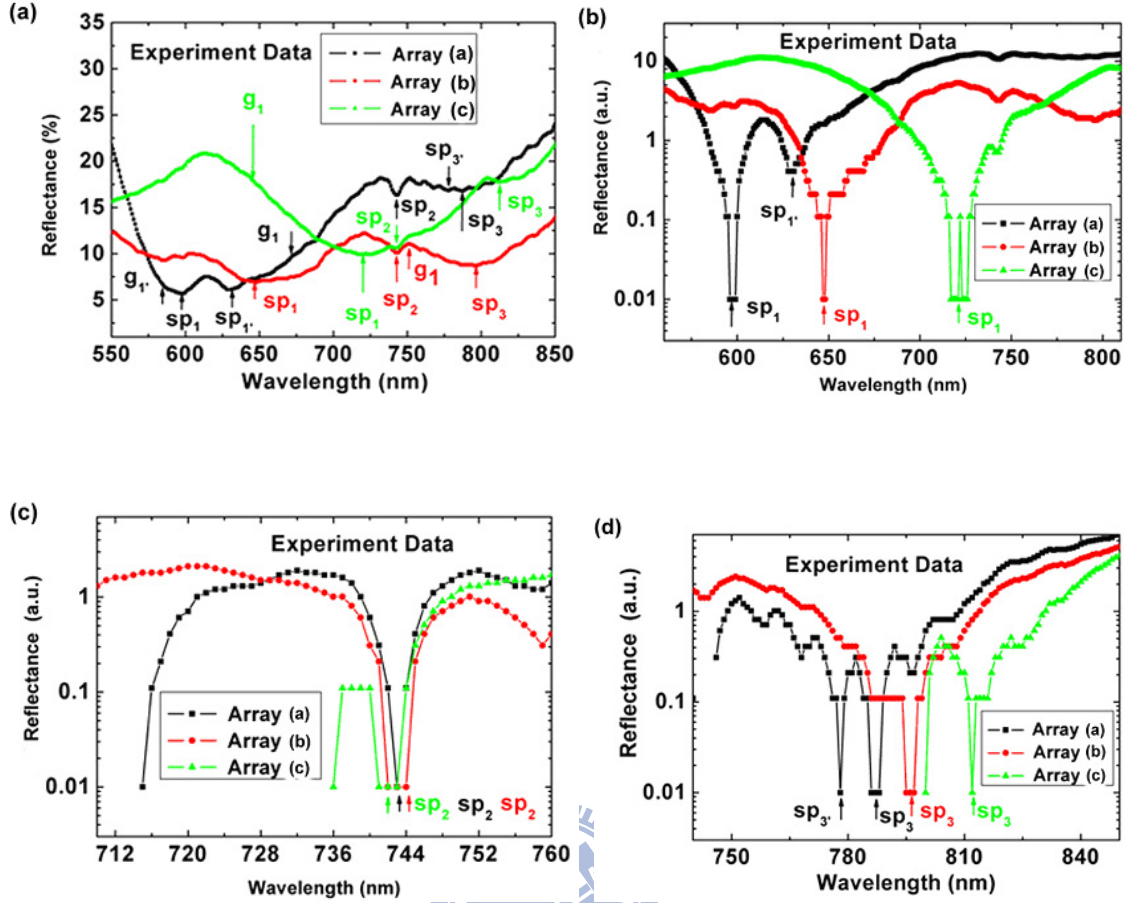
The reflectance spectra of three different array structures were observed and the results are shown in Figs. 5.4(a-d). Reflectance spectra labeled “Array (a)”, “Array (b)” and “Array (c)” shown in Figs. 5.4(a-d) correspond to the array structures as shown in the SEM images of Figs. 5.3I(a-c) respectively. As shown in Fig. 5.4(a), the original reflectance

spectra with the LSP resonances in each sample are within the wavelength region ranging from 550 nm to 850 nm. The LSP modes of the three arrays are labeled by arrows “sp_n” as shown in Figs. 5.4(a-d). Where sp₁, sp₁’ in Fig. 5.4(b) are the group for the highest frequencies; sp₂ in Fig.5.4(c) are the group for the other special feature, i.e. the notch is at an incident wavelength of 743 nm; and sp₃, sp₃’ in Fig. 5.4(d) are the group for the lowest frequencies. In order to compare the LSP modes of the three arrays more easily, we shifted the reflectance curves in Fig. 5.4(b-d) till their dips “sp_n” value reach at 0.01%, and then took the common logarithms of the three reflectance curves, respectively. As shown in Figs. 5.4(b-d), the longer the distances between Au coated SiNRs, the lower frequencies of the LSP modes (red shift), as shown in the reflectance spectra of Figs. 5.4(b)(d).

By a standard setup, we can only get information at which incident wavelength will the LSP resonate. For estimating the SP resonance frequencies, starting from Maxwell’s equations under appropriate boundary conditions, one can obtain the SP dispersion relation for the metal-dielectric interface:

$$k_{SP} = k_0 \sqrt{\frac{\varepsilon_m \varepsilon_d}{\varepsilon_m + \varepsilon_d}} \quad (5.1)$$

k_{SP} is the frequency-dependent SP wave-vector, ε_m is the frequency-dependent permittivity of the metal and ε_d is the frequency-dependent permittivity of the dielectric material. The SP wave-vector (k_{SP}) for a gold-air interface in our spectrum range 550 nm ~ 850 nm is $1.02k_0 \sim 1.07k_0$ [16, 17]. According to Eq. (5.1), the incident light with a lower frequency produces a higher frequency of LSP mode. This is because that $k_{sp} = 1.02k_0 \sim 1.07k_0$, $k_{sp} > k_0$, therefore, $\nu_{sp} > \nu_0$ ($k = \frac{2\pi\nu}{c}$, where ν is the frequency of light). The relative permittivity of the gold is assumed to follow the Drude model [17] and is frequency dependent, the experimental data of Johnson and Christie [16] were used in our 2D FEM simulations.



Figs. 5.4 Reflectance spectra of three arrays are shown. In **Fig. 5.4(a)**, original reflectance spectra of array (a-c) within wavelength 550 nm ~ 850nm are shown. The LSP modes (labeled by arrows “ sp_n ”) and the grating effects (labeled by arrows “ g_1 ”, “ g_1 ”) of array (a-c) are shown. **Figs. 5.4(b-d)** is the common logarithm of the reflectance curves. In **Figs. 5.4(b)** and **(d)**, the highest and the lowest frequencies of the LSP modes are shown in the spectra. In **Fig. 5.4(c)**, the LSPs resonance at $\lambda_0 \sim 743$ nm for array (a-c) (labeled by arrows “ sp_2 ”) are displayed, which show the unique feature of a single Au coated SiNR.

For a square array with the lattice constant a_0 and incident wavelengths λ_{ij} can be recognized approximately from the equation derived from the dispersion relation as shown in Eq. (5.1):

$$\lambda_{ij} = \lambda_{\max} \sqrt{i^2 + j^2} \cong a_0 \sqrt{\frac{\epsilon_m \epsilon_d}{\epsilon_m + \epsilon_d}} \quad (5.2)$$

Where indices i and j are the scattering orders from the array⁶. The red shift of the grating effects and the LSP modes of array [a-c] can be qualitatively explained by Eq. (5.2)

that when a_0 is tuned to be longer, the LSP modes λ_{ij} are shifted to be longer. However, due to the geometric complexities of our array structures, it's difficult to predict quantitatively the red shifts of LSP modes and the grating effects by simply using Eqs. (5.1) and (5.2). We shall employ the 2D FEM to estimate our observed results.

Table 5.1: *The peripheral distances and the diagonal distances ($D, \sqrt{2}D$), the incident wavelengths of the LSP modes ($sp_1, sp_1', sp_2, sp_3, sp_3'$) of Array (a-c) observed in the reflectance spectra, 2D FEM simulations results: the incident wavelengths at the extra sharp peak values of the time average total energy enhancement factors' curves for the grating effects (g_1, g_1') and the peak (or dip) values of the enhancement factors' curves for the LSP modes ($sp_1, sp_1', sp_2, sp_3, sp_3'$) of Array (a-c) are listed.*

Array	D, $\sqrt{2}D$ (nm)	Spectra:	FEM:	Spectra:	FEM:	Spectra:	FEM:	FEM:
		sp_1, sp_1' :	sp_1, sp_1' :	$sp_2: \lambda_0$	$sp_2: \lambda_0$	sp_3', sp_3' :	sp_3', sp_3' :	$g_1', g_1': \lambda_{ij}$
		λ_0 (nm)	λ_0 (nm)	(nm)	(nm)	λ_0 (nm)	λ_0 (nm)	(nm)
(a)	210, 297	597, 630	591, 624	743	743	778, 787	781, 786	584, 672
(b)	380, 537	650	660	743	743	797	791	751
(c)	650, 919	721	727	743	743	812	812	646

In Table 5.1, we list the peripheral and the diagonal distances of arrays (a-c) used in simulations, the incident wavelengths of the LSP modes ($sp_1, sp_1', sp_2, sp_3, sp_3'$) observed in the reflectance spectra, the extra sharp peak (g_1, g_1'), peak (or dip) ($sp_1, sp_1', sp_2, sp_3, sp_3'$) values of the time average total energy enhancement factors' curves (calculated by 2D FEM as shown in Figs. 5.6(a-c)). The characteristics of the grating effects are shown in the last column of Table 5.1 (The extra sharp peaks " g_n " at λ_{ij} calculated from the 2D FEM are listed, $\lambda_{10} = 584nm$ and $\lambda_{10} = 672nm$ are for the peripheral and diagonal direction of array (a) respectively, $\lambda_{10} = 751nm$ is for the peripheral direction of array (b), and

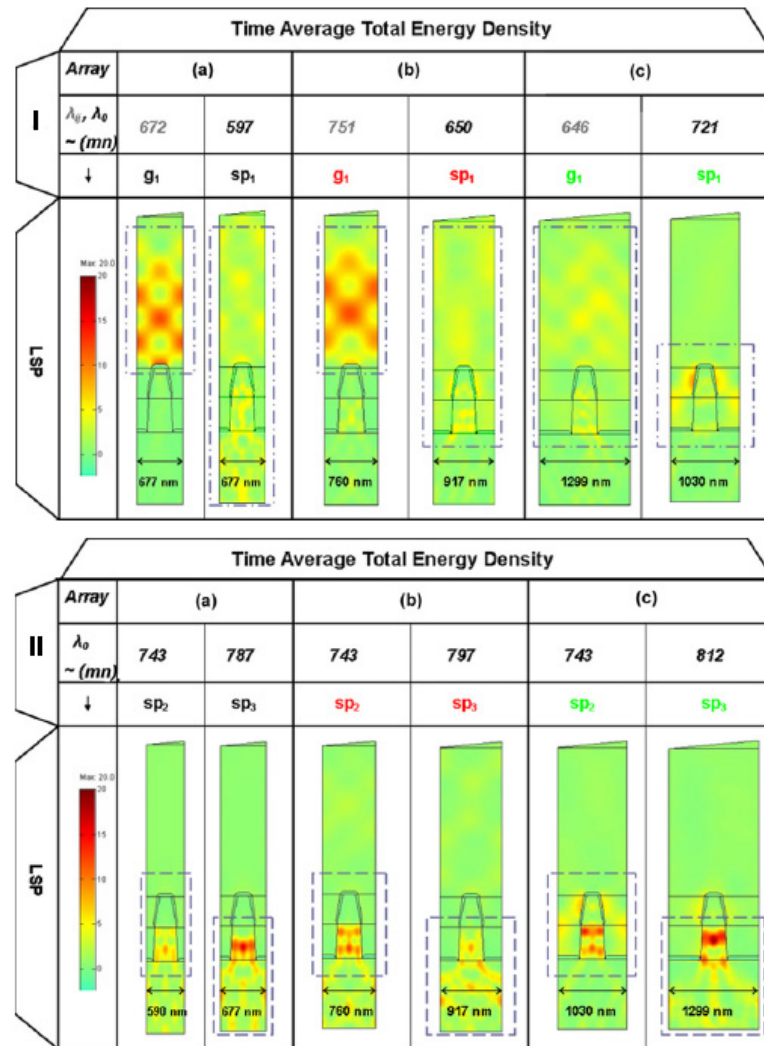
$\lambda_{21} = 646\text{nm}$ is for the diagonal direction of array (c) inside our interested wavelength region 560nm ~ 850 nm.) λ_{10} for the diagonal direction of array (c) is about 1300 nm which is clear for understanding the red shift characteristic of the grating effect. However, it is out of our interest wavelength region and is not listed here. Inside our interested wavelength region, only $\lambda_{21} = 646\text{nm}$ for array (c) is shown.

5-2-4 Discussion

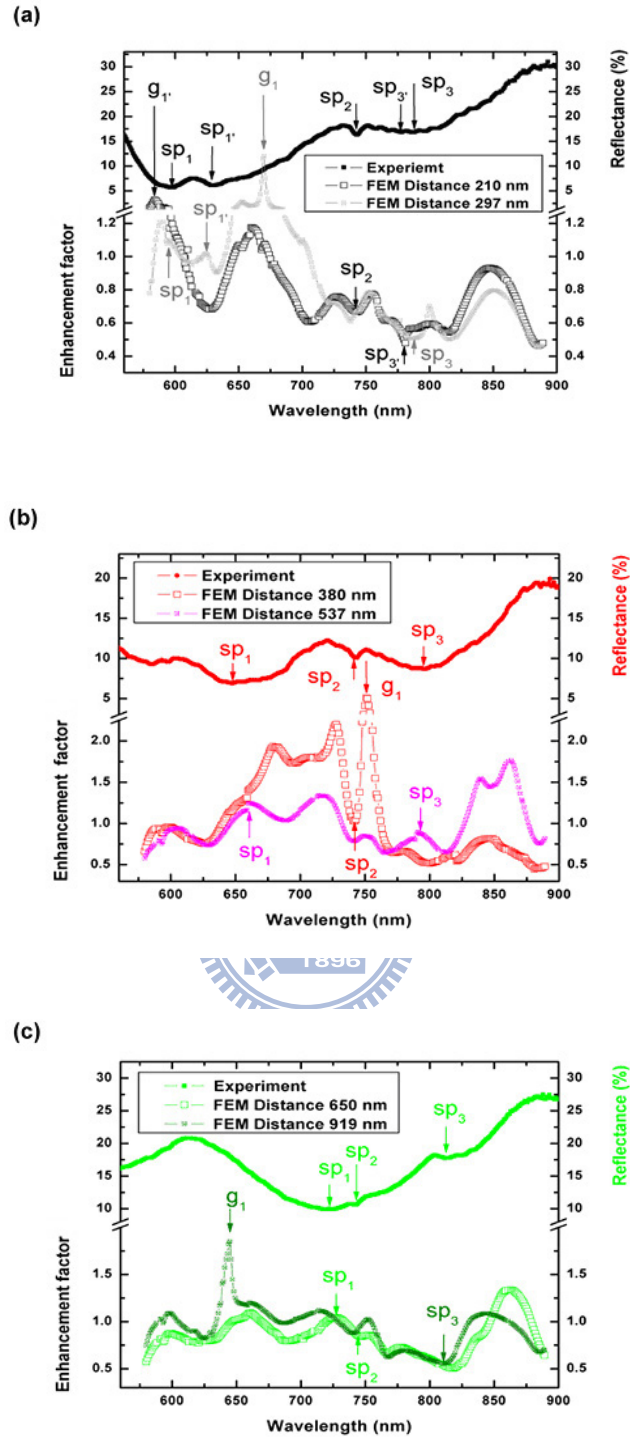
For analyzing the reflectance spectra of our specific array structures, we used the FEM simulations as implemented in the FEMLEB code (www.femlab.de) to calculate the time average total energy densities and the enhancement factors of arrays (a-c) at every specific incident wavelength. The results are shown in Figs. 5.3I-II and Figs. 5.6(a-c). In the simulations, the Helmholtz wave equations were solved within a unit cell by employing periodic boundary conditions for each case. In the square unit cell of each array, both the peripheral distances ($D=210\text{ nm}$, 380 nm , and 650 nm (as shown in Figs. 5.3I(a-c) yellow dash line)) and the diagonal distances ($\sqrt{2} D \sim 297\text{ nm}$, 537 nm , and 919 nm (as shown in Figs. 5.3I(a-c) blue dash line)) between the two Au coated SiNRs were included. The convergence of our simulation models has been checked by varying mesh sizes to evaluate the normalized electric field at the center of Au coated SiNR with a distance $\sim 5\text{ nm}$ away from the top of the rod. We reduced the mesh size until sufficiently fine so that the results do not depend on meshes, avoiding numerical errors [18]. Finally, we choose tiny meshes with a maximum grid size of 2 nm at all Au coating surfaces, and relatively coarse meshes of maximum value 50 nm within the SiNRs, as shown in Fig. 5.3II(b).

In Figs. 5.5I(a-c), the LSP modes accompanied with the constructive interference happened strongly in the air and slightly in the Si for array (a-c) are shown. And in Figs.

5.5II(a-c), the LSP modes accompanied with the constructive interference happened strongly in the Si and slightly in the air for array (a-c) are shown.



Figs. 5.5 2D FEM calculations of the normalized time average total energy densities of the three array structures which represent typical examples LSP modes with the grating effects. The left columns of **5.5I(a-c)** show the most obvious grating effects with strong constructive interference happened in the air at different λ_{ij} (labeled by arrow “ g_1 ”) for array (a-c). The right columns of **5.5I(a-c)** present the LSP modes with constructive interference happened stronger in the air (labeled “ sp_1 ”); while the right columns of **5.5II(a-c)** present the LSP modes with constructive interference happened stronger in the Si (labeled “ sp_3 ”). The left column of **5.5II(a-c)** show the LSP modes at $\lambda_0 \sim 743$ nm for array (a-c) (labeled by arrow “ sp_2 ”) is a unique feature from every single Au coated SiNR with constructive interference formed inside. The color codes for **5.5I-II** are the absolute values of the time average total energy densities which is normalized to the incident total energy densities.



Figs. 5.6 Reflectance spectra of array (a-c) with 2D FEM simulations of the normalized time average total energy enhancement factors are listed in **Figs. 5.6(a-c)**. In each unit cell, both the peripheral and diagonal Au coated SiNRs are included for calculations. The LSP resonance modes (shown as peaks or dips, labeled by arrows sp_n) and the grating effects (shown as the extra sharp peaks, labeled by arrows g_1 , g_1') found in 2D FEM simulation results are corresponding to reflectance spectra.

The theoretical counterparts of the typical LSP modes of the three array structures shown in reflectance spectra (Figs. 5.4(a-d)) can be found in Figs. 5.5I-II and Figs. 5.6(a-c) (marked with “sp_n”). Among these examples, the LSP modes indicate that the single Au coated SiNR exhibits its unique feature, i.e. the total energy densities are concentrated inside SiNRs and formed constructive interference inside SiNRs, as shown in Figs. 5.5II(a-c) (the left columns).

A quantitative interpretation of the reflectance spectra requires further investigations. However, some points for qualitative discussion of reflectance spectra can be given. First of all, the trends of the reflectance spectra can be modulated by varying the lattice constants of Au coated SiNR arrays. Second, the trends of reflectance spectra are dominated by the LSP modes and the grating effects. For the first point, we have discussed its detail with Figs. 5.4(a-d). For second point, the following discussions are given. The valleys shown in the reflectance spectra is corresponding to the high optical fields produced by the LSP modes and the conditions which are proper for the constructive interference formed inside the Si; whereas the peaks shown in the reflectance spectra is corresponding to the grating effects which form constructive interference in the air. Due to the optical fields highly confined at the surface of a metal and the propagations of the SP subjected to the significant energy losses. When the frequencies of the incident light are properly matched with those of the LSP resonance modes, the damping effects in the nonconductors are obvious and the corresponding absorption coefficients are increased to reach maximum values. Therefore, low reflection can be observed. In our Au coated SiNR array structures, the LSPs resonate at the surface of Au in the nonconductors, i.e. air and Si can both cause low reflectance. And as mentioned before, in addition to the LSP modes, the grating effects with the constructive interference formed in the nonconductors, i.e. air and Si can also contribute to the reflectance spectra. The complexity for analyzing is risen for the LSP modes are accompanied with the grating effects which may cause high

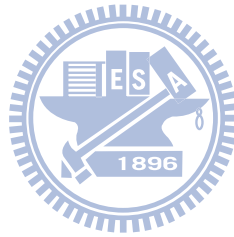
reflectance (with the constructive interference formed in the air) or low reflectance (with the constructive interference formed in the Si).

By 2D FEM, we find that the distributions of the time average total energy densities are strongly dependent on the geometries of the metallic nano-particles and their orientations with respect to the incident fields. And apparently, the LSP modes observed in reflectance spectra as shown in Figs. 5.4(a-d) manifest the characteristics that the total energies densities are highly concentrated near the surface of a metal as shown in Figs. 5.5I-II. We also obtain the normalized time average total energy enhancement factors in our spectrum range by integrating the time average total energy in the area on top region above the SiNR (height $\sim 2 \mu\text{m}$ in the air) of each unit cell for our three array structures with respect to 50 nm Au thin film without any array structures on the Si substrate (the results are show in Figs. 5.6(a-c) and Table 5. 1). One can find out that the sharpest peak values of the enhancement factors correspond to the obvious grating effects as shown in Figs. 5.5I(a-c) (the left column). And the LSP modes appear as the peaks (or dips) in the enhancement factors' curves as shown in Figs. 5.6(a-c). The LSP modes appear as the peaks in the enhancement factors when the LSP modes accompanied with the constructive interference formed strongly in the air as shown in Figs. 5.5I(a-c), and appear as the dips when accompanied with the constructive interference formed strongly in the Si as shown in Figs. 5.5II(a-c). For all simulations, the incident TM mode plan wave is 5° inclined to the normal direction of the Si substrate. And the color codes in Figs. 5.5I-II indicate the absolute value of the time average total energy density which is normalized by the incident total energy density.

The reason that the sharp peaks “ g_n ” obtained by the simulations are missing in the observed spectra can be explained as follows. The simulation result of each array is full angle integration: $0^\circ \sim 180^\circ$ which obtained from linear superposition of the TM mode plane wave in the near field regions. It can reveal subtle characteristic of the intensity

distributions including the grating effects from higher order diffractions and also more LSP modes. However, in the experimental observations, the far field reflection measurements of 5° reflection angle were performed, one can receive only the zero order diffraction. This is the case in the grating equation: $a_0(\sin \theta_m - \sin \theta_i) = m\lambda$, a_0 is the lattice constant, θ_m is the diffraction angle, and θ_i is the incident angle. In this case, $\theta_m = \theta_i = 5^\circ$, so that $m = 0$, the zero order diffraction light is the reflection light itself. At the reflection angles with 5° in the far field regions, the higher order diffraction cannot contribute to the rise of the intensity. Therefore, at the reflection angle, the grating effects (sharp peaks “g_n”) were not observed in reflectance spectra. Owing to this arrangement in experiments which could avoid the disturbance of the sharp diffraction peak, the LSP peaks could be clearly extracted from the reflection spectra.

5-2-5 Conclusion



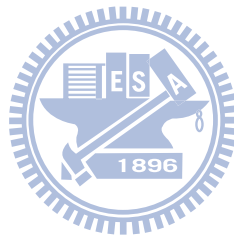
Based on the electromagnetic theories, the time average total energy density of the three Au coated SiNR array structures were calculated by 2D FEM. There are two important constituents: the LSP modes and the grating effects should be considered for understanding their corresponding reflectance spectra. The coupling of LSP with light can cause emission enhancing or quenching at different incident wavelength conditions in different locations of our structures. During the coupling processes, the incident light energies are transferred into the LSP modes. If the SP modes match with radiation modes, light emission can be efficiently enhanced. In contrast, SP dissipation leads to emission quenching. A grating structure is a good choice for controlling phase matching between LSP modes and radiation modes. The array structures we studied were fabricated by well-established silicon technology and are reproducible. Although the LSP resonance modes are sensitive

to the geometries of metal/dielectric interfaces, it is still a challenge to precisely implement a particular geometry and achieve the emission enhancement/quenching of a desired emission wavelength based on the LSP coupling. As exquisite design and fabrication are implemented, more efficient optical devices and newly development circuits can be expected.

References

- [1] Ritchie R. H. *Phys. Rev.* **106**, 874 (1957)
- [2] Stern E. A. and Ferrell R. A. *Phys. Rev.* **120**, 130 (1960)
- [3] Zayats Anataly V and Smolyaninov Igor I. *J. Opt. A: Pure Appl. Opt.* **5**, S16 (2003)
- [4] Pitarke J. M., Silkin V. M., Chulkov E. V. and Echenique P. M. *Rep. Prog. Phys.* **70**, 1–87 (2007)
- [5] Song Jung-Hoon, Atay Tolga, Shi Sufei, Urabe Hayato, and Nurmikko Arto V., *Nano Lett.* **5**, 1557 (2005)
- [6] Barnes William L., Dereux Alain, and Ebbesen Thomas W. *Nature* **424**, 824 (2003)
- [7] Kneipp Kartrin, Moskovits Martin, and Kneipp Harald: *Surface-Enhanced Raman Scattering*, Springer (2006)
- [8] Chuang Wen-Hung, Wang Jyh-Yang, Yang C. C. and Kiang Yean-Woei *Appl. Phys. Lett.* **92**, 133115 (2008)
- [9] Félidj N., Aubard J., Lévi G. *Phys. Rev. B* **65**, 075419 (2002)
- [10] Ibach Harald and Lüth Han, *Solid-State Physics —An Introduction to Principles of Materials Science*, Second Edition, Springer (2002)
- [11] Christiansen S. H., Becker M., Fahlbusch S., Michler J., Sivakov V., Andrae G., and Geiger R. *Nanotechnology* **18**, 035503 (2007)

- [12] Becker M., Sivakov V., Goesele U., Stelzner T., Andra G., Reich H. J., Hoffmann S., Michler J., and Christiansen S. H. *Small* **4**, 398 (2008)
- [13] Maier Stefan A., Kik Pieter G., Atwater Harry A., Meltzer Sheffer, Harel Elad, Koel Bruce E., and Requicha Aria G. *Nature Material* **2**, 229 (2003)
- [14] Bozhevolnyi S. I., Smolyaninov I.I., and Zayats A. V. *Phys. Rev. B* **51**, 17916 (1995)
- [15] Jin Jianming, *The Finite Element Method in Electromagnetics*, Second Edition, JOHN WILEY & SONS. INC (2002)
- [16] Johnson P. B. and Christy R. W. *Phys. Rev. B* **6**, 4370 (1972)
- [17] Frederick Wooten, *Optical Properties of Solids*, Academic, New York (1972)
- [18] Christiansen S. H., Chou J. W., Becker M., Sivakov V., Ehrhold K., Berger A., Chou W. C., Chuu D. S., Gösele U. *Nanotechnology* **20**, 165301 (2009)



Chapter 6 Fluorescence Signals of Quantum Dots

Influenced by Spatially Controlled Array

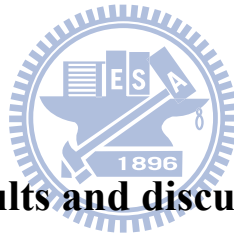
Structures

Fluorescence signals of quantum dots (QDs) influenced by different array structures of the gold-coated silicon nanorods (SiNRs) were investigated via experiment observations and 2D finite element method simulations. On the densest gold-coated SiNR array structure, the highest QDs fluorescence quenching rates were observed. And on the sparsest array structure, the highest QDs fluorescence enhancement rates were observed. By developing a new technique which obtains the optical image of the array structures without losing information of the QD locations, we are able to further investigate how the QDs fluorescence influenced by spatially controlled array structures.

§ 6-1 Introduction

The fluorescence emission from semiconductor nanoparticles can be significantly influenced by coupling with the localized surface plasmon (LSP) provided by metal surfaces [1-3]. By properly arranging the geometric configurations of a metal/dielectric interface, the properties of the LSP resonance modes, in particular, their interaction with light can be manipulated. For example, the topic of QDs located within the range of surface plasmon polariton [4-12] has been studied. Besides, many applications such as

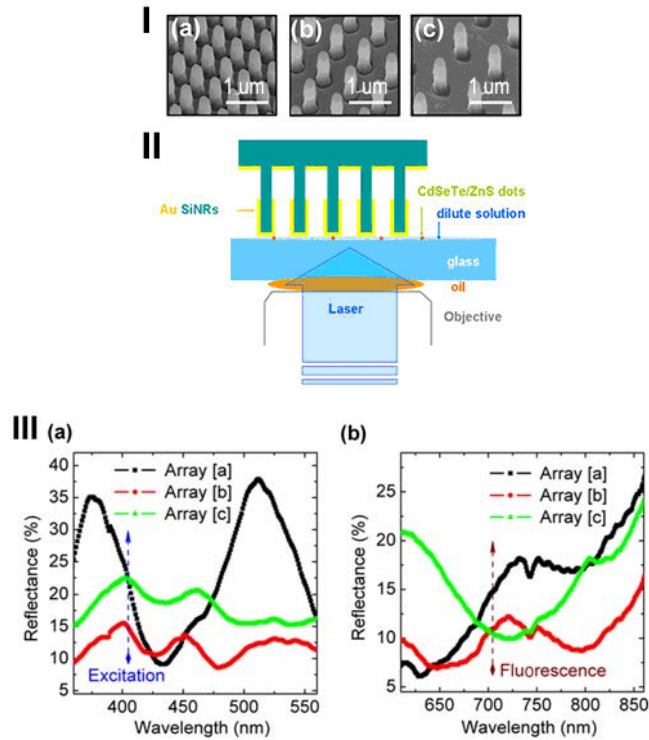
surface enhanced Raman scattering (SERS) [13-16], plasmon waveguides [17], filters and nanocavities [18], etc. are developed recently. In this letter, for investigating the coupling effects of the QDs fluorescence and the LSP resonance modes, we designed three different array structures, i.e. square periodic arrays of gold-coated SiNRs for the experiments. The geometric size and shape of the Au coated SiNRs in these three array structures are fixed, however, the distances between the Au coated SiNRs are varied for spatial controlling the LSP resonance modes. Both enhancement and quenching of the QDs fluorescence influenced by the array structures were observed in the experiments. We further developed a new technique to define the relative locations between the QDs and the Au coated SiNRs for observing how the relative locations influence the coupling effect. Finally, 2D finite element (FE) [19] simulations based on electromagnetic theory were applied for interpretations.



§ 6-2 Experiments results and discussions

In our experiments, the periodic SiNR arrays on Si (100) wafers (n-type, 27 Ω -cm) were fabricated by electron beam lithography (EBL) and followed by Transformer Coupled Plasma (TCP) etching which is able to provide capability to etch nanoscale features into silicon and metal films. After SiNR arrays were constructed, a thickness of 50 nm gold thin films by electron gun was deposited on the surfaces. Three samples of Au coated SiNRs of same diameters but with different shortest root distances (210 nm, 380 nm, and 650 nm) between the nearest neighbor Au coated SiNR arrays were prepared for the measurements. The diameter of Au coating on top of SiNRs is \sim 200 nm, the root diameter of SiNRs is \sim 380 nm, and the length of SiNRs is \sim 900 nm. SEM images of the three array structures (Si substrate tilted with angle 30°) are shown in Figs. 6.11(a-c). The commercially available core/shell (CdSeTe/ZnS) QDs [21] (diameter 5.3 nm, concentration $\sim 10^{-9}$ M) were

spin-coated (~ 5000 rpm) on a cover glass. And then, each array structure was put upside down above the cover glass (the top of the Au coated SiNRs was contacted with the QDs on the cover glass) as shown in Fig. 6.1II.



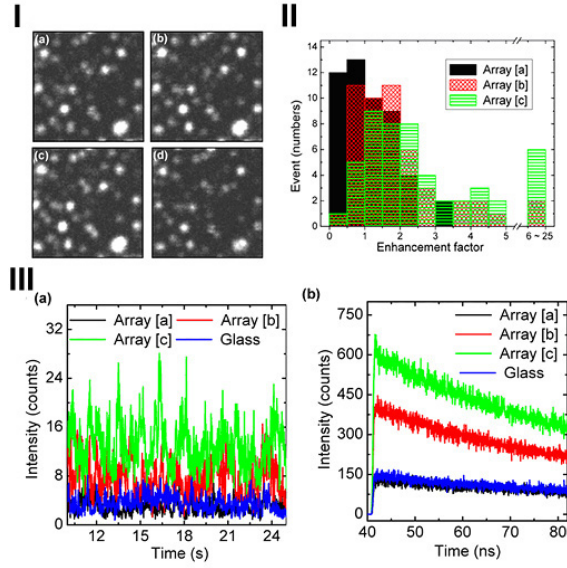
Figs. 6.1I(a-c) SEM images of Au coated SiNR arrays [a-c]. Scalar bars shown in (a-c) are $1 \mu\text{m}$. **II** Schematic view of the sample structure. **III (a)** and **(b)** show the reflectance spectra of arrays [a-c] (without QDs) near the excitation (405 nm) and near the QDs fluorescence center (705 nm) wavelength range, respectively. The wavelength of the QDs center fluorescence (705 nm) is relatively close to the LSP resonance modes (shown as valleys) of array [c].

The reflectance spectra of three different array structures were observed and the results are shown in Fig. 6.1III(a) for wavelength range $360 \sim 560 \text{ nm}$ (covered the excitation laser wavelength 405 nm), and in Fig. 6.1III(b) for wavelength range $610 \sim 860 \text{ nm}$ (covered the single quantum dot (SQD)) fluorescence center wavelength 705 nm). In reflectance spectra measurements, an incident angle of 5° from normal direction was set for the three different array structures. Reflectance spectra labeled “Array [a]”, “Array [b]” and “Array [c]” shown in Fig. 6.1III (a) and (b) correspond to the array structures shown in the SEM images of Figs. 6.1I(a-c) respectively. The un-polarized white light from a

tungsten halogen lamp was focused on the sample. The reflection spectra from three arrays of Au coated SiNRs on Si substrates were normalized to that of 50 nm Au thin films without array structures on the same Si substrates.

The LSP modes can be tuned by varying the distances between Au coated SiNRs. The valleys shown in the reflectance spectra corresponding to the high optical fields are produced by the LSP modes [20]. In Fig. 6.1III(a), the excitation wavelength 405 nm is not close to the LSP mode (shown as valleys) of arrays [a-c]; whereas in Fig. 6.1III (b), the LSP mode of array [c] is close to the fluorescence wavelength 705 nm. These results indicate that the excitation laser source can hardly couple to the LSP modes of the three arrays. And among the three array structures, array [c] provides higher coupling efficiency for QDs fluorescence enhancement [10]. In other words, the excitation laser source cannot be enhanced on arrays [a-c]. However, QDs fluorescence on array [c] can be efficiently enhanced.

QDs fluorescence signals were measured by PicoQuant Microtime200 confocal microscope system (with the objective: Olympus UPlanSApo 100xoil, NA = 1.4). The picosecond pulsed diode laser (repetition frequency: 10 MHz, wavelength 405 nm, power $\sim 0.02 \mu W$) was used as the excitation source for obtaining sufficient statistical lifetime histograms, and a long pass 500 nm filter was used to filter out the excitation laser. The fluorescence images (areas: $4.75 \times 4.75 \mu m^2$) of represented 50 different QDs on arrays [a-c] and on the glass are shown respectively in Figs. 6.2I (a-d). In Fig. 6.2II, total event numbers distribution statistics of enhancement factors from 50 different QDs of arrays [a-c] (the black, red, and green columns are for the QDs on arrays [a-c]) are shown. The enhancement factor was calculated by the intensity value on arrays [a-c] divided by the intensity value on the glass respectively. The intensity value can be obtained from the integration of the multi channel scalar (MCS) trace / the record time.



Figs. 6.2I(a-d) Fluorescence images of 50 different QDs on arrays [a-c] are shown in (a-c) and that on the glass is shown in (d). The fluorescence image areas are $4.75 \times 4.75 \mu\text{m}^2$.

II Statistic event numbers of the enhancement factors are taken from 50 different QDs of arrays [a-c]. Array [a] shows the highest quenching rate; while array [c] shows the highest enhancement rate. **III (a)** the MCS and **(b)** the TCSPC of one of the SQD picked up from the 50 QDs on arrays (a-c) and on the glass.

One of a segment of MCS trace is shown in Fig. 6.2III (a). The statistical quenching (enhancement) rate is defined as the rate of the quenching (enhancement) event numbers/total event numbers. The quenching rates (Q %) and enhancement rates (E %) were obtained from the target 50 QDs (classified by the enhancement factor). Since the error bar of the fluorescence intensity of the same point (obtained from the average of 10 measurements) of QDs is $\sim 5\%$. Therefore, we assume that when the intensity variation of the QDs fluorescence $> 10\%$, the extra variation is due to the phenomena of quenching or enhancement. For each point of QDs, the enhancement factor < 0.9 is classified as quenching, whereas the enhancement factor > 1.1 is classified as enhancement. For the 50 different QDs on arrays [a-c], the quenching rates are $\sim 46\%$, 10% and 8% respectively, and the enhancement rate are $\sim 42\%$, 74% and 82% respectively. We find that among the three array structures, the QDs fluorescence on array [a] exhibits the highest quenching rate, whereas that on array [c] exhibits the highest enhancement rate. According to the

results of the reflectance spectra of three different array structures in our previous paper [20], the LSP mode of array [c] is close to the fluorescence wavelength 705 nm [20]. The highest coupling efficiency is reached when the LSP resonance is formed [10]. In our case, the sparsest array structure provides such LSP resonance frequency coincidentally. Which is a key point indicated that among the three array structures, array [c] provides higher coupling efficiency for QDs fluorescence enhancement. In other words, QDs fluorescence on array [c] can be efficiently enhanced due to it is the sparsest array structure where forms the LSP resonance.

In Figs. 6.2III (a) and (b), the multi channel scalar (MCS) trace and the Time-Correlated Single Photon Counting (TCSPC) histogram of one of the SQD picked up from the 50 QDs on arrays [a-c] and on the glass are shown respectively.

The MCS trace reveals the SQD fluorescence intensity fluctuation in ~ 15 s, and the TCSPC histogram reveals the SQD fluorescence lifetime statistics (recording time: 1 min). According to TCSPC histograms, the fluorescence intensities of SQD on arrays [a-c] and on the glass can be fitted by single exponential decay: $I = A_0 + A_1 e^{-t/\tau_1}$. In the case as shown in Fig. 6.2III, the SQD is not close to the Au coated SiNRs on arrays [a-c], so that the quenching effects are avoided. The enhancement factors of the SQD on arrays [a-c] are 0.91, 2.40 and 3.63, and the lifetimes (τ_1) are 50.12 ns, 47.90 ns, and 49.57 ns respectively.

We further investigated the influence of the relative locations between the SQD and the Au coated SiNR of array [c] as shown in Figs. 6.3I-III. In Fig. 6.3I(a), six different relative locations (p1-p3, d1-d2, x) of the same SQD fluorescence image are shown. The six SQD fluorescence image areas shown in Fig. 6.3I(a) are $3 \times 3 \mu\text{m}^2$. In order to define the relative locations between the SQD and the Au coated SiNR, we removed the long pass 500 nm filter, and focused the laser light near each array substrate. Therefore, the substrate regions are bright and the Au coated SiNR regions are dark, such that the array structures

are distinguishable. The stability of the system was carefully checked by comparing the drift distances (< 2.5 nm in 1 min) of the SQD locations before and after measuring the reflection images. Array [c] was selected for the experiment since its optical reflectance image is the most obvious one. One of the reflectance images for defining the relative locations as shown in Fig. 6.3I(b) of array [c] was formed by scanning the same area with the fluorescence images as shown in Fig. 6.3I(a). Then, a schematic array with the peripheral (green short dash lines) and the diagonal (olive long dash lines) direction assisting lines for the following descriptions was additionally sketched. Fluorescence intensity of the same SQD was observed by randomly replacing array [c] on different relative locations. In Fig. 6.3I(b), six typical relative locations with color points labeled for the p1-p3 (for the peripheral directions), d1-d2, x (for the diagonal directions) of the same SQD are shown. The MCS trace shown in the insert of Fig. 6.3II(a) reveals the SQD fluorescence intensity fluctuation in ~ 5 s, and the TCSPC and the normalized TCSPC histograms in Figs. 6.3II(a)(b) reveal the SQD fluorescence lifetime statistics (recording time: 1min). In Figs. 6.3II(a)(b), the MCS traces and the TCSPC of the SQD on location x, d1-d2, p1-p3 on array [c] are shown. According to TCSPC histograms, the fluorescence intensities of SQD on array [c] also can be fitted by single exponential decay. The lifetimes (τ_1) of SQD on x, d1-d2, p1-p3 are 53.4 ns, 47.9 ns, 42.6 ns, 40.1 ns, 28.7 ns and 22.5 ns respectively. The corresponding enhancement factors on each one are 0.8, 2.0, 2.5, 2.7, 3.3 and 4.4. The higher enhancement factors are attributed to two reasons, the LSP coupling and the constructive interference. First of all, the LSP coupling process occurs as the SQD is located proximity to the boundary of the Au coated SiNR, e.g. locations d2 and p2-3. Second, the SQD fluorescence is enhanced when SQD is located near the mid point of two Au coated SiNRs where the constructive interference is formed, e.g. locations d1 and p1. However, when the SQD touches the Au coated SiNR, e.g. location x, the enhancement factor is decreased due to the dissipation process.

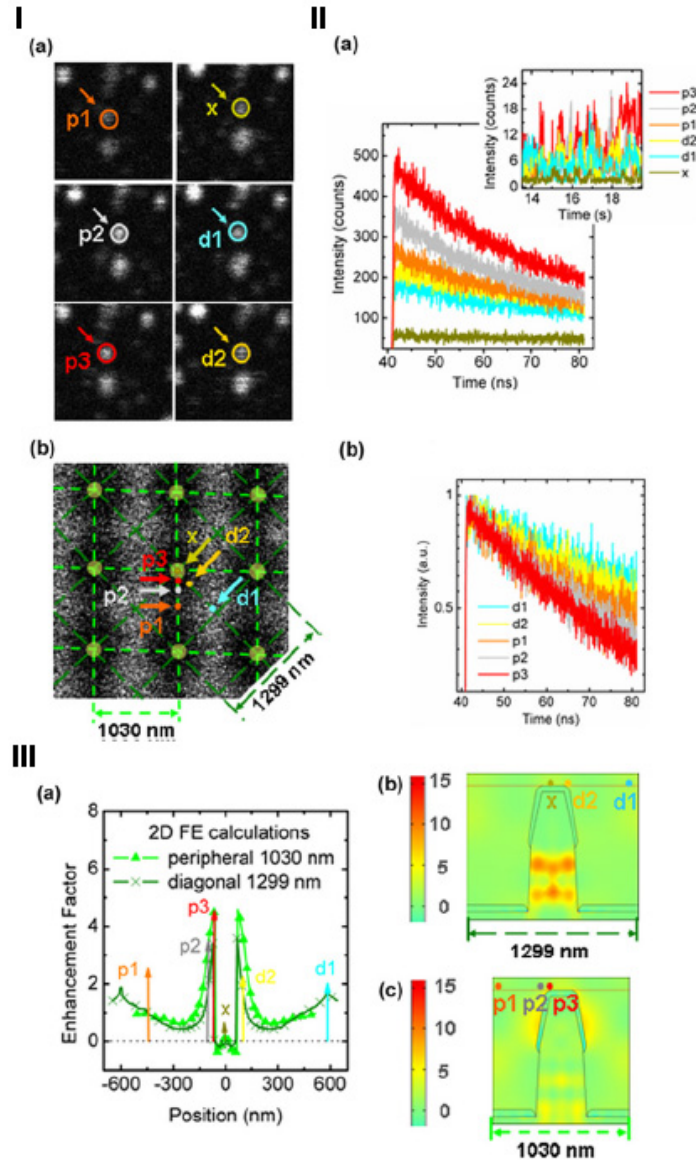


Fig. 6.3I(a) The QDs fluorescence images for six different relative locations (labeled as $p1$ - $p3$, $d1$ - $d2$, x). The images areas are $3 \times 3 \mu\text{m}^2$. **(b)** The reflectance image combined with schematic square unit cell of array [c] and color points labeled for six different locations ($p1$ - $p3$ (the peripheral direction), $d1$ - $d2$ (the diagonal direction), x (the center of Au coated SiNR)) of the same SQD are shown. **II (a)** TCSPC and MCS trace (the insert) **(b)** Normalized log scale TCSPC of the SQD on locations x , $d1$ - $d2$, $p1$ - $p3$ of array [c] (dark yellow, blue, yellow, orange, gray and red line). **III (a-c)** 2D FE calculations of unit cell of array [c] are shown (color labels x , $d1$ - $d2$, $p1$ - $p3$ from the experiments are listed for comparison). **(a)** “position vs. enhancement factors” on 0 nm line above Au coated SiNR. The normalized time average total energy densities in the diagonal direction (the olive line) and the peripheral direction (the green line) of the unit cell are shown in **(b)** and **(c)** respectively. The color codes for (b-c) are the absolute values of the time average total energy densities normalized to the incident total energy densities.

In Figs. 6.3III(a-c), we used the FEM [19] simulations as implemented in the FEMLEB code (www.femlab.de) to calculate the time average total energy densities on a unit cell of array [c] for comparing with the experiment results. The simulation details can be found in our previous papers [12, 20]. The Helmholtz wave equation was solved within a unit cell by employing periodic boundary conditions for each case. And the TM mode plane wave based calculations corresponding to the LSP resonance were obtained. In Fig. 6.3III(a), “the enhancement factors vs. the position” on the 0 nm line above the Au coated SiNRs is shown for both the peripheral (green line) and the diagonal (olive line) direction on array [c]. Consistent with the experiment results, we find that on the center regions 0 nm line above the Au coated SiNR (location x), the enhancement factor is about 0 which is corresponding to the quenching effect. Whereas on the boundary regions (locations d2 and p2-3) of the Au coated SiNR, and the constructive interference regions (locations d1, p1), the enhancement factors are higher. The time average total energy densities on a unit cell of array [c] at incident wavelength 705 nm in the diagonal and peripheral direction are shown in Figs. 6.3III(b) and (c) respectively.

§ 6-3 Conclusion

In conclusion, we found QDs fluorescence on the sparsest array structure shows the highest enhancement rate due to the highest coupling efficiency with the radiative LSP resonance frequency; whereas QDs fluorescence on the densest array structure shows the highest quenching rate due to the largest contact areas with the Au coated SiNRs which provide the largest regions for the fluorescence dissipation. Further, from the observations with identified relative locations between the QDs and the array structures, we found the QDs fluorescence enhancement effects are observed on the locations proximity enough (but not touched by the Au) to the Au coated SiNRs, and on the locations near the mid

point of two Au coated SiNRs. Similar conclusion can be found in other geometric metal nano structures, and both the enhancement and quenching phenomenon can be explained by the FEM and the coupled-mode theory [22]. For the example of a silver nanotip as shown in Figs. 1.5(a-c) [22], when the emitter is placed very close to the nanotip (at the distance $k_0d = 0.002$), the emitter decays primarily nonradiatively. When the emitter is placed a little far to the nanotip (at the distance $k_0d = 0.2$), the emitter can efficiently excite the guided plasmons. And when the emitter is placed at the proper location (at the distance $k_0d = 0.7$), the emitter decays radiatively. Where k_0 is the wave vector in the free space.

References

- 
- [1] Ritchie R H *Phys. Rev.* **106** 874 (1957)
- [2] Stern E A and Ferrell R A *Phys. Rev.* **120**, 130 (1960)
- [3] Barnes W L, Dereux A and Ebbesen T W *Nature* **424**, 824 (2003)
- [4] Gueroui Z and Libchaber A *Phys. Rev. Lett.* **93**, 166108 (2004)
- [5] Pons T, Medintz I L, Sapsford K E, Higashiya S, Grimes A F, English D S and Mattoussi H *Nano Lett.* **7**, 3157 (2007)
- [6] Larkin I, Stockman M, Achermann M and Klimov V *Phys. Rev. B* **69**, 121403 (2004)
- [7] Gryczynski I, Malicka J, Jiang W, Fischer H, Chan W, Gryczynski Z, Grudzinski W and Lakowicz J J. *Phys. Chem. B* **109**, 1088 (2005)
- [8] Wang Y, Yang T, Tuominen M T and Achermann M *Phys. Rev. Lett.* **102**, 163001 (2009)
- [9] Kulakovich O, Strekal N, Yaroshevich A, Maskevich S, Gaponenko S, Nabiev I, Woggon U and Artemyev M *Nano Lett.* **2**, 1449 (2002)
- [10] Song J-H, Atay T, Shi S, Urabe H, and Nurmikko A V *Nano Lett.* **5**, 1557 (2005)

- [11] Chang D E, Sørensen A S, Hemmer P R and Lukin M D *Phys. Rev. Lett.* **97**, 053002 (2006)
- [12] Christiansen S H, Chou J W, Becker M, Sivakov V, Ehrhold K, Berger A, Chou W C, Chuu D S and Gösele U *Nanotechnology* **20**, 165301 (2009)
- [13] Félidj N., Aubard J., Lévi G. *Phys. Rev. B* **65**, 075419 (2002)
- [14] Ibach Harald and Lüth Hans *Solid-State Physics —An Introduction to Principles of Materials Science*, Second Edition, Springer (2002)
- [15] Christiansen S H, Becker M, Fahlbusch S, Michler J, Sivakov V, Andrae G and Geiger R *Nanotechnology* **18**, 035503 (2007)
- [16] Becker M, Sivakov V, Goesele U, Stelzner T, Andra G, Reich H J, Hoffmann S, Michler J and Christiansen S H *Small* **4**, 398 (2008)
- [17] Maier S A, Kik P G, Atwater H A, Meltzer S, Harel E, Koel B E and Requicha A G *Nature Material* **2**, 229 (2009)
- [18] Bozhevolnyi S I, Smolyaninov I I and Zayats A V *Phys. Rev. B* **51**, 17916 (1995)
- [19] Jin Jianming, *The Finite Element Method in Electromagnetics*, 2 Edn, New York: Wiley (2002)
- [20] Chou J W, Lin K C, Lee Y J, Yuan C T, Hsueh F K, Shih H C, Fan W C, Luo C W, Lin M C, Chou W C, Chuu D S *Nanotechnology* **20**, 305202 (2009)
- [21] <http://tools.invitrogen.com>
- [22] Chang D.E., Sørensen A.S., Hemmer P.R., Lukin M.D. *Phys. Rev. Lett.* **97**,053002 (2006)

Chapter 7 Surface Enhanced Raman Scattering

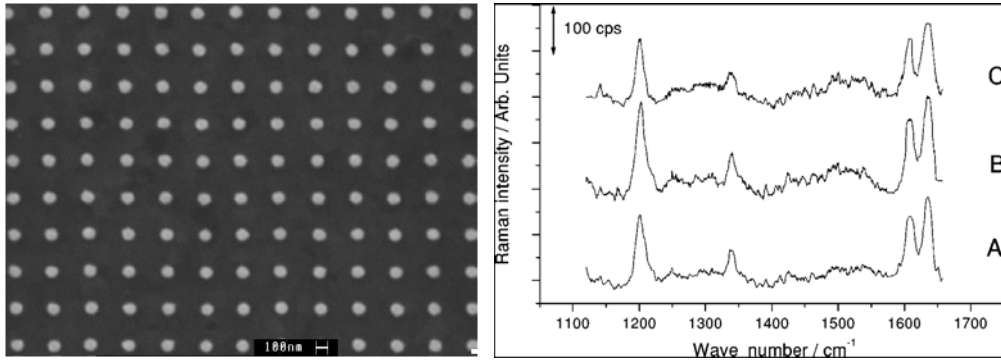
Observed on Spatially Controlled Array Structures

Before starting to discuss the topic of this chapter, the surface enhanced Raman scattering (SERS) applications investigated by N. Félidj et al. will be reviewed firstly in the following. Félidj et al. reported regular gold particle arrays exhibit remarkable optical properties and appear to be suitable substrates for the SERS effect. The resonances of the surface plasmons (SPs) localized on the particles with extinction spectra at wavelength from visible to near-infrared are corresponding to the SERS effects. The localized surface plasmons (LSPs) resonance frequencies can be tuned to almost any desirable wavelength by varying the particle shape, size, and spacing, thus optimizing the SERS [1]. In their experiment, the SERS study of $10^{-5}M$ trans-1, 2-bis (4-pyridyl) ethylene (BPE) aqueous solution adsorbed on three arrays (with different lattice constants) was carried out, and SERS spectra are shown in Figs. 7.1.

The enhancement effect was defined as the ratio of the intensity in presence and in absence of the metallic substrate [2-8]. Consider a molecule (assumed as a polarizable point dipole) is localized close to a metallic surface. Under this condition, the field enhancement (defined as the enhancement factors G) is proportional to the product of the local field enhancement at the incident and at the scattered Raman Stokes frequencies [1][9-16], as shown in Eq. (7.1):

$$\mathbf{G}_{\text{SERS}} \propto \frac{|\mathbf{E}_{\text{loc}}(\omega_{\text{exc}})\mathbf{E}_{\text{loc}}(\omega_{\text{RS}})|^2}{|\mathbf{E}_{\text{inc}}(\omega_{\text{exc}})\mathbf{E}_{\text{inc}}(\omega_{\text{RS}})|} = \mathbf{g}(\omega_{\text{exc}})\mathbf{g}(\omega_{\text{RS}}). \quad (7.1)$$

Where $\mathbf{E}_{\text{loc}}(\omega_{\text{exc}})$ and $\mathbf{E}_{\text{loc}}(\omega_{\text{RS}})$ are the local electric fields at the laser ω_{exc} and Raman ω_{RS} angular frequencies, respectively. $\mathbf{E}_{\text{inc}}(\omega_{\text{exc}})$ and $\mathbf{E}_{\text{inc}}(\omega_{\text{RS}})$ are the amplitude of the incident fields at these angular frequencies. The G values in this paper deduced to be in the order of $10^4 \sim 10^5$.



Figs. 7.1 In the left side of the figure, SEM image of one of the three gold particle square grating (The grating constant is 300 nm) is shown. The diameter of the particles parallel to the substrate is 110 nm and the particle height is 60 nm. In the right side of the figure, SERS spectra of $10^{-5} M$ BPE aqueous solution for gratings A, B, and C (with spacing between particles 200, 250, and 300 nm, respectively) are shown. All the spectra were recorded under identical experimental conditions: laser excitation 632.8 nm; power 3 mW at the sample, slit width 300 nm; three accumulations of 180 s counting time each. The spectra are vertically shifted for clarity [1].

The way to evaluate the absolute enhancement factor of the SERS is still under debate [17, 18]. Enhancement factors in a broad range from several folds to the order of 10^{14} can be found in previous papers [19, 1, 20-22, 9-26]. Compare to our SERS results (the details will be described later), we define the enhancement factor in a different way as the ratio of the measured intensity in presence on the metallic array structure and in presence on metallic plane surface. We will get the enhancement factors within the order of 10^2 , which can be converted to the conventional G factors (as defined in this paper [1], the ratio of the intensity in presence and in absence of the metallic substrate) to the same order of $10^4 \sim 10^5$, too.

Now let's start to discuss our study. In our work, SERS on three different nano-sized array structures of the gold-coated silicon nanorods (SiNRs) were observed on every measured location. On the surface of densest gold-coated SiNR array structure where the strongest electromagnetic field formed, we observed the highest enhancement factors. Based on electromagnetic theories, 2D finite element method (FEM) simulation which can be helpful for estimating the enhancement factors was used to calculate the localized electromagnetic field of the three array structures.

§ 7-1 Introduction

SERS first discovered by Martin Fleischman et al. in 1974 [27] and has been investigated over 30 years. Raman scattering was found to be enhanced by molecules adsorbed on rough metal surfaces [27], the nano-sized metal particles, and the nano-sized metal array structures [22, 23, 28]. Two main different theories are helpful to explain the SERS effects, *i.e.* the electromagnetic theory which explains the SERS effects by exciting the LSPs [29] and the chemical theory which explains the SERS effects through the formation charge-transfer complexes [30]. Although the exact mechanism of the SERS effects is still under debate, due to its potential in applications, SERS relative topics remain hot till now. Especially in the modern age, due to the progress in fabrication technology of nanostructures, more effective SERS substrates are available. In this chapter, we designed three different array structures for the effective SERS applications. The geometric size and shape of Au coated SiNRs in the three different array structures are fixed, and the distances between the Au coated SiNRs are varied for spatial controlling the LSP resonance modes [31]. On our three array structures which provide conditions for excitation of the LSP resonance modes, the SERS effects are effective and obvious. For further understanding the observation results, 2D finite element (FE) [32-33] simulations based on

electromagnetic theory were applied for systematically interpretations. FEM is a good choice for solving the near field distributions in our system. By breaking up the computational domain into elements with simple shapes and solving the Maxwell equations within, the near field distributions over domains even with complicated geometries such as our Au coated SiNR arrays can be conceptually solved piece by piece.

§ 7-2 Experiment Results

In our experiments, the periodic SiNR arrays on Si (100) wafers (n-type, 27 Ω -cm) were fabricated by electron beam lithography (EBL) and followed by Transformer Coupled Plasma (TCP) etching which is able to provide capability to etch nanoscale features into silicon and metal films. After SiNR arrays were constructed, a thickness of 50 nm gold thin films by electron gun was deposited on the surfaces and the Au coated SiNR arrays were formed. Three samples of Au coated SiNRs of same diameters but with different shortest root distances (210 nm, 380 nm, and 650 nm) between the nearest neighbor Au coated SiNR arrays were prepared for the experiments. Every single Au coated SiNR (in the three array structures) is not uniform cylinder. On the top side, the SiNR is with Au coated (the diameter is \sim 200 nm); whereas on the root side, SiNR is without Au coated (the diameter is \sim 380 nm). And the length of the SiNR is \sim 900 nm. SEM images of the three array structures used as the SERS substrates in our experiments are shown in Figs. 7.2I(a)-(c).

The SERS substrates were exposed to $10^{-5} M$ aqueous crystal violet (CV) solution for 10 min and then rinsed with deionized water (for minimizing the CV molecules adsorbed on the metal surfaces). Finally the samples were dried by the nitrogen gun. A high resolution (band analysis in the order of 0.3 cm^{-1} to 1 cm^{-1}) Raman spectrometer (Horiba Jobin Yvon LabRAM HR800) is used during our SERS experiment. He-Ne (633 nm) laser with an intensity of 6.4 mW was set as the incident source, and the objective

$\times 50$ (numerical aperture: 0.75) was used during the experiments. The laser beam was focused on the surface of the samples with the reduced intensity ~ 0.45 mW. The incident laser beam hit the sample surface in the normal direction of the sample substrate and the laser beam was focused to the minimized spot size with diameter of $\sim 1.8\mu\text{m}$, $3.4\mu\text{m}$, and $3.4\mu\text{m}$ on array (a)-(c) which covered about 7.3, 15.7, and 8.6 elements of the square lattice defined on array (a)-(c) respectively as shown on Figs. 7.2II(a)-(c).

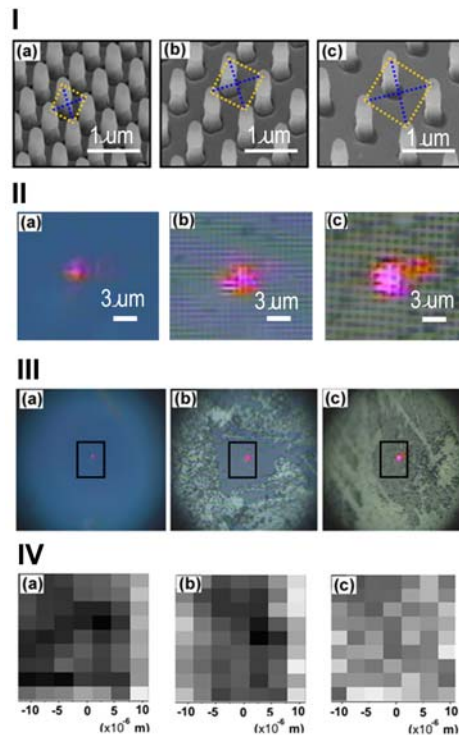
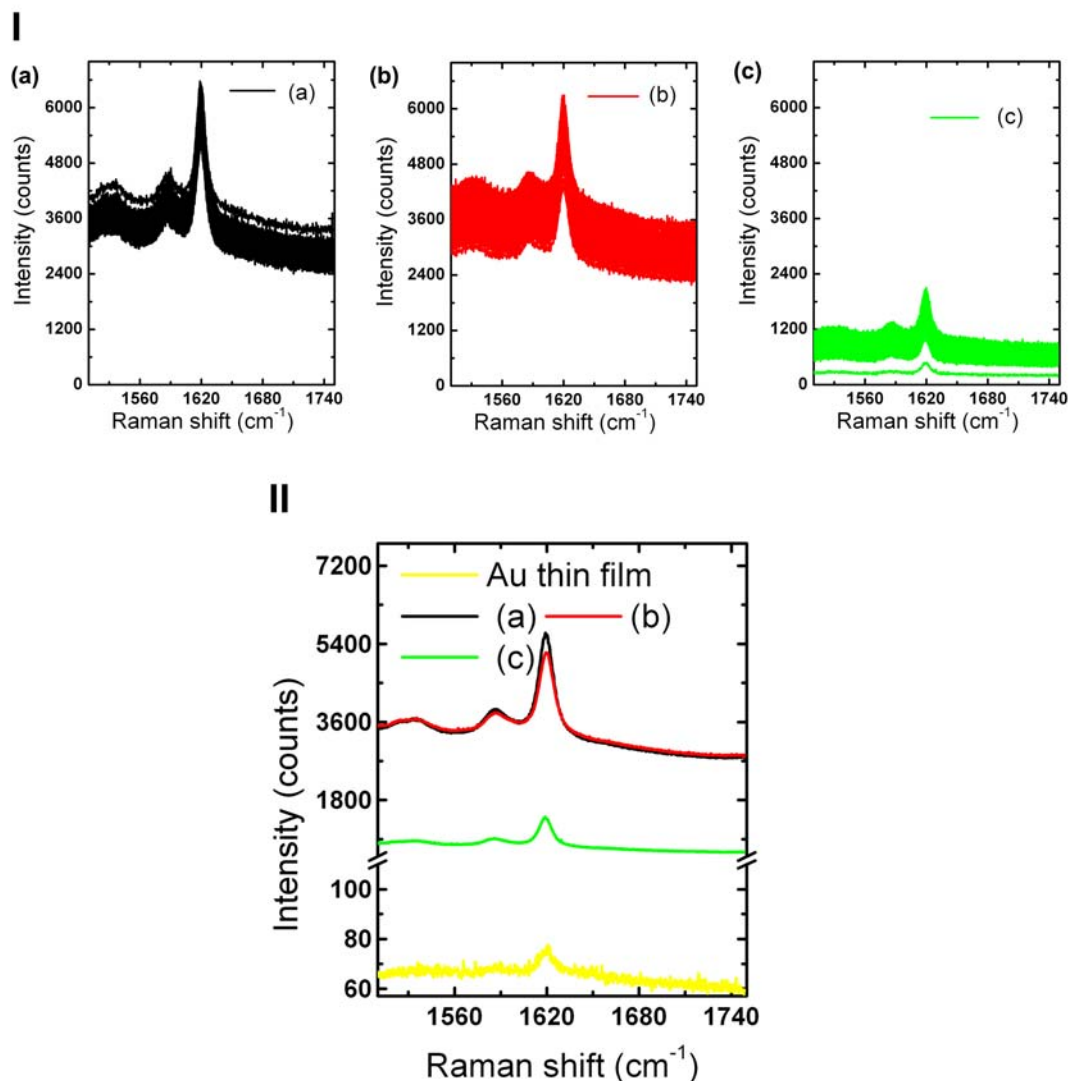


Fig. 7.2.I(a)-(c) SEM images of Au coated SiNR arrays (a)-(c). Scalar bars shown in (a)-(c) are $1\ \mu\text{m}$. In the square unit cell of each array, both the peripheral direction of the unit cell (the length: 590 nm, 780 nm, and 1030 nm (yellow dash line)) and the diagonal direction of the unit cell (677 nm, 917 nm, 1299 nm (blue dash line)) will be included in 2D FEM calculations (represented later). **II(a)-(c)** Optical images (Objective $\times 50$) near the focus spot regions of the excitation HeNe laser (power ~ 0.45 mW, wavelength: 633 nm) on arrays (a)-(c) are shown. The diameter of the focus spot size on array (a) is $\sim 1.8\ \mu\text{m}$, (b) is $\sim 3.4\ \mu\text{m}$, and (c) is $\sim 3.4\ \mu\text{m}$. Scalar bars shown in (a)-(c) are $3\ \mu\text{m}$. **III(a)-(c)** Larger regions of the optical images (Objective $\times 50$) of arrays (a)-(c) are shown, the image sizes are $\sim 106\ \mu\text{m} \times 112\ \mu\text{m}$. **IV(a)-(c)** Three of the mapping images (step: $3\ \mu\text{m}$) of Au coated SiNR arrays (a)-(c) are shown, the image sizes are $\sim 21\ \mu\text{m} \times 27\ \mu\text{m}$. The mapping regions were chosen from small regions (the black rectangle marks) of the whole optical images as shown in **III(a)-(c)**. The maximum gray levels (the brightest squares) in **IV(a)-(c)** are corresponding to the maximum SERS intensities (for the crystal violet (CV),

the Raman shift center at $\sim 1620 \text{ cm}^{-1}$); the maximum SERS intensity for array (a) is ~ 6570 (counts), array (b) is ~ 6280 (counts), and array (c) is ~ 2100 (counts).



Figs. 7.3I(a)-(c) SERS on 63 different locations of Au coated SiNR arrays (a)-(c) (black, red, and green line) are corresponding to the mapping images shown in **Figs. 7.2IV(a)-(c)**. The SERS spectra of crystal violet in the observed region contains three characteristic peaks (1533 cm^{-1} , 1585 cm^{-1} , 1620 cm^{-1}) are from C-C stretching modes [22, 34-35]. **II** Average SERS (from the 63 different locations) on array (a)-(c) (the black, red, and green line) and on the Au thin film (the yellow line). The enhancement factor at 1620 cm^{-1} (defined by (the average intensity value of Raman signals on each array)/ (the average intensity value of Raman signals on the Au thin film)) on array (a) is ~ 73.0 , array (b) is ~ 67.6 , and on array (c) is ~ 17.9 .

The SERS signal from the sample was collected by the thermoelectrically cooled charge couple device (CCD). On each sample, the Raman signals in the marked black rectangular

regions (size: $21\mu\text{m} \times 27\mu\text{m}$) as shown in Figs. 7.2III(a)-(c) were investigated. Inside each black rectangular region, there are $7 \times 9 = 63$ measurement locations. The mapping of Raman signals (at the Raman shift center $\sim 1620\text{ cm}^{-1}$) obtained from the 63 locations (formed a matrix (step $3\mu\text{m}$)) on array (a)-(c) is shown as gray levels in Figs. 7.2IV(a)-(c) respectively. The integration time during each measurement was set 30 s. The SERS spectra were analyzed with program LabSpec.

In Figs. 7.3I(a)-(c), the Raman spectra of the 63 locations on array (a)-(c) are shown respectively. The SERS effects were observed on every measured locations on each array. The maximum SERS intensity at the Raman shift center $\sim 1620\text{ cm}^{-1}$ for array (a)-(c) is ~ 6570 (counts), 6280 (counts), and 2100 (counts). In Fig. 7.3II, the average spectra acquired at the 63 locations on array (a)-(c) (the black, red, and green line) and on the Au thin film (with Au thickness 50 nm on Si substrate, the yellow line) are shown. The Au thin film is used as a comparison for estimating the enhancement factors. The enhancement factor is defined by (the average intensity value of Raman signals on each array)/ (the average intensity value of Raman signals on the Au thin film). The enhancement factor at 1620 cm^{-1} on array (a)-(c) is ~ 73.0 , 67.6 , and 17.9 .

§ 7-3 Discussion

Among the three array structures, the maximum SERS effects were observed on array (a) due to it has the most effective LSP excitation. We provide the experiment data of reflectance spectra as shown in Fig. 7.4 to support the argument. In reflectance spectra measurements, an incident angle of 5° from normal direction was set for the three different array structures. The un-polarized white light from a tungsten halogen lamp was

focused on the sample. The reflection spectra from three arrays structures were normalized to that of 50 nm Au thin films. The LSP modes can be tuned by varying the distances between Au coated SiNRs. The valleys shown in the reflectance spectra corresponding to the high optical fields are produced by the LSP modes [31, 36]. The valleys (labeled by “sp”) in the reflectance spectra as shown in Fig. 7.4 are corresponding to the nearest (to the excitation wavelength 633 nm) LSPs resonance modes. The excitation wavelength 633 nm is closest to the LSPs resonance mode provided by array (a), therefore array (a) has higher coupling efficiency and the maximum SERS effects were observed.

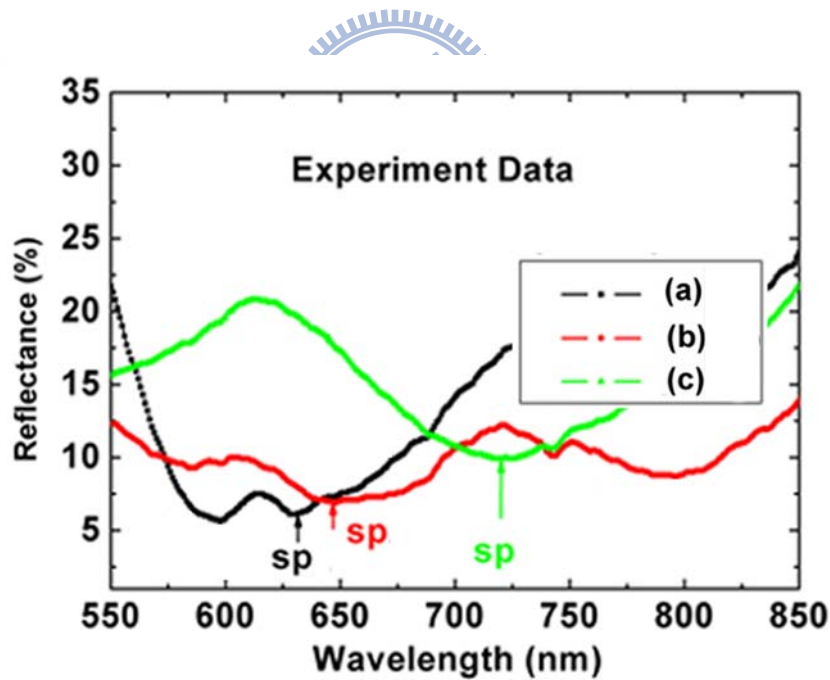


Fig. 7.4 Reflectance spectra of array (a)-(c) (the black, red, and green line) are shown. The valleys (labeled by “sp”) in the reflectance spectra are corresponding to the nearest (to the excitation wavelength 633 nm) LSPs resonance modes. The excitation wavelength 633 nm is closest to the LSPs resonance mode provided by array (a), therefore array (a) has higher coupling efficiency.

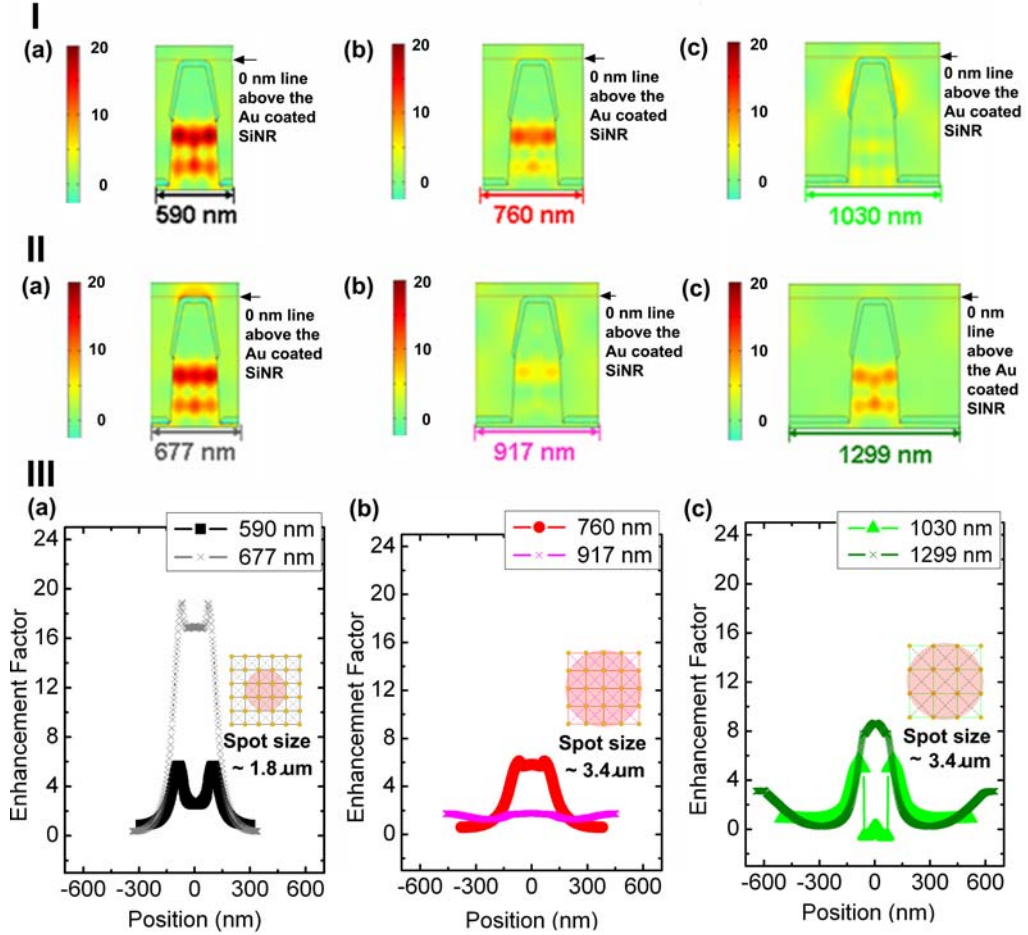
The way to evaluate the absolute enhancement factor of the SERS is still under debate [17-18]. Enhancement factors in a broad range from several folds to the order of 10^{14} can be found in previous papers [19, 21, 24-26]. The extra large enhancement factor (such as 10^{14}) although obtained from plausible assumptions regarding the surface density of adsorbed dye molecules cannot be directly available from the observation (since the detectable signals (Intensity (counts)) for CCD is not unlimited).

Back to our system, if one considers the ratio of (the total surface area of each array)/(the plan area of the Au thin film) inside its spot size, one can estimate that (the numbers of the molecules on the array (a)-(c))/(the numbers of the molecules on the Au thin film) inside each spot size is $\sim 3.45, 2.48$ and 1.81 respectively. Which are less than the enhancement factors of $73.0, 67.6,$ and 17.9 observed on array (a)-(c) in the experiment. Therefore, the number of the adsorbed molecule is not the only factor to influence the SERS.

In the following, the electromagnetic theory is involved to analyze our experiment results about the SERS. In Figs. 7.5I-III, we used the FEM [32-33] simulations as implemented in the FEMLEB code (www.femlab.de) to calculate the time average total energy densities on a unit cell of array (a)-(c) for comparing with the experiment results. The Maxwell equations were solved within a unit cell by employing periodic boundary conditions for each case. The TM mode plane wave based calculations corresponding to the LSP resonance were obtained. The simulation details can be found in our previous papers [31, 37].

In Figs. 7.5I-III, 2D FEM simulation results of the unit cell of array (a-c) at the Raman shift center 1620 cm^{-1} are shown respectively. In Figs. 7.5I(a)-(c), the normalized time average total energy densities of the unit cell in the peripheral direction of array (a)-(c) are shown, and in Figs. 7.5II(a)-(c), the normalized time average total energy densities of the unit cell in the diagonal direction of array (a)-(c) are shown. In Figs. 7.5III(a)-(c), “Position

versus Enhancement Factor” extracted the normalized time average total energy densities (at the excitation wavelength (633 nm) \times the Raman shift center 1620 cm^{-1}) from the position on 0 nm line above the Au coated SiNR of array (a)-(c) are shown.



Figs. 7.5I-III 2D FEM simulation results of the unit cell of arrays (a-c) at the Raman shift center 1620 cm^{-1} are shown respectively. The color codes for I-II are the absolute values of the time average total energy densities normalized to the incident total energy densities. The normalized time average total energy densities of the unit cell of arrays (a)-(c) are shown in I(a)-(c): the peripheral direction and II(a)-(c): the diagonal direction. III(a)-(c) “Position versus Enhancement Factor” extracted the normalized time average total energy densities (at the excitation wavelength (633 nm) \times the Raman shift center 1620 cm^{-1}) from the position on 0 nm line above the Au coated SiNR of arrays (a)-(c). The simulated average enhancement factor on array (a) is ~ 9.6 , array (b) is ~ 4.2 , and on array (c) is ~ 3.8 . Since the diameter of the focus spot size of array (a) is $\sim 1.8 \mu\text{m}$, (b) is $\sim 3.4 \mu\text{m}$, and (c) is $\sim 3.4 \mu\text{m}$. Inside the focus spot of arrays (a)-(c), there are ~ 7.3 , 15.7 , and 8.6 elements of the square lattice respectively. Therefore, the calculated enhancement factor obtained from the spot size of array (a) is ~ 70.2 , array (b) is ~ 66.0 , and array (c) is ~ 32.5 .

This typical region is chosen because it is corresponding to the beam waist of Gaussian beam (the focal plane area, where the maximum intensity is formed). The simulated average enhancement factor (calculated from the summation of the average total energy density in the two peripheral and the two diagonal directions in a unit cell) on array (a)-(c) is ~ 9.6 , 4.2 , and 3.8 . Since the diameter of the focus spot size of array (a)-(c) is $\sim 1.8 \mu\text{m}$, $3.4 \mu\text{m}$, and $3.4 \mu\text{m}$ (optical image of the spot size as shown in Figs. 7.2II(a)-(c) and its schematic as shown in the inset of Figs. 7.5III(a)-(c)). The smaller spot size on array (a) (photonic crystal like) is due to the distance between the Au coated SiNRs is too short for the excitation laser with wavelength 633nm to propagate straight forwards in between. Inside the focus spot of arrays (a)-(c), there are ~ 7.3 , 15.7 , and 8.6 elements of the square lattice respectively. Therefore, the calculated enhancement factor obtained from (the average enhancement factor in unit cell) \times (elements of the square lattice in each spot size) of arrays (a)-(c) is $\sim 9.6 \times 7.3 = 70.2$, $4.2 \times 15.7 = 66.0$, and $3.8 \times 8.6 = 32.5$.

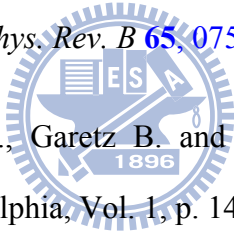
Except array (c), the simulated enhancement factors on arrays (a) and (b) are quite consistent with the enhancement factors obtained from the experiment. Since that the % of top area of the Au coated SiNR in array (c) is much less than 50% (the % can be calculated by $((\text{the diameter of a top SiNR})/(\text{the diameter of a unit cell}))^2$). Therefore, on array (c), the focus plane was more probable near the Au thin film substrate during the observation instead of on top of the Au coated SiNRs. However, in the simulation demonstrated previously, the average total energy density was obtained near the top of Au coated SiNRs. Therefore, especially on array (c), the enhancement factor obtained from the simulation result is much larger than the observation result.

§ 7-4 Conclusion

On the three Au coated SiNR array structures prepared by EBL, effective SERS of the molecules CV were observed. Among the three array structures, the maximum SERS was

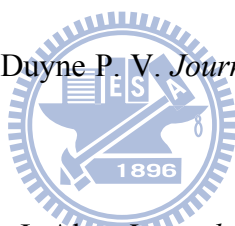
observed on the densest array structure mainly due to the highest coupling efficiency with the excitation LSP resonance frequency. However, the densest array structure with the distance between two nearest SiNRs below the diffraction limitation can lead to the excitation laser spot size decreasing, and the SERS effects are curtailed. Based on the electromagnetic theory, 2D FEM simulation results can support our arguments and are helpful to analyze the experiment results. The array structures we studied were fabricated by well-established silicon technology and are reproducible. By precisely designing, more efficient composite optical devices can be developed.

References

- 
- [1] Félidj N., Aubard J., Lévi G. *Phys. Rev. B* **65**, 075419 (2002)
- [2] Birke R. L., Lombardi J. R., Garetz B. and Lombardi J. R. *Advances in Laser Spectroscopy*, Heyden, Philadelphia, Vol. 1, p. 143 (1982)
- [3] Chang R. K. and Furtak T. E. *Surface Enhanced Raman Scattering*, Plenum Press, New York (1982)
- [4] Moskovits M. *Rev. Mod. Phys.* **57**, 783 (1985)
- [5] Furtak T. E., Garetz B. and Lombardi J. *Advances in Laser Spectroscopy*, Heyden, Chichester, Vol. 2, p. 175 (1984)
- [6] Otto A., Cardona R. and Guntherodt G. *Light Scattering in Solids*, Springer, Berlin,, Vol. IV (1984); Garell R. L. *Anal. Chem.* 61, 401A (1989)
- [7] Hexter R. M. and Albrecht G. M. *Spectrochim. Acta, Part A* **35**, 233 (1979)

- [8] Bingler H.-G., Bruner H., Leitner A., Aussenegg F. R., and Wokaun A. *Mol. Phys.* **85**, 587 (1995)
- [9] Kerker M., Wang D. S. and Chew H. *Appl. Opt.* **19**, 4159 (1980)
- [10] Aravind P. K., Nitzan A., and Metiu H. *Surf. Sci.* **110**, 189 (1981)
- [11] Mc-Call S. L., Platzman P. M., and Wolf P. A. *Phys. Lett. A* **77**, 5, 381 (1980)
- [12] Gersten J. and Nitzan A. *J. Chem. Phys.* **73**, 3023 (1980)
- [13] Ruppin R. *Solid State Commun.* **39**, 903 (1981)
- [14] Weitz D. A., Garoff S., and Gramila T. J. *Opt. Lett.* **7**, 168 (1982)
- [15] Weitz D. A., Garoff S., Gersten J. I., and Nitzan A. *J. Chem. Phys.* **79**, 5324 (1983)
- [16] Bingler H.-G., Bruner H., Leitner A., Aussenegg F. R., and Wokaun A. *Mol. Phys.* **85**, 587 (1995)
- [17] Le Ru E. C. Blackie E., Meyer M., Etchegoin P. G. *J. Phys. Chem. C* **111**, 13794 (2007)
- [18] Cai W. B., Ren B., Li X. Q., She C. X., Liu F. M., Cai X. W., Tian Z. Q. *Surf. Sci.* **406**, 9 (1998)
- [19] Becker, M. , Sivakov V., Andrä G., Geiger R., Schreiber J., Hoffmann S., Michler J., Milenin A. P., Werner P., and Christiansen S. H. *Nano Letters* **7**, 75 (2007)
- [20] Christiansen S. H., Becker M., Fahlbusch S., Michler J., Sivakov V., Andrae G., and Geiger R. *Nanotechnology* **18**, 035503 (2007)
- [21] Becker M., Sivakov V., Goesele U., Stelzner T., Andra G., Reich H. J., Hoffmann S., Michler J., and Christiansen S. H. *Small* **4**, 398 (2008)

- [22] Wang Y., Becker M., Wang L., Liu J., Scholz R., Peng J., Gösele U., Christiansen S., Kim D. H., Steinhart M. *Nano Lett.* **9**, 6, 2384 (2009)
- [23] Tsang J. C., Kirtley J. R. and Bradley J. A. *Phys. Rev. Lett.* **43**, 772 (1979)
- [24] Lyon S. A. and Worlock J. M. *Phys. Rev. Lett.* **51**, 593 (1983)
- [25] Murray C. A., Allara D. L. and Rhinewine M. *Phys. Rev. Lett.* **46**, 57 (1981)
- [26] Nie Shuming and Emory Steven R. *Science* **275**, 1102 (1997)
- [27] Fleischmann M., Hendra P.J. and McQuillan A.J. *Chem. Phys. Lett.* **26**, 163 (1974)
- [28] Perchee J. Le, Quémerais P., Barbara A., and López-Ríos T. *Phys. Rev. Lett.* **100**, 066408 (2008)
- [29] Jeanmaire David L., Richard Duyne P. V. *Journal of Electroanalytical Chemistry* **84**, 1-20 (1977)
- [30] Albrecht M. Grant, Creighton J. Alan *Journal of the American Chemical Society* **99**, 5215 (1977)
- [31] Chou J W, Lin K C, Lee Y J, Yuan C T, Hsueh F K, Shih H C, Fan W C, Luo C W, Lin M C, Chou W C, Chuu D S *Nanotechnology* **20**, 305202 (2009)
- [32] Jin Jianming, *The Finite Element Method in Electromagnetics*, 2 Edn, (New York: Wiley) (2002)
- [33] Volakis John L., Chatterjee Arindam, Kempel Leo C. *Finite Element Method for Electromagnetics—antennas, microwave circuits, and scattering applications*, IEEE PRESS (1998)
- [34] Schneider S., Brehm G., Freunscht P. *Phys. Status Solidi B*, **189**, 37 (1995)



[35] Liang E. J., Ye X. L., Kiefer W. *J. Phys. Chem. A*, **101**, 7330 (1997)

[36] Song J-H, Atay T, Shi S, Urabe H, and Nurmikko A V *Nano Lett.* **5**, 1557 (2005)

[37] Christiansen S H, Chou J W, Becker M, Sivakov V, Ehrhold K, Berger A, Chou W C,
and Chuu D S, Gösele U *Nanotechnology* **20**, 165301 (2009)



Chapter 8 Conclusion

Starting from the enlightenment of M. D. Lukin's group [1], we investigated the localized surface plasmons (LSPs) [3-5] related topics. We have investigated how the quantum dots (QDs) [2] PL and the QDs fluorescence spontaneous emission rate can be influenced by Au caps on silicon nanowires (SiNWs). However, the geometric size and distribution of Au caps on SiNWs fabricated by electron-beam evaporation (EBE) are not uniform. This had resulted in difficulties when analyzing the LSPs [3-5] resonance modes. For further investigation, we therefore started series of the Au coated on Si nanorod (SiNR) array structures to investigate the LSP resonance modes. Three kinds of periodic Au coated SiNR array structures were fabricated by electron beam lithography (EBL) and followed by Transformer Coupled Plasma (TCP) etching. After SiNR array structures were constructed, a thickness of 50 nm gold thin films by electron gun were deposited on the surfaces. From the observation results via both the Scanning Near Field Optical Microscope (SNOM) and reflection spectra, we found the LSP resonance modes can be spatially controlled by the array structures [6]. The longer the distance between the Si nanorods (SiNRs) performed the lower the LSP frequency.

Furthermore, we found QDs fluorescence (fluorescence center~ 705 nm) on the sparsest array structure shows the highest enhancement rate due to the highest coupling efficiency with the radiative LSP resonance frequency. We also found QDs fluorescence on the densest array structure shows the highest quenching rate due to the largest contact area with the Au coated SiNRs which provide the largest region for the fluorescence dissipation. And from the observations with identified relative locations between the QDs and the array structures, we found the QDs fluorescence enhancement effects are observed on the

locations proximity enough (but not touched by the Au) to the Au coated SiNRs, and on the locations near the mid point of two Au coated SiNRs. In the first case, by coupling with the LSP resonance, the QDs fluorescence enhancement effects with shorter lifetime are observed. While in the second case, by interacting with the constructive interference, the QDs fluorescence enhancement effects with longer lifetime (compared to the LSP coupling cases) are observed. We found again that when the QDs contact with Au coated SiNRs, instead of enhancement, a non-radiative process may lead to QDs fluorescence quenching.

Finally, Surface Enhanced Raman Scattering (SERS) of crystal violet (CV) molecules on the three array structures of the gold-coated SiNR were also investigated. The enhancement factor is defined as the ratio of the measured CV Raman signal intensity in presence on the gold-coated SiNR array structure and in presence on gold thin film plane surface. On the surface of densest gold-coated SiNR array structure where the strongest electromagnetic field is, we observed the highest enhancement factor (~ 73). The excitation source (wavelength 633 nm) can excite the LSP on the densest array structure with the highest efficiency is the main reason for the highest enhancement factor. However, we found that the densest array structure with the distance between two nearest SiNRs below the diffraction limitation can lead to the excitation laser spot size decreasing, and the SERS effects are curtailed.

By 2D finite element method (FEM) [7-8] simulation results which calculated the enhancement factors on different positions (with the specific frequency) and near field distributions of the array structures, we can analyze the LSP resonance modes formed on each case. Once the LSP resonance frequencies are tuned to couple with the frequency of the excitation source, the highest enhancement factors can be reached. The spatial distributions of total energy densities in the array structures (corresponding to the enhancement and the dissipation effects in the near field region) are predicted and are consistent with the experiment results.

The array structures we studied were fabricated by well-established silicon technology and are reproducible. By implementing exquisite design, more efficient quenching/enhancement composite optical devices can be further fabricated.

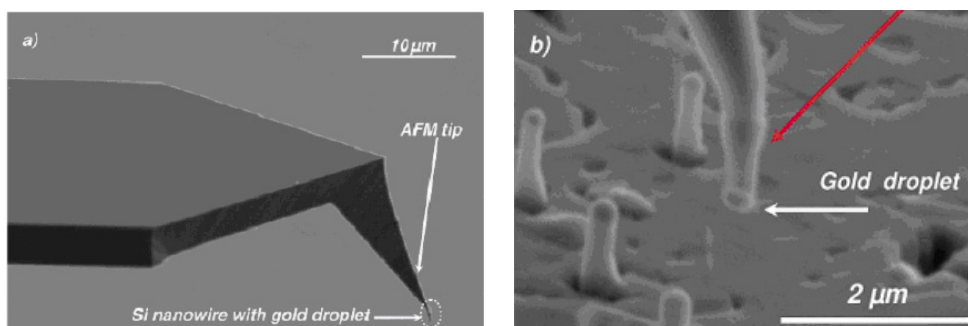
References

- [1] Akimov A. V., Mukherjee A., Yu C. L., Chang D. E., Zibrov A. S., Hemmer P. R., Park H. & Lukin M. D. *Nature* **450**, 402 (2007)
- [2] <http://tools.invitrogen.com>
- [3] Ritchie R. H. *Phys. Rev.* **106**, 874 (1957)
- [4] Stern E. A. and Ferrell R. A. *Phys. Rev.* **120**, 130 (1960)
- [5] Barnes W L, Dereux A and Ebbesen T W *Nature* **424**, 824 (2003)
- [6] Chou J W, Lin Kao-Chin, Lee Yao-Jen, Yuan Chi-Tsu, Hsueh Fu-Kuo, Shih Hsun-Chuan, Fan Wen-Chung, Luo Chih-Wei, Lin Ming-Chieh, Chou Wu-Ching, Chuu Der-San *Nanotechnology* **20**, 305202 (2009)
- [7] Jin Jianming, *The Finite Element Method in Electromagnetics*, Second Edition, JOHN WILEY & SONS. INC. (2002)
- [8] Volakis John L., Chatterjee Arindam, Kempel Leo C., *Finite Element Method for Electromagnetics – antennas microwave circuits, and scattering applications*, IEEE PRESS (1998)

Chapter 9 Future Works

Relative to the topic of the surface-enhanced Raman spectroscopy (SERS) [1-5], the application in inspection of the food (aimed at the small amount additional dyes possibly found in the food) or for the detection of the low concentration molecules [6] which cannot be detected by conventional Raman spectroscopy is discussed in the future works. Different from the conventional Raman spectroscopy, via the SERS application, Raman signals of dyes (even with highly diluted concentration) are available on the rough metal surfaces, the nano-sized metal particles, and the nano-sized metal array structures [1-3].

Becker and Christiansen et al. [7] reported the malachite SERS and Tip-enhanced Raman spectroscopy (TERS) effects by gold droplets on top of nanowires (NWs) in 2007. By welding the gold droplets on top of Si nanowire (SiNW) to a standard AFM tip, one can produce a “nanowire (NW) TERS tip.” First, use ultrasonic treatment to break off the gold droplets on top of SiNWs from the Si substrate. Then, move the whole sample into the SEM chamber [8] to observe. Align one of the breaking off NWs to the standard AFM tip, and weld the single NW by the focus electron beam onto the standard AFM, as shown in Figs. 9.1. (a) and (b) [9].



Figs. 9.1 (a) AFM tip with the attached SiNW tip. **(b)** The magnified NW tip region, the gold droplet on the top of the NW is clearly visible [9].

The molecules malachite green SERS and TERS are then proceeded in SEM chamber. Soak another “standard gold-coated AFM tip” in the malachite green solution to put some malachite green molecules on it. Use the “NW TERS tip” in contact mode to approach “the standard gold-coated AFM tip” which with some malachite green molecules on it. When the incident laser (He-Ne 633nm) polarization is nearly parallel to the axial of the “NW TERS tip” and precisely focused on the top of the “standard gold-coated AFM tip,” and the “NW TERS tip” is close enough to the “standard gold-coated AFM tip” (several nm), one can get the best SERS and TERS effects (description shown in Fig. 9.2). However, the task of alignment usually needs a long time.

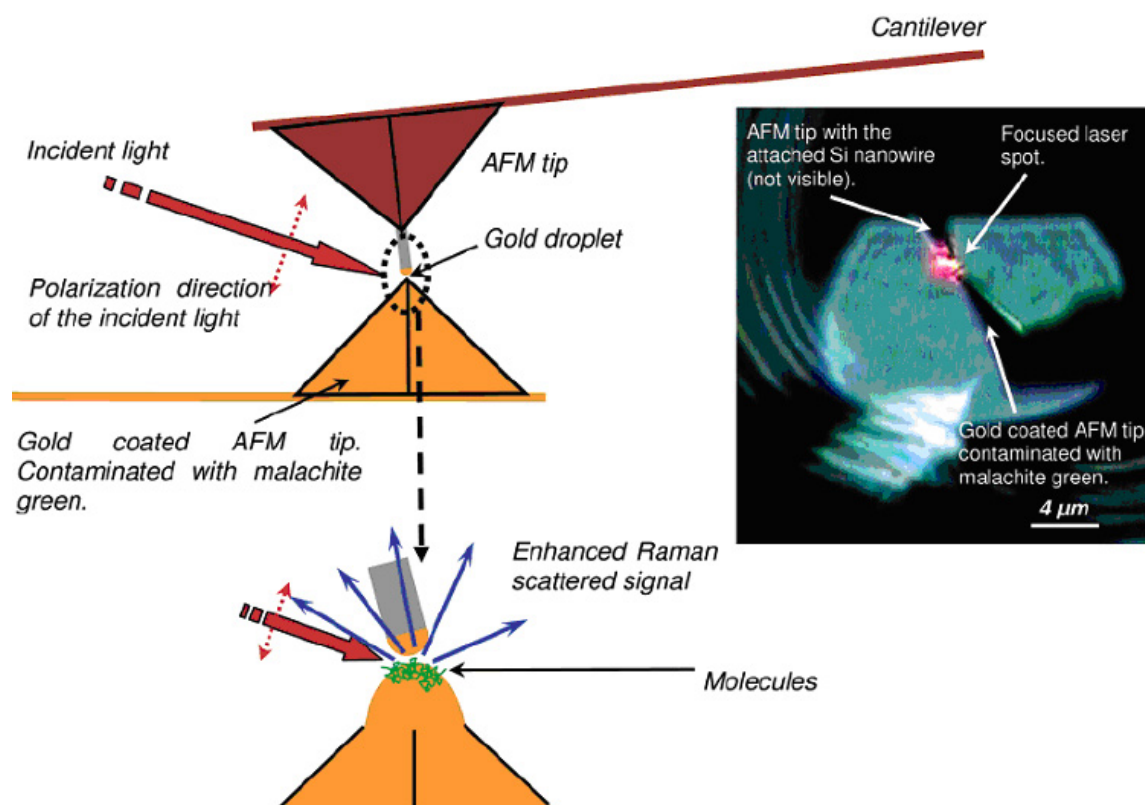


Fig. 9.2 Setup of the TERS measurement with SiNWs AFM tip. The incident laser polarization is nearly parallel to the axial of the “NW TERS tip” and precisely focused on the top of the “standard gold-coated AFM tip,” and the “NW TERS tip” is close enough to the “standard gold-coated AFM tip” (several nm), one can get the best SERS and TERS effects. The right side figure is the picture from the optical microscope [9].

The results of the malachite green molecules measurement are shown in Fig. 9.3 [9]. The blue spectrum shows the signal enhancement solely produced by the gold-coated sample tip. When the NW tip is in contact with the sample tip, the enhancement becomes 6-7 times larger (red spectrum).

As the future works, the SERS relative research will be considered to investigate by the Micro-Raman spectrometer (Jobin Yvon LabRam HR800, as illustrated in chapter 2, section 2-1) combined with AFM system in the experiments.

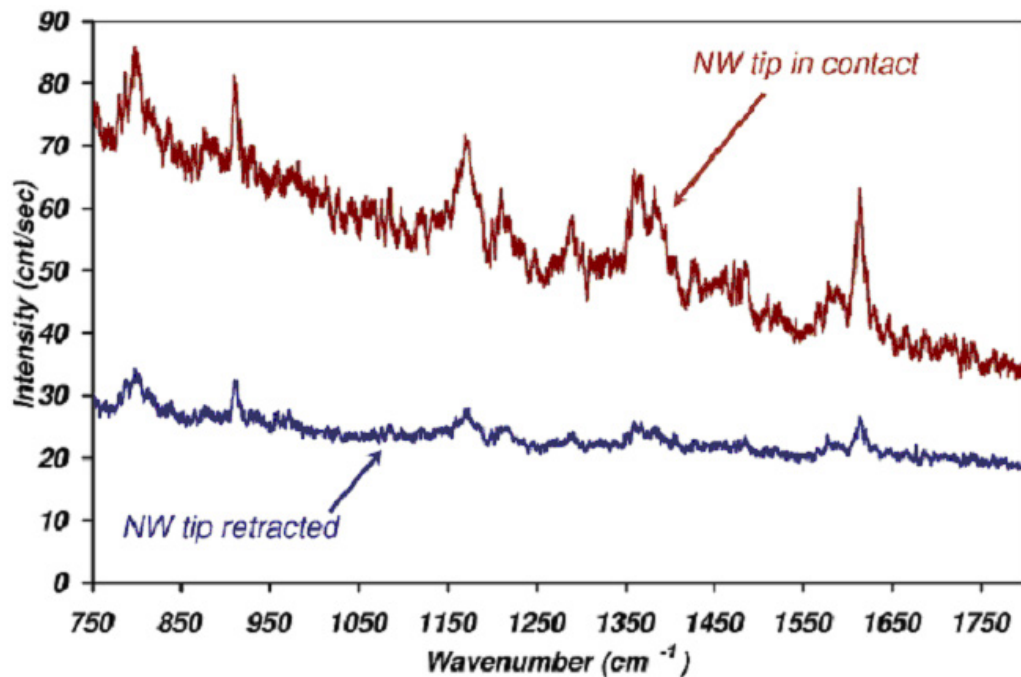
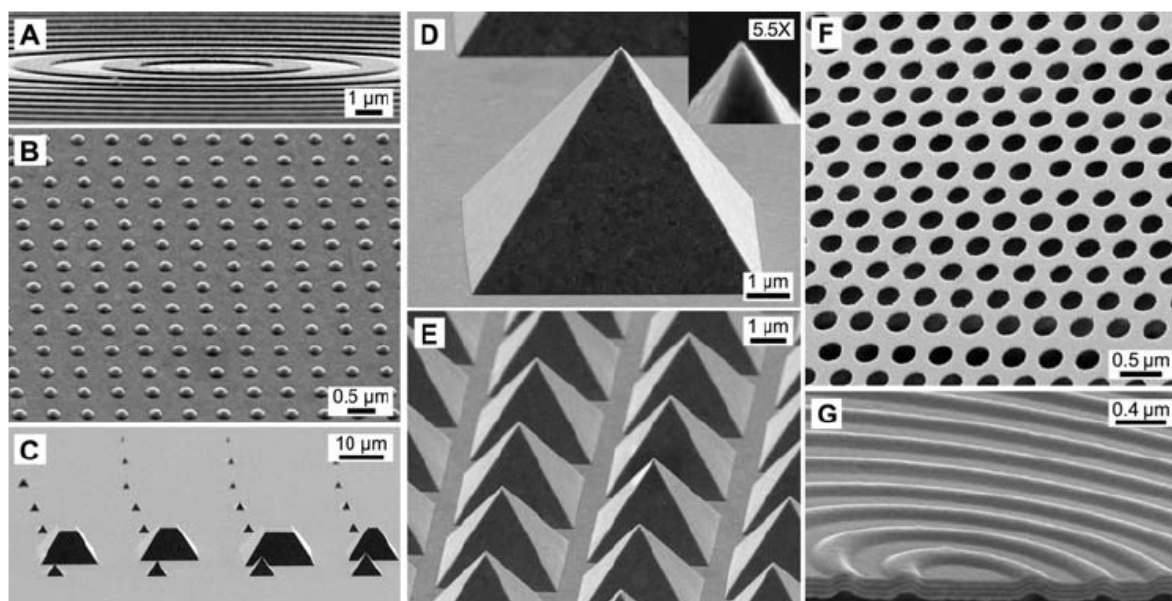


Fig. 9.3 Enhanced Raman spectra of malachite green between 750-1750 cm^{-1} . The blue spectrum shows the signal enhancement solely produced by the gold-coated sample tip. When the NW tip is in contact with the sample tip, the enhancement becomes 6-7 times larger (red spectrum) [9].

Since the SERS effects are relative to the localized surface plasmons (LSPs) which strongly dependent on the geometry of the metal surfaces. And for the array structures are geometrically periodic, they have advantages when analyzing. Except the Au coated Si

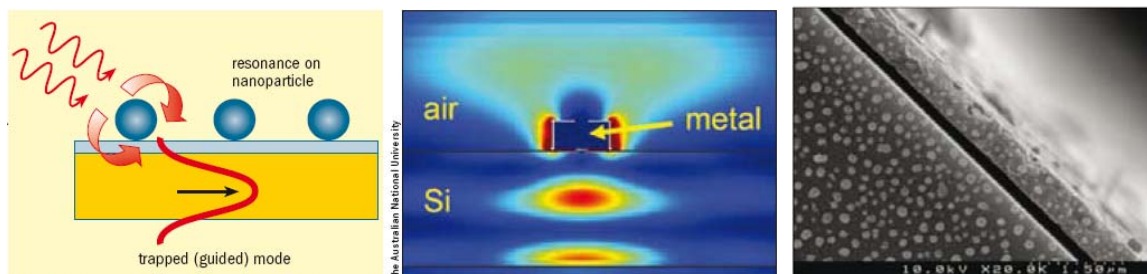
nanorod (SiNR) array structures illustrated in chapter 5, 6 and 7, we will consider another three series of Au coated SiNR array structures, *i.e.* the array structures with more different spacing between the Au coated SiNRs, the array structures with more different diameter and height of the Au coated SiNR array structures. The dimensions (the spacing, the diameter and the height) of the array structures will be considered large (or small) compared to the size of the quantum dots (QDs) or some large molecules.



Figs. 9.4 *Electron micrographs of various metal structures. A A copper bull's eye with 1.3- μm -wide circular grooves spaced every 3.5 μm ; the template was patterned with photolithography and reactive ion etching (RIE). B A square silver array of 240-nm-diameter bumps spaced every 600 nm; the template was patterned with focused ion beam (FIB). C and D A silver pyramid array made by anisotropic etching. A gold-on-chromium mask with square holes was formed with FIB on a silicon wafer and etched in KOH. The inset in D shows the tip of one of the pyramids. E A gold pyramid array made by anisotropic etching as in C, except a chromium mask was patterned with a hexagonal array of 1- μm -diameter circles spaced by 2.25 μm using photolithography. F A thin silver nanohole array made with template stripping and nanosphere lithography. 265-nm-diameter holes spaced by 450 nm were formed in a 30-nm-thick silver film. G A multilayer bull's eye with alternating layers of silver (30 nm) and alumina (15 nm). A cross section etched by FIB shows seven layers. [10].*

Further, we will also consider series of ultrasmooth patterned metals, *i.e.* stripping with precisely patterned silicon substrates to obtain ultrasmooth pure metal films with grooves, bumps, pyramids, ridges, and holes as illustrated by Norris et al. [10] (as shown in Figs. 9.4). Those various structures are selected for possible providing the LSPs resonance modes which can be coupling with the QDs fluorescence (and the molecules SERS). The LSPs resonance modes provided by the array structures will be investigated by the reflectance spectrometer (as illustrated in chapter 2, section 2-4), how the QDs fluorescence influenced by the array structures will be investigated by fluorescence lifetime image system (as illustrated in chapter 2, section 2-2), and how the molecules SERS influenced by the array structures will be investigated by the Micro-Raman spectrometer (as illustrated in chapter 2, section 2-1).

Another potential application we are interested is the plasmonic solar cell as illustrated by Catchpole and Beck [11] (as shown in Figs. 9.5). Metal nanoparticles are strong scatterers of light when forming the LSPs resonance modes. When the LSPs resonance formed on surface of the metal nanoparticles, the scattering cross-sections are found to be larger, therefore the amount of light scattered into the cell is increased. Significant enhancements in photocurrent measurements have been found by using silver or gold nanoparticles. Further, ultrasmooth patterned metals and array structures illustrated previously are promising candidates for the plasmonic solar cell applications.



Figs. 9.5 *Left: Light excites a surface plasmon resonance on a metal nanoparticle and is coupled into silicon. Middle: Simulation of increased light intensity beneath a metal nanoparticle on a silicon cell. Right: A SEM image of silver nanoparticles on a solar cell, each averaging only 100 nm in diameter. [11].*

References

- [1] Tsang J. C., Kirtley J. R. and Bradley J. A. *Phys. Rev. Lett.* **43**, 772 (1979)
- [2] Wang Y., Becker M., Wang L., Liu J., Scholz R., Peng J., Gösele U., Christiansen S., Kim D. H., Steinhart M. *Nano Lett.* **9**, 6, 2384 (2009)
- [3] Percec J. Le, Quémerais P., Barbara A., and López-Ríos T. *Phys. Rev. Lett.* **100**, 066408 (2008)
- [4] Becker M., Sivakov V., Gösele U., Stelzner T., Andra G., Reich H. J., Hoffmann S., Michler J., and Christiansen S. H. *Small* **4**, 398 (2008)
- [5] Nie Shuming and Emory Steven R. *Science* **275**, 1102 (1997)
- [6] http://en.wikipedia.org/wiki/Malachite_green
- [7] Jin Rongchao, Cao Y. Charles, Thaxton C. Shad, and Mirkin Chad A. *Small* **2**, 3, 375 (2006)
- [8] Hoffmann S., Utke I., Moser B., Michler J., Christiansen S., Schmidt V., Senz S., Werner P., Gösele U., Ballif C. *Nano Lett.* **6**, 622 (2006)
- [9] Becker, M. , Sivakov V., Andrä G., Geiger R., Schreiber J., Hoffmann S., Michler J., Milenin A. P., Werner P., and Christiansen S. H. *Nano Letters* **7**, 75 (2007)
- [10] Nagpal Prashant, Lindquist Nathan C., Oh Snag-Hyun, Norris David J. *Science* **325**, 594 (2009)
- [11] <http://nanotechweb.org/cws/article/indepth/38421>

Publication lists

1. Yuan Chi-Tsu, Chou Wu-Ching, Chen Yueh-Nan, **Chou Jui Wen**, Chuu Der San, Lin Cheng-An J., Li Jimmy K., Chang Walter H., Shen Ji-Lin *J. Phys. Chem. C* **111**, 15166 (2007)
2. Christiansen S H, **Chou J W**, Becker M, Sivakov V, Ehrhold K, Berger A, Chou W C, Chuu D S, Gösele U *Nanotechnology* **20**, 165301 (2009)
3. **Chou J W**, Lin Kao-Chin, Lee Yao-Jen, Yuan Chi-Tsu, Hsueh Fu-Kuo, Shih Hsun-Chuan, Fan Wen-Chung, Luo Chih-Wei , Lin Ming-Chieh , Chou Wu-Ching, Chuu Der-San *Nanotechnology* **20**, 305202 (2009)
4. **Chou J W**, Tang Ying-Tsan, Lin Kao-Chin, Lee Yao-Jen, Chen Lung-I, Luo Chih-Wei , Ho Fu-Han, Yuan Chi-Tsu, Chou Wu-Ching, Chuu Der-San, “Localized Surface Plasmons on the Au coated array nanorods”, *Nanophotonics Meta-Materials conference* (April 28-May 2, 2009).
5. **Chou J W**, Lin K C, Tang Y T, Hsueh F K, Lee Yao-Jen, Luo C W, Chen Y N, Yuan C T, Shih Hsun-Chuan, Fan W C, Lin M C , Chou W C, Chuu D S *Nanotechnology* **20**, 415201 (2009)
6. **Chou J W**, Tang Y T, Fan F C, Lee Yao-Jen, Luo C W, Lin M C , Höflich Katja, Becker M, Christiansen S H, Gösele U, Chou W C, Chuu D S, “Surface Enhanced Raman Scattering Observed on Spatially Controlled Array Structures”, to be published.